DTU Nanotech
Department of Micro- and Nanotechnology

Master Thesis, s031734 and s032056

Flow in Microporous Silicon Carbide: an Experimental and Numerical Study

Kristoffer Gjendal and Henrik Bank Madsen

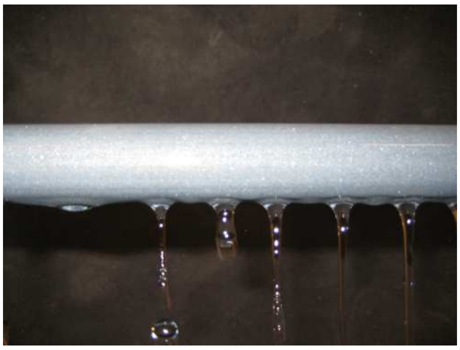

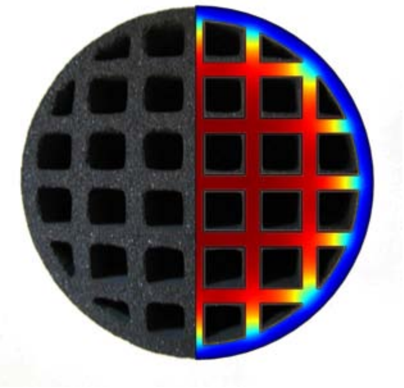

Main supervisor: Henrik Bruus
Department of Micro- and Nanotechnology
Technical University of Denmark

Co-supervisor: Thomas Eilkær Hansen
CoMeTas A/S

1 December 2008

Abstract

Flow through porous silicon carbide (SiC) is studied in order to get an understanding of the parameters influencing the flow. As porous SiC is used to fabricate membranes, a deeper understanding of the flow through porous SiC would assist in the design process of more efficient membranes as well as with improving existing membranes.

The flow in porous SiC is described by Darcy's law which is demonstrated both analytically and by means of thorough experiments on different SiC-samples, such as simple plugs, monotubes and so-called 24-channel tubes with a complex geometry. Experiments are conducted both with pure SiC-substrates and with substrates coated with different thin membrane layers.

From experiments with monotubes a permeability of the SiC-substrate is found and used in two numerical models developed to describe the flow in porous SiC. Results from the numerical models are compared to experimental results, and good correlation is achieved between simulations and experiments. The numerical models are used to develop optimized geometries with focus on increasing the permeate flow rate delivered from the tubes. These new design proposals are compared to existing membrane geometries used by CoMeTas, the membrane company we cooperate with during the work for this thesis, and the results show that significant increases in the permeate flow rate are obtained by making relatively small and simple geometrical changes.

Resume

Flow gennem porøs siliciumkarbid (SiC) bliver i denne afhandling undersøgt for at opnå en større forståelse af de influerende parametre. Da porøs SiC anvendes til fremstillingen af membraner, vil en større forståelse af strømningerne gennem materialet være nyttig når nye membraner skal fremstilles eller eksisterende skal forbedres.

Flowet gennem porøs SiC er beskrevet ved Darcy's lov, hvilket eftervises både analytisk og ved gennemgribende eksperimenter med forskellige SiC-emner, såsom simple skiver, enkeltkanalsrør og 24-kanalsrør med en kompleks geometri. Eksperimenter udføres både med rene SiC-substrater og med substrater, der er coatet med forskellige tynde membranlag.

Permeabiliteten i SiC-substratet findes ud fra eksperimenter med enkeltkanalsrør, og den bliver anvendt i to udviklede numeriske modeller, som beskriver strømningerne i porøs SiC. Resultaterne fra de to numeriske modeller bliver sammenlignet med resultaterne fra eksperimenterne og god overensstemmelse findes mellem simuleringer og eksperimenter. De numeriske modeller bliver anvendt til at udvikle optimerede geometrier med fokus på at øge permeat flowet gennem rørene. Permeat flowet fra optimerede rør bliver sammenlignet med permeat flowet fra standard membraner fra CoMeTas, som er det firma vi har samarbejdet med i vores afgangsprojekt. Denne sammenligning viser at det er muligt at opnå store forøgelser af permeat flowet ved relativt små og simple indgreb.

Preface

This thesis, titled ”Flow in Microporous Silicon Carbide: an Experimental and Numerical Study”, has been submitted in order to obtain the Master of Science degree at the Technical University of Denmark (DTU). The project work was carried out within the Theoretical Microfluidics (TMF) group at the Department of Micro- and Nanotechnology (DTU Nanotech) and in cooperation with the membrane company CoMeTas during the period from February 2008 to December 2008, corresponding to a credit of 45 ECTS points.

First of all we want to thank our supervisor Henrik Bruus for invaluable guidance and inspiration throughout the thesis work and for always having extra time to spare to discuss different issues. Further we are thankful to our co-supervisor Thomas Eilkær Hansen and the rest of the staff at CoMeTas for their help and encouragement especially during the experimental part of the project. We also acknowledge CoMeTas for putting the experimental setup at our disposal and for giving us free hands during the entire project. We have also appreciated the ideas and comments offered by the rest of the TMF group, especially at the weekly group meetings.

We are grateful to Johnny Marcher (technical director at LiqTech) for lending us equipment and for his good advise during the fabrication and geometrical optimization process. Furthermore we want to express our gratitude to Alexander Shapiro (associate professor, Department of Chemical and Biochemical Engineering, DTU) and Duc Thuong Vu (technician, Department of Chemical and Biochemical Engineering, DTU) for introducing us to the CT-scanner and its possibilities. Also we thank Jesper Lybæk from the company Jaka Metal for water-jet cutting our plugs.

Finally, we want to thank all those not mentioned above, but who have offered their assistance or helped us in one way or another during our project.

Kristoffer Gjendal and Henrik Bank Madsen
Department of Micro- and Nanotechnology
Technical University of Denmark
1 December 2008

Contents

List of Figures

List of Tables

List of symbols

Symbol	Description	Unit
$\mathcal{A}$	Area	m^2
a	Radius of a cylinder	m, mm
c_0	Dimensionless shape factor	
D, d	Diameter	m, mm, μm
e	Pipe roughness	m, mm
f	Friction factor	
g	Gravitational acceleration	$\mathrm{m\ s}^{-2}$
$\mathbf{g}$	Gravitational acceleration vector	$\mathrm{m\ s}^{-2}$
H, h	Height	m, mm
h_l	Major head loss	$\mathrm{m}^2\ \mathrm{s}^{-2}$
$h_{\mathrm{l}_\mathrm{m}}$	Minor head loss	$\mathrm{m}^2\ \mathrm{s}^{-2}$
$h_{\mathrm{l}_\mathrm{T}}$	Total head loss	$\mathrm{m}^2\ \mathrm{s}^{-2}$
I	Electric current	A
K_l	Loss coefficient	
k	Permeability	m^2
L, ℓ	Length	m, mm
L_0	Characteristic length	m, mm
m	Mass	kg
$\mathbf{n}$	Normal vector	
p	Pressure	Pa, bar
p_0	Atmospheric gauge pressure	Pa, bar
$\bar{p}$	Time averaged mean gauge pressure	Pa, bar
p^*	Reference pressure	Pa, bar
Δp_surf	Young-Laplace pressure drop	Pa, bar
Q	Volume flow rate	$\mathrm{m}^3\ \mathrm{s}^{-1}$, $\mathrm{m}^3\ \mathrm{h}^{-1}$
R	Electric resistance	Ω
R_hyd	Hydraulic resistance	$\mathrm{Pa\ s\ m}^{-3}$
R_c	Channel resistance	$\mathrm{Pa\ s}^2\ \mathrm{m}^{-6}$
Re	Reynolds number	
r	Radius	m, mm
S	Surface area pr. volume of particles	m^{-1}
T	Time scale	s
t	Time	s
$\tilde{t}$	Normalized time	

Symbol	Description	Unit
ΔU	Electric potential difference	V
$\mathcal{V}$	Volume	m^3
$\bar{V}$	Time averaged mean velocity	$\mathrm{m\ s^{-1}}$
V_0	Characteristic velocity	$\mathrm{m\ s^{-1}}$
$\mathbf{v}$	Velocity vector	$\mathrm{m\ s^{-1}}$
v	Velocity	$\mathrm{m\ s^{-1}}$
w	Wall thickness	m, mm
w_e	Actual flow distance	m, mm
z	Vertical position	m
α	Kinetic energy coefficient	
β	Dissipative force	$\mathrm{Pa\ s\ m^{-2}}$
γ	Surface tension	$\mathrm{J\ m^{-2}}$, $\mathrm{mJ\ m^{-2}}$
ε	Error	
ζ	Correlation coefficient	
η	Dynamic viscosity	Pa s
θ	Polar angle	
κ	Kozeny-Carman constant	
λ	Constant	m
ρ	Mass density	$\mathrm{kg\ m^{-3}}$
τ	Tortuosity	
ϕ	Porosity (volume fraction)	

Subscript	Description
b	Bubble point
c	Channel
d	Dry
f	Feed
m	Mean
n	Normal
o	Outer
p	Permeate
r	Retentate
s	Substrate
tm	Transmembrane
w	Water

Chapter 1

Introduction

1.1 Membrane filtration

Flow through porous media is encountered in many different types of engineering, one of the most important being membrane filtration. Filtration is traditionally defined as the separation of particulate material from a fluid by the passage of the fluid through a porous material (the filter) that retains the particles on or within itself. The driving force in this process is the pressure difference applied across the filter. Membrane filtration, on the other hand, has a broader definition. It includes not only the separation of particulate matter, but also the separation of soluble components. Furthermore, membrane filtration differs from conventional filtration because material, which is unable to permeate through the membrane, may remain in suspension upstream of the membrane instead of being retained on or within the filter. For further information about filtration see [5, 6].

Generally, two methods are used in membrane filtration. In the most simple and conventional method the fluid permeates through the membrane while the particulate material is rejected at the surface of the membrane, thus the filtered solids are allowed to

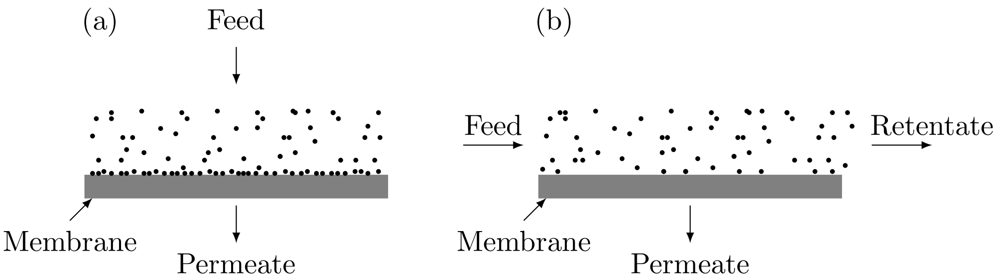

Figure 1.1: (a) Principle of dead-end filtration. The fluid permeates through the porous membrane, while particles larger than the pore size in the membrane are rejected at the surface of the membrane and build up as a filter cake. (b) Principle of cross-flow filtration. The direction of the feed stream is tangentially over the surface of the membrane in order to sweep the rejected particles away from the membrane. The fluid is separated into two product streams, the permeate, which is depleted of the rejected particles, and the retentate (or concentrate), which is enriched in those particles. This figure is made with inspiration from [6].

build up as a so-called filter cake on the surface of the membrane, see Fig. 1.1(a). This method is referred to as dead-end filtration. It is a very energy efficient method, but it is rarely used because the permeation rate through the combined membrane and surface cake layer would, in most applications, fall to very low levels. Therefore another method, the so-called cross-flow method, is widely used in membrane filtration, see Fig. 1.1(b). In this method the feed flow is tangential to the surface of the membrane in order to sweep rejected particles and solutes away. The feed fluid is separated into two product streams, the permeate, which is depleted of the rejected particles, and the retentate (or concentrate), which is enriched in those particles. The feed fluid is defined as the initial fluid mixture before the membrane. The permeate fluid is defined as the stream that emerges from the membrane and is depleted of the rejected particulate material. The retentate (or concentrate) is defined as the stream on the upstream side of the membrane, which is enriched in the same components [5, 6].

This thesis deals only with the pure water flow through a porous membrane, not with a fluid mixture containing particulate material. Therefore the filtration process itself will not be investigated.

1.2 Membranes and silicon carbide

Copenhagen Membrane Technology A/S (CoMeTas) was founded in 2006 at Scion, DTU, and is today situated in Bagsværd. The company develops and manufactures ceramic membranes of porous silicon carbide (SiC) for both dead-end and cross-flow applications. CoMeTas' membranes are so-called asymmetric membranes, meaning that they consist of two different layers. The main structure, called the substrate or carrier, is made of large SiC-particles sintered together, and this substrate supports one or more thin top layers consisting of smaller SiC-particles, called the membrane layers. The membrane layers have a thickness of approximately 50 µm to 200 µm and a mean pore size of around 0.01 µm to 0.5 µm, while the substrate thickness is minimum 0.8 mm and has a mean pore size of 10 µm to 20 µm, [19, 20]. This design increases the flow rate through the filter, as the resistance in the substrate is significantly lower than the resistance in the membrane layer due to the larger particles. The pore size in the membrane layer determines the size of the particulate material that is rejected, and it can be changed by varying the SiC-particle composition in the membrane layer.

Silicon carbide membranes have many advantages. They are very wear resistant, as SiC is one of the hardest materials known, they have a relatively high flow rate compared to other porous ceramic membranes, and they have high chemical and physical stability and thus a long service life-time. All these properties make porous SiC a very promising material with respect to membrane applications.

1.3 Objective and motivation

As CoMeTas is a newly started company, the knowledge concerning the flow in their membranes is still limited. Theoretical and experimental investigations of the flow in SiC-membranes have previously been studied by M.Sc. Thomas Eilkær Hansen (TEH) in his M.Sc. project [10].

The scope of the present project has been to continue and extend the work of TEH, in order to get a better understanding of the phenomena of liquid flow in SiC. This investigation includes both experimental and numerical computational work. Extensive experiments are conducted with different types of SiC-samples, going from simple plugs, through monotubes to the so-called 24-channel tubes having a complex geometry. In the experiments both pure SiC-substrates and tubes coated with different membrane layers will be used, and the experiments will be used to verify Darcy's law in a porous media and to determine the permeability, which is an expression for the hydraulic conductivity, of the SiC. The numerical work will contain simulations using the software Comsol Multiphysics™ and a so-called equivalent circuit model developed in Matlab. These models will be validated by means of the experimental results and will be used to optimize the liquid flow through the SiC.

Since the focus will be on the liquid flow phenomena in the porous SiC, and not the filtration process, the SiC-samples will not be referred to as SiC-membranes, but merely as SiC-plugs and SiC-tubes.

1.4 Outline

The work presented in this thesis is a selection of the work carried out during our master project, and some aspects like basic considerations and investigations regarding the fabrication of the SiC-samples and the experimental setup and some experimental and numerical results have been omitted for clarity.

We used the first three months on initial work such as literature study, fabrication of the SiC-samples and development of simple methods that could be used to characterize the SiC. The setup used for the experimental part was a new setup provided by CoMeTas. This setup caused unforseen problems, and it ended up lasting more than two months to modify and improve it to obtain satisfactory results. The remaining project time was equally divided between experimental and numerical work. The experimental work was conducted at the premises of CoMeTas, while the numerical work was conducted at the Department of Micro- and Nanotechnology at DTU.

The chapters contain following:

- Chapter 2: We begin by introducing the fundamental governing equations and some theoretical considerations concerning the flow in a porous media and flow in channels with porous walls. The content of Chapter 2 can be found in several textbooks and papers and will be well known to readers familiar with porous media.

- Chapter 3: The fabrication process is described as well as the improvements we made to obtain the best possible SiC-samples. Further we present some simple characterization methods used to check the quality, porosity and pore size of the SiC-samples.

- Chapter 4: The experimental setup is shortly described along with the improvements we made to obtain satisfactory results.

- Chapter 5: The experiments conducted with the substrate SiC-samples are presented here together with the obtained results. These experiments include plugs with four different thicknesses, monotubes with two different wall thicknesses and 24-channel tubes.

- Chapter 6: This chapter describes the experiments carried out on monotubes and 24-channel tubes coated with membrane layers in the same manner as CoMeTas' membranes. The obtained results are presented together with a short investigation of the quality and thickness of the membrane layers.

- Chapter 7: Two numerical models are developed, a simple 2D model made in COMSOL on the basis of potential flow and the Laplace equation, and a 3D equivalent circuit model made in MATLAB. Results obtained with the two models are presented and compared with experimental results.

- Chapter 8: Using the developed numerical models, new membrane designs are presented with the focus on increasing the permeating water flow. The performance of the proposed designs are compared with existing membranes from CoMeTas.

- Chapter 9: The thesis is rounded off with a conclusion and an outlook.

Chapter 2

Basic theory and considerations

In the following the general theoretical basis of this thesis will be given. Two major flow situations are considered, the flow through a porous medium and the channel flow in a porous tube. For this purpose two simple flow problems are investigated. A 1D problem of flow through a porous plug is used to check if Darcy's linear law is valid in porous SiC and a 2D problem of the flow through a pipe with porous walls is used to investigate how the pressure develops down the length of a porous SiC-tube.

Furthermore the governing equations used in the two numerical models are given, namely the Laplace equation used in the COMSOL simulations and the equivalent circuit theory used in the equivalent circuit model.

Section 2.2 is written with inspiration from DTU Nanotech master thesis by Thomas Eilkær Hansen [10].

2.1 Fundamental equations

The Navier–Stokes equation is the fundamental, partial differential equation describing the motion of fluids by conservation of momentum. For an incompressible, Newtonian fluid it can be expressed as

$$\rho[\partial_t \mathbf{v} + (\mathbf{v}\cdot\boldsymbol{\nabla})\mathbf{v}] = -\boldsymbol{\nabla} p + \eta\nabla^2\mathbf{v} + \rho\mathbf{g}, \tag{2.1}$$

where ρ and η are the fluid mass density and dynamic viscosity, respectively, $\mathbf{v}$ is the velocity vector, p is the pressure and $\mathbf{g}$ is the gravitational vector. The left-hand side of Eq. (2.1) can be interpreted as inertia force densities while the right-hand side is the applied force densities. The gravitational term $\rho\mathbf{g}$ is neglected throughout this thesis.

The primary controlling parameter in viscous fluid flows is the dimensionless Reynolds number Re describing the relative importance between inertia and viscous forces in the fluid,

$$\mathrm{Re} = \frac{\text{Inertia}}{\text{Viscosity}} = \frac{\rho V_0 L_0}{\eta}, \tag{2.2}$$

where V_0 is a characteristic velocity and L_0 is a characteristic length. If the Reynolds number is low the viscous forces are dominating in the flow and the left-hand side of the

Navier–Stokes equation can therefore be neglected. In this case the flow is laminar and Eq. (2.1) reduces to

$$0 = -\boldsymbol{\nabla} p + \eta \nabla^2 \mathbf{v}, \tag{2.3}$$

which is the linear Stokes equation. If the Reynolds number is high inertia is dominating the flow and the laminar flow will break down. Instead the flow evolves into a new regime called turbulence which is a fluctuating, disorderly motion that cannot be predicted by stability theory. Turbulent flow can generally be described as a spatially varying mean flow with superimposed three-dimensional random fluctuations that are self-sustaining and enhance mixing, diffusion, entrainment and dissipation, [4]. We will not describe turbulent flow in detail here, as it is not the scope of this thesis.

2.2 Flow in porous media

A porous medium is defined as a volume consisting of a solid, the solid matrix, which is permeated by pores, the void space, filled with a fluid being liquid or gas. At least some of the pores should be interconnected to make the volume permeable, [2].

2.2.1 Permeability

Most porous media, like porous SiC, consist of a very complex solid matrix making it almost impossible to describe the geometry in an exact manner. However, it is often possible to describe the porous medium as a continuum, where the hydraulic resistance in each pore is averaged to a mean hydraulic resistance of the entire medium. This resistance is described by the properties of the fluid and the properties of the solid matrix. In an analogy to Ohm's law from electrical circuits the hydraulic conductivity is the inverse of the hydraulic resistance and is denoted the permeability k. The permeability of a porous medium indicates how well a fluid permeates, i.e. a high permeability induce a high permeating flow rate.

The permeability is typically said to be dependent on three properties of a porous medium. The porosity ϕ is defined as the volume $\mathcal{V}_{\text{void}}$ of the void space in the medium divided by the total volume $\mathcal{V}_{\text{total}}$ of the medium,

$$\phi = \frac{\mathcal{V}_{\text{void}}}{\mathcal{V}_{\text{total}}}. \tag{2.4}$$

Another property used to define the permeability is the total surface area $\mathcal{A}$ of the particles divided by the total volume. Assuming spherical particles it is found as

$$S = \frac{\mathcal{A}}{\mathcal{V}_{\text{total}}} = \frac{6}{d_{\text{m}}}, \tag{2.5}$$

where d_{m} is the mean particle diameter of the medium. The last property is the so-called tortuosity τ, which is used to indicate how complicated the flow path through a porous medium is,

$$\tau = \left(\frac{w}{w_{\text{e}}}\right)^2, \tag{2.6}$$

where w is the direct distance between inlet and outlet and w_e is the actual flow distance. The permeability can then be estimated from the Kozeny–Carman equation, [2],

$$k = \frac{\phi^3}{S^2 \kappa (1-\phi)^2}, \tag{2.7}$$

where $\kappa = c_0/\tau$ is an experimentally determined constant known as the Kozeny–Carman constant and c_0 is a dimensionless shape factor used to compensate for the non-circular shape of the pores. Assuming spherical particles and using the recommended value of $\kappa = 5$ from [13] we obtain

$$k = \frac{d_\mathrm{m}^2 \phi^3}{180(1-\phi)^2}. \tag{2.8}$$

This equation is based on empirical data and can only be used to find an approximate value of the permeability in a porous medium. To get an exact value of the permeability flow experiments will have to be conducted.

2.2.2 Flow regions and Darcy's law

The flow in a porous material can be divided into four regions, pre-Darcy flow, Darcy flow, Forchheimer flow and turbulent flow, as shown in Fig. 2.1. The transition between the regions is smooth meaning that it is difficult to determine the flow pattern in the transitions. The defining parameter for the four regions is the Reynolds number, Eq. (2.2), based on the mean particle diameter. Darcy flow occurs at $10^{-5} < \mathrm{Re} < 2.3$, Forchheimer flow at $5 < \mathrm{Re} < 80$ and turbulent flow at $\mathrm{Re} > 120$, as stated in [12]. These values are the results of the work from only one reference and they are subject to some disagreement, e.g. [13, 16].

Pre-Darcy flow is only present in extremely slow flows and no generally accepted theory describing this region exists. Darcy flow is described by Darcy's law, which expresses

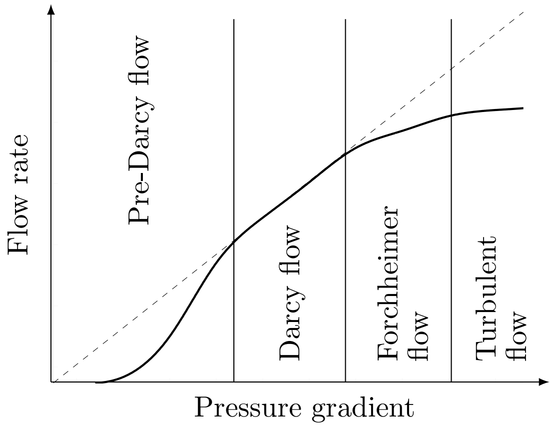

Figure 2.1: The relation between the pressure gradient and the flow rate in the different flow regimes in a porous material. The flow is laminar in the pre-Darcy and Darcy zones. In the Forchheimer zone the flow is in a transition zone between laminar and turbulent flow and in the turbulent zone the flow is fully turbulent. This figure is made with inspiration from [8, 21].

a linearity between the permeating flow rate and the applied pressure difference, [2, 7, 9]. Henry Darcy derived this law in 1856 from experiments with water through a pipe containing sand, and it is given as

$$\mathbf{v} = -\frac{k}{\eta}\boldsymbol{\nabla} p, \tag{2.9}$$

where $\mathbf{v}$ is the macroscopic velocity through the porous medium defined as $\mathbf{v} = \mathbf{Q}/\mathcal{A}$ with $\mathbf{Q}$ being the volume flow rate and $\mathcal{A}$ being the active surface area of the porous medium. The flow in the pre-Darcy and Darcy regions is laminar. When the inertial forces become significant, the flow enters a transition zone between laminar and turbulent flow and Darcy's law is no longer valid. The flow in the transition zone is denoted Forchheimer flow. When the flow enters the turbulent zone the flow is recognized as fully turbulent and it is then unstable and unsteady.

In membrane technology it is generally assumed that Darcy's law is valid in the porous medium. The following assumptions has to be valid in order to apply Darcy's law, [2, 7, 9]:

- Inertial forces are negligible in the fluid flow.
- Isotropic porous medium. If it is anisotropic the permeability may vary in the medium.
- The pressure gradient is constant through the porous medium.
- The fluid is heterogeneous, i.e. the fluid has constant density.
- Completely saturated medium, i.e. there is a single fluid flow.

An estimate of a typical Reynolds number is made to determine whether or not it is reasonable to assume that the flow in SiC can be described by Darcy's law. An estimate of the permeability of SiC is found to be $k = 1 \times 10^{-13}\,\mathrm{m}^2$ calculated from Eq. (2.8) with a porosity of $\phi = 0.4$ and assuming that the mean grain diameter d_m is approximately the same size as the mean pores, $d_\mathrm{m} = 10\,\mu\mathrm{m}$, see [20]. The dynamic viscosity of water at 20°C is $\eta = 10^{-3}\,\mathrm{Pa\ s}$, a typical pressure difference is $\Delta p = 1\,\mathrm{bar}$ and a typical thickness of SiC is $w = 2\,\mathrm{mm}$. The velocity in the porous SiC is found from Eq. (2.9) assuming that the pressure gradient is constant, $\boldsymbol{\nabla} p = -\Delta p/w$, giving a velocity of $v = 5 \times 10^{-3}\,\mathrm{m/s}$. The Reynolds number is then found from Eq. (2.2) using this velocity and $\rho = 1000\,\mathrm{kg/m}^3$ for water, to be

$$\mathrm{Re} \approx 0.05. \tag{2.10}$$

From this simple estimate the flow in the porous SiC can then be described by Darcy's law under typical conditions.

2.2.3 1D flow through porous plug in a pipe

A simple flow problem is used to find an analytical solution to the flow in a porous medium. The flow problem consists of an infinitely long, translation-invariant pipe with a plug of porous material, see Fig. 2.2. The width of the plug is w while the radius of the pipe is

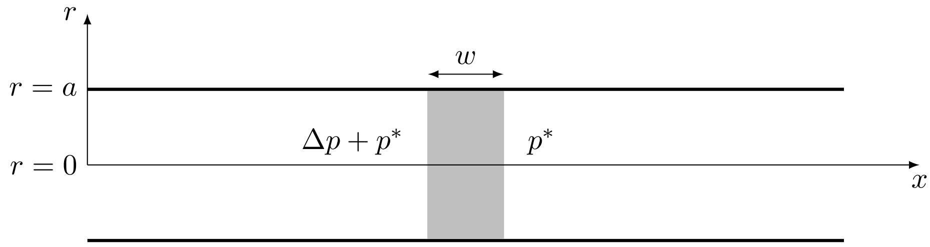

Figure 2.2: Infinitely long, translation-invariant pipe containing a plug of porous medium. The width of the plug is w and the radius of the pipe is a. An external pressure difference is put on the pipe.

a. An external pressure difference is put on the pipe. The flow in the pipe is assumed to be laminar and can thus be described as a Poiseuille flow, while the flow in the porous medium is described by Darcy's law. The entire flow can then be described by Brinkman's equation, which is Stokes's equation, see Eq. (2.3), extended with a dissipative force $\beta\mathbf{v}$ acting against the flow,

$$0 = -\boldsymbol{\nabla} p + \eta\nabla^2\mathbf{v} - \beta\mathbf{v}. \tag{2.11}$$

The dissipative force originates in the porous material with $\beta = \eta/k$. Outside the porous material $\beta = 0$. The pressure gradient is assumed to be constant in the porous material, thus $\boldsymbol{\nabla} p = -\Delta p/w$. This assumption is applied to Eq. (2.11) together with cylindrical coordinates. The equation is non-dimensionalized with the following parameters, $\ell = \sqrt{k}$, $v_0 = (k\Delta p)/(\eta w)$, $s = r/\ell$, $\tilde{s} = a/\ell$ and $u(s) = v_x/v_0$ to

$$0 = u''(s) + \frac{1}{s}u'(s) - u(s) + 1, \tag{2.12}$$

which is a second order inhomogeneous differential equation. A particular solution is easily seen to be $u(s) = 1$. The solution to the homogeneous part is found as the solution to the modified Bessel function of zeroth order. The boundary conditions are no-slip on the walls $u(\tilde{s}) = 0$ and a symmetry condition $\partial_r u(r) = 0|_{r=0}$. The solution to Eq. (2.12) then appears as

$$u(s) = 1 - \frac{I_0(s)}{I_0(\tilde{s})}. \tag{2.13}$$

This solution is investigated in its two limits, $\tilde{s} \ll 1$ and $\tilde{s} \gg 1$. In the first case of $\tilde{s} \ll 1$, i.e. $a \ll \sqrt{k}$, the solution is found using a Taylor expansion of $I_0(s)$ to be,

$$v_x(r) = \frac{\Delta p}{4\eta w}(a^2 - r^2), \qquad \text{for } a \ll \sqrt{k}. \tag{2.14}$$

This is recognized as the Poiseuille flow solution for laminar flow in a straight pipe. The flow in the plug can then be described as a normal pipe flow if the permeability k is large compared to the radius a. This result is expected because if k is large the plug will not imply any significant resistance to the flow.

In the second case of $\tilde{s} \gg 1$, i.e. $a \gg \sqrt{k}$, the solution becomes

$$u(s) = 1 - \sqrt{\frac{\tilde{s}}{s}}e^{-(\tilde{s}-s)}. \tag{2.15}$$

The permeability of SiC is around $k = 1 \times 10^{-13}\,\mathrm{m}^2$, and it is therefore a good approximation to use $u(s) \equiv 1$. The velocity then becomes,

$$v_x(r) = v_0 = \frac{k}{\eta}\frac{\Delta p}{w}, \qquad a \gg \sqrt{k}, \tag{2.16}$$

which is recognized as Darcy's law in a 1D flow. From this it can be concluded that the velocity in porous SiC can be described by Darcy's law.

2.2.4 2D flow in pipe with porous walls

The pressure drop in a pipe with porous walls will be investigated in this section. The flow problem containing a channel with porous walls is seen in Fig. 2.3. The wall thickness is w and the length and the inner radius of the pipe is L and a, respectively. The flow in the pipe is assumed to be a Poiseuille flow and it can then be described by the Hagen-Poiseuille law,

$$Q_{\mathrm{pipe}}(x) = -\frac{\pi a^4}{8\eta} p'(x) = \frac{\pi a^4}{8\eta}\frac{\Delta p(x)}{w}, \tag{2.17}$$

assuming that the pressure gradient across the wall is constant, $p'(x) = -\Delta p(x)/w$. Darcy's law, Eq. (2.9), is assumed to describe the flow in the porous walls. The flow through the porous material is then found as

$$Q_{\mathrm{p}}(x) = \frac{2\pi a k}{\eta}\frac{\Delta p(x)}{w} dx. \tag{2.18}$$

In a section of the domain with the length dx, the conservation of mass is used to find the relation between the incoming flow rate $Q_{\mathrm{pipe}}(x)$, the permeating flow rate $Q_{\mathrm{p}}(x)$ and the outgoing flow rate $Q_{\mathrm{pipe}}(x + dx)$. Assuming that $(p'(x + dx) - p'(x))/dx = p''(x)$, we then have

$$p''(x) = \frac{1}{\lambda^2}\Delta p(x), \quad \lambda = \sqrt{\frac{a^3 w}{16k}}. \tag{2.19}$$

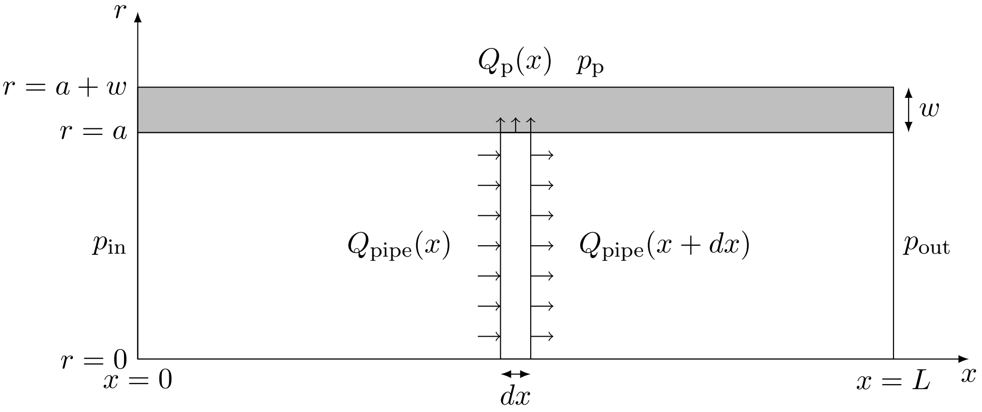

Figure 2.3: Straight pipe with porous walls. The wall thickness is w, the inner radius of the pipe is a, and the length is L. An external pressure difference is put on the pipe.

The solution to Eq. (2.19) must be an exponential function and since $\Delta p(x) = p(x) - p_{\mathrm{p}}$ the solution has the following form,

$$p(x) - p_{\mathrm{p}} = Ae^{x/\lambda} + Be^{-x/\lambda}. \tag{2.20}$$

The boundary conditions are $p(0) = p_{\mathrm{in}}$ and $p(L) = p_{\mathrm{out}}$ as seen in Fig. 2.3. Using these boundary conditions and $p_{\mathrm{p}} = 0$, the solution becomes

$$p(x) = p_{\mathrm{in}} + \frac{x}{L}\left[p_{\mathrm{out}} - p_{\mathrm{in}} - \left(\frac{L}{\lambda}\right)^2\left(\frac{1}{3}p_{\mathrm{in}} + \frac{1}{6}p_{\mathrm{out}}\right)\right] + \frac{1}{2}\left(\frac{x}{\lambda}\right)^2\left[p_{\mathrm{in}}\left(1 - \frac{1}{3}\frac{x}{L}\right) + \frac{1}{3}p_{\mathrm{out}}\frac{x}{L}\right]. \tag{2.21}$$

It is seen that the factor $(L/\lambda)^2$ controls the deviation from a linear pressure drop. Using $a = 6.5\,\mathrm{mm}$, $w = 3.5\,\mathrm{mm}$, $k = 1 \times 10^{-13}\,\mathrm{m}^2$ and $L = 305\,\mathrm{mm}$, we have $(L/\lambda)^2 = 2 \times 10^{-4}$. Since $(x/\lambda)^2 \leq (L/\lambda)^2 \ll 1$, we can conclude that the pressure drop can be assumed to be linear in a pipe with a laminar flow and walls of porous SiC. This means that the transmembrane pressure p_{tm}, which is the pressure difference over the porous wall of the pipe, can be estimated as

$$p_{\mathrm{tm}} = \frac{p_{\mathrm{in}} + p_{\mathrm{out}}}{2} - p_{\mathrm{p}}. \tag{2.22}$$

This approximation of the transmembrane pressure will be used throughout this thesis.

2.3 General channel flow

In the previous section we assumed that the flow was laminar in the channel, but in many cases this is not true. When the Reynolds number exceeds 2300 the laminar channel flow breaks down and when Re > 4000 the flow becomes fully turbulent, [3]. Pressure drops in a circular channel with viscous flow is described by the energy equation,

$$\left(\frac{p_1}{\rho} + \alpha_1\frac{\bar{V}_1^2}{2} + gz_1\right) - \left(\frac{p_2}{\rho} + \alpha_2\frac{\bar{V}_2^2}{2} + gz_2\right) = h_{\mathrm{l_T}} = h_{\mathrm{l}} + h_{\mathrm{l_m}}, \tag{2.23}$$

which assumes that the flow is steady and incompressible, and the internal energy and the pressure are uniformly distributed across the two cross-sections 1 and 2 in the channel. In Eq. (2.23) α is the kinetic energy coefficient, $\bar{V}$ is the average velocity in the channel, g is the gravitational constant and z is the vertical position. The subscripts 1 and 2 corresponds to the cross-sections where the energy equation is applied. $h_{\mathrm{l_T}}$ is the total head loss and h_{l} and $h_{\mathrm{l_m}}$ are the sum of the major and minor losses, respectively. The major losses are caused by the frictional effects in a straight channel with constant cross-section, while the minor losses are due to expansions, contractions, bends, inlets and outlets. For fully developed flow through a horizontal pipe with constant cross-section we have that $\alpha_1\bar{V}_1^2/2 = \alpha_2\bar{V}_2^2/2$ and $h_{\mathrm{l_m}} = 0$ and Eq. (2.23) reduces to

$$\frac{p_1 - p_2}{\rho} = \frac{\Delta p}{\rho} = h_{\mathrm{l}}. \tag{2.24}$$

The major loss is found as

$$h_{\mathrm{l}} = f\frac{L}{D}\frac{\bar{V}^2}{2}, \tag{2.25}$$

where f is the so-called friction factor, L the length between the two cross-sections and D is the diameter of the channel. By combining Eqs. (2.24) and (2.25) a correlation between the pressure difference and the flow rate appears,

$$\Delta p = R_\mathrm{c}\ f(\frac{e}{D}, Re)\ Q^2, \qquad R_\mathrm{c} = \frac{L}{D^5}\frac{8\rho}{\pi^2}, \tag{2.26}$$

where R_c is the channel resistance and e/D is the relative roughness in the pipe. For laminar flow, $\mathrm{Re} < 2300$, the friction factor is defined as

$$f = \frac{64}{\mathrm{Re}}. \tag{2.27}$$

When inserting the laminar friction factor in Eq. (2.26), the Hagen-Poiseuille law for a circular straight channel appears,

$$\Delta p = \frac{128\eta L}{D^4\pi}Q. \tag{2.28}$$

No analytical expression for the friction factor is known for turbulent flow, but it can be read from the experimentally based Moody diagram, e.g. [3], with known values of the relative roughness and the Reynolds number. Several mathematical expressions have been fitted to the Moody diagram, the most widely used being the implicit expression from Colebrook,

$$\frac{1}{f^{0.5}} = -2.0\log\left(\frac{e/D}{3.7} + \frac{2.51}{\mathrm{Re}\ f^{0.5}}\right). \tag{2.29}$$

When assuming smooth channels, another fitted expression can be used in a turbulent flow at $\mathrm{Re} \leq 10^5$ called the Blasius correlation,

$$f = \frac{0.316}{\mathrm{Re}^{0.25}} \tag{2.30}$$

Inserting the Blasius expression into Eq. (2.26) gives the turbulent relation between pressure drop and flow rate,

$$\Delta p = \frac{1.788L\eta^{\frac{1}{4}}\rho^{\frac{3}{4}}}{D^{\frac{19}{4}}\pi^{\frac{7}{4}}}Q^{\frac{7}{4}}, \tag{2.31}$$

and it is seen that the relation is nonlinear. Throughout this thesis we will use the Colebrook expression, Eq. (2.29) in a turbulent flow as it is the more general of the two presented here. Furthermore the SiC-tubes will be assumed to be smooth ($e/D = 0$), since the relative roughness is unknown.

We will thus use $f = 64/\mathrm{Re}$ in laminar flow at $\mathrm{Re} < 2300$ and Colebrook with the assumption of smooth pipes is used at $\mathrm{Re} > 4000$. In the transition zone between laminar and turbulent flow the friction factor is unknown and therefore a smooth transition is made at $2300 \leq \mathrm{Re} \leq 4000$ between the laminar and the turbulent friction factor.

2.4 Equivalent circuit model

An analog between the Hagen-Poiseuille law, Eq. (2.28), and Ohm's law in electricity is studied. The Hagen-Poiseuille law is written more generally as

$$\Delta p = R_{\text{hyd}} Q, \tag{2.32}$$

where R_{hyd} is the hydraulic resistance. This linear relation is compared to Ohm's law, which states that

$$\Delta U = RI, \tag{2.33}$$

where ΔU is the difference in electric potential difference, R is the electric resistance and I is the electric current. The analog between Eq. (2.32) and Eq. (2.33) is obvious and even the rules of series/parallel coupling of resistors and capacitors can be used in the Hagen-Poiseuille law. This means that for two channels in series coupling we can use the simple additive law,

$$R = R_1 + R_2, \tag{2.34}$$

and for two channels in parallel coupling we can use the additive law of inverse resistances,

$$R = \left(\frac{1}{R_1} + \frac{1}{R_2}\right)^{-1} = \frac{R_1 R_2}{R_1 + R_2}. \tag{2.35}$$

The analog can be used when building a numerical model of a fluidic network in which the pressure differences become electrical potential differences, the hydraulic channel resistances become resistors and flow rates become currents. For a given fluidic circuit or network we can then apply Kirchhoff's laws:

1. The sum of flow rates entering/leaving any node in the circuit is zero.
2. The sum of all pressure differences in any closed loop of the circuit is zero.

The analog between electrical and fluidic circuits is described in detail in [1].

2.5 The Laplace equation in 1D and 2D Darcy flow

The continuity equation for an incompressible fluid is given as

$$\boldsymbol{\nabla} \cdot \mathbf{v} = 0, \tag{2.36}$$

and combining it with Darcy's law from Eq. (2.9) the governing equation for the pressure distribution in a porous medium appears,

$$\nabla^2 p = 0 \tag{2.37}$$

which is the Laplace equation for the pressure. In a 1D flow problem through a porous plug with thickness w and radius a, see Fig. 2.4(a), the solution to the pressure distribution is very simple and found as

$$p(x) = \frac{p_2 - p_1}{w} x + p_1, \quad 0 \le x \le w. \tag{2.38}$$

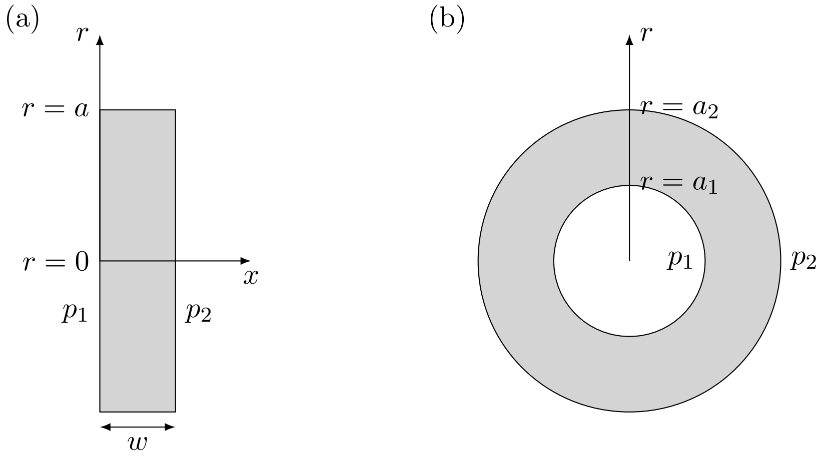

Figure 2.4: (a) Side-view of circular plug with a 1D flow problem. (b) Cross-section of a tube with porous walls with a 2D flow problem. In both figures $p_1 > p_2$.

Combining this equation with Darcy's law and integrating the velocity with respect to the active surface area, which in this case is equal to the cross-sectional area of the plug, gives the permeating flow rate Q_p,

$$Q_\mathrm{p} = \frac{\pi a^2 k}{\eta} \frac{\Delta p}{w}, \tag{2.39}$$

where $\Delta p = p_1 - p_2$.

In a 2D flow problem through the porous walls of a tube, see Fig. 2.4(b), the pressure distribution is no longer linear. The inner and outer radius of the tube is a_1 and a_2, respectively. The pressure inside the tube is p_1 and outside the tube it is p_2. The solution to Eq. (2.37) is then

$$p(r) = \frac{p_1 - p_2}{\ln\left(\frac{a_1}{a_2}\right)} \ln\left(\frac{r}{a_1}\right) + p_1, \quad a_1 \leq r \leq a_2. \tag{2.40}$$

The permeating flow rate is again found by combining this equation with Darcy's law and integrating the velocity at the inner boundary,

$$Q_\mathrm{p} = \frac{2\pi L k}{\eta \ln\left(1 + \frac{w}{a_1}\right)} \Delta p, \tag{2.41}$$

where $w = a_2 - a_1$ is the wall thickness, L is the length of the tube and $\Delta p = p_1 - p_2$.

Chapter 3

Fabrication and characterization of SiC-samples

We fabricated all the SiC-monotubes and plugs, used throughout the experimental part of this thesis, from scratch starting with the SiC as a clay-like material delivered by the company LiqTech. This way we got a good feeling with SiC as a material and gained insight into the process of producing filters from SiC.

In the following we first describe the fabrication method used for the monotubes and plugs, and focus in particular on our own improvements leading to specimens of high quality. Second, we shortly present a few, simple characterization methods used to check the quality of the fabricated SiC-samples, and to estimate its porosity and average pore diameter.

We are thankful to Johnny Marcher, technical director at LiqTech, for many good advice and technical discussions of SiC production methods. We are also grateful to Alexander Shapiro, associate professor, and Duc Thuong Vu, technician, both at the Department of Chemical and Biochemical Engineering, DTU, for introducing us to the Computed Tomography (CT) scanning method and for making the CT-scanner at their department available to us.

Specific comments about the fabrication process, like the composition of the SiC-material, the composition of the membranes and the sintering temperature have been omitted, as it is confidential information.

3.1 Fabrication of SiC-plugs and tubes

This section appears a bit tedious, but the fabrication process is described in detail to show how complicated it was to fabricate the high quality SiC-samples.

3.1.1 Plugs

The plugs were fabricated by mounting the SiC-clay between two pieces of paper in a press, and then pressing it into a flat plate shape, see Fig. 3.1. The paper was used to avoid

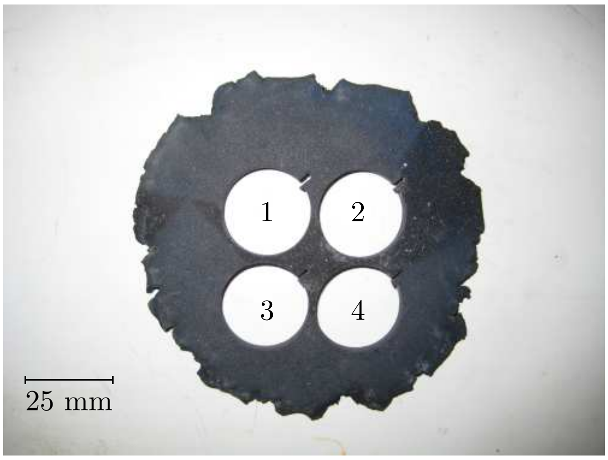

Figure 3.1: Picture of a SiC-plate after pressing, drying, sintering and removal by water-jet cutting of four circular plugs. The numbers are used to label the plugs. The water-jet cutting was done by Jesper Lybæk from the company Jaka Metal.

sticking of SiC to the press. The paper, of course, stuck to the surface of the SiC-plates, but it would be burned off during the subsequent sintering process at high temperatures.

Plates were made with four different thicknesses, 3.7 mm, 5.2 mm, 6.5 mm and 8.2 mm. To minimize the risk of crack formation in the SiC-plates no plates were made thicker than 8 mm, and they were dried slowly after pressing. The drying process consisted of placing the SiC-plates between planar pieces of wood in a room for a week at a temperature of approximately 20°C.

After drying, the plates were sintered and oxidized in a high-temperature furnace at LiqTech. The oxidization removed all the carbon molecules freed during the sintering. The sintering process lasted about four days and the oxidization about one day. When the plates had been sintered and oxidized, plugs with a diameter of 25 mm were cut out of the plates by Jesper Lybæk from the company Jaka Metal using water-jet cutting.

The plugs were named as in the following example: P6-3-6.6. 'P6' is the plate number given from approximate plate thickness, '3' is the plug number from that plate and '6.6' is the measured thickness in mm of the plug. The thickness of the plugs cut from the same plate varied slightly within ±0.1 mm. This thickness variation was probably caused by the two surfaces of the press not being completely parallel.

A total of 18 plugs were made: four plugs from each of the three plates, P3, P5 and P8, and six plugs from plate P6.

3.1.2 Monotubes

The monotubes were made by extrusion using the extruder shown in Fig. 3.2(a). As it was vital that the SiC-clay was homogeneous and did not contain any air bubbles, the material was pressed hard together and formed as rods to fit inside the cylinder of the extruder. This way the monotubes were extruded from one piece of material. If any pockets of air were present in the walls of a monotube, stresses might occur during the

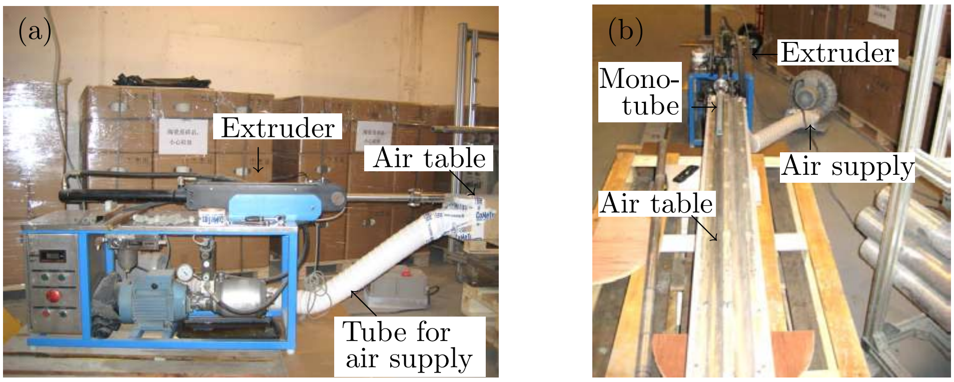

Figure 3.2: The setup with the extruder used to produce the monotubes. (a) Side-view of the setup with the extruder in the middle of the picture. The monotubes are extruded onto the air table in the right side of the picture. (b) Front-view of the setup showing a monotube being extruded onto the air table. The air supply for the air table can be seen to the right of the extruder.

drying or sintering process that could weaken the walls or even create a crack going from the channel to the surface, thereby ruining the monotube.

In the extruder a piston pushed the SiC-clay in the cylinder through the extruder head shown in Fig. 3.3. The clay was pushed into the extruder head through the small holes in the front, see Fig. 3.3(a). Inside the extruder head a cylinder was placed, the so-called inner cylinder, see Fig. 3.3(c)-(d), and the clay was forced around it, forming the channel in the monotube. The extruder head had an inner diameter of 22 mm while the inner cylinder had a diameter of 15 mm, thus giving the monotubes an outer and inner diameter of 22 mm and 15 mm, respectively. The position of the inner cylinder was adjusted with the use of three screws placed with an angle of 120° in between them on the perimeter, see Fig. 3.3(b) where the original adjustment screws are labeled '1'.

It was important that the inner cylinder was positioned exactly in the middle of the extruder head, both in order to get a uniform and circular channel in the monotube, but also because if the inner cylinder was out of position, the monotube tended to bend to one side or the other during the extrusion. It proved to be extremely difficult to position the inner channel properly. Even though we adjusted the position of the inner cylinder carefully for more than ten minutes, it seemed to be more luck than skill, if a monotube was extruded properly. The difficulties were mainly due to the inner cylinder being made out of plastic and the adjustment screws being placed only 20 mm down the length of the cylinder, see Fig. 3.3(d) where the old screw marks are labeled '7'. This meant that about 80 mm of the inner cylinder was hanging freely and since it was made out of plastic, it could then easily bend and move out of place.

It was considered that both a new inner cylinder made of a harder material than plastic, and new adjustment screws placed further down the length of the inner cylinder, would make it easier to keep the inner cylinder in place. A harder material would ensure that the screws were not screwed into the cylinder when trying to position it, and furthermore it would be harder to bend and move. New adjustment screws placed further down the length of the inner cylinder would make it easier to keep it centered. Thus we made some

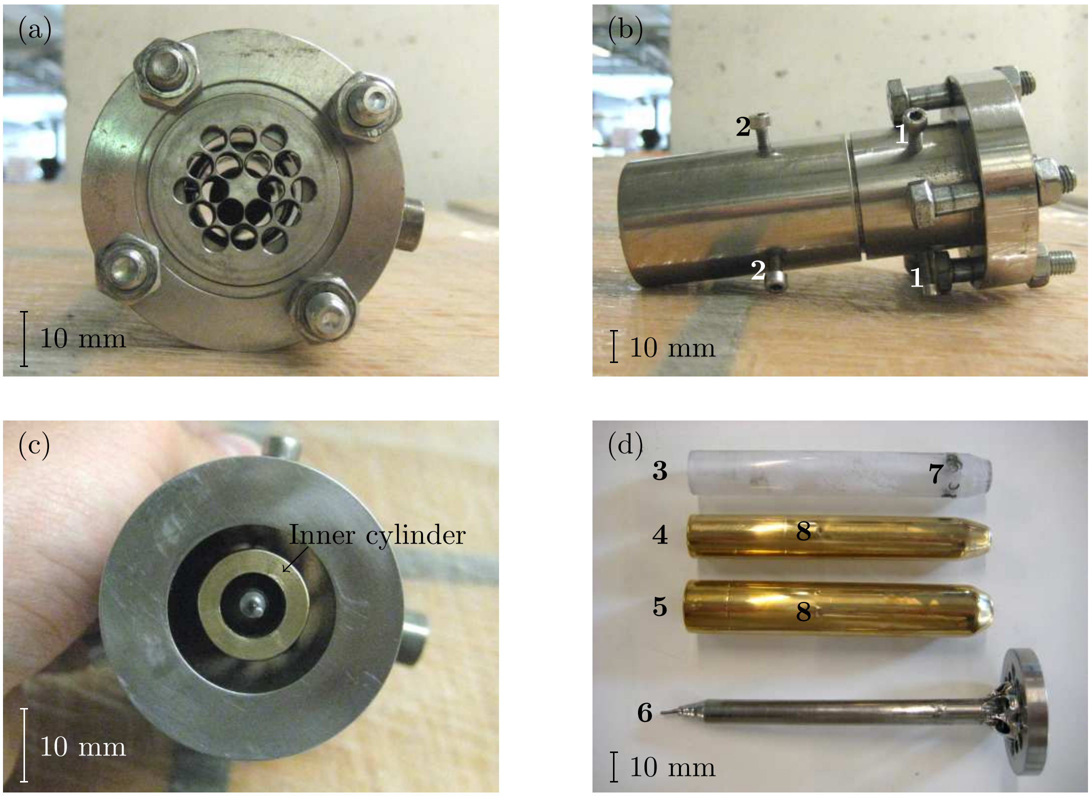

Figure 3.3: Close-up pictures of the extruder head. (a) Front-view of the extruder head. The material is pushed through the small holes and past the inner cylinder behind the holes. (b) Side-view of the extruder head showing the adjustment screws used to keep the inner cylinder in place. The old screws are labeled '1', and the new screws are labeled '2'. (c) Back-view of the extruder head. The SiC-clay is forced through the gap between the extruder head itself and the inner cylinder, thereby forming a monotube. (d) The old plastic inner cylinder ('3') is shown together with the two new brass inner cylinders ('4' and '5') and the cylinder rod ('6') on which the inner cylinders are placed. Marks from the old adjustment screws ('7') is seen on the plastic inner cylinder, while marks from the new adjustment screws ('8') is seen on the brass cylinders.

new parts for the extruder head.

We fabricated two new inner cylinders out of brass with a diameter of 15 mm and 18 mm, respectively, see Fig. 3.3(d) where they are labeled '4' and '5'. The working drawings of the new inner cylinders are shown in Appendixes F.2 and F.3. The different diameters made it possible to fabricate monotubes with two wall thicknesses, giving more options in the experiments, like measuring the dependence of the permeability of the wall thickness. The two types of monotubes produced are shown in Fig. 3.4. The monotubes do not have the exact same dimensions after being dried and sintered, as they do when extruded. This is due to a slight expansion in the material right after being extruded and then a shrinkage during the subsequent drying and sintering process. The thin-walled monotubes had a final outer diameter of 21.3 mm and a wall thickness of 2.2 mm, and the thick-walled monotubes had a final outer diameter of 21.3 mm and a wall thickness of 3.6 mm.

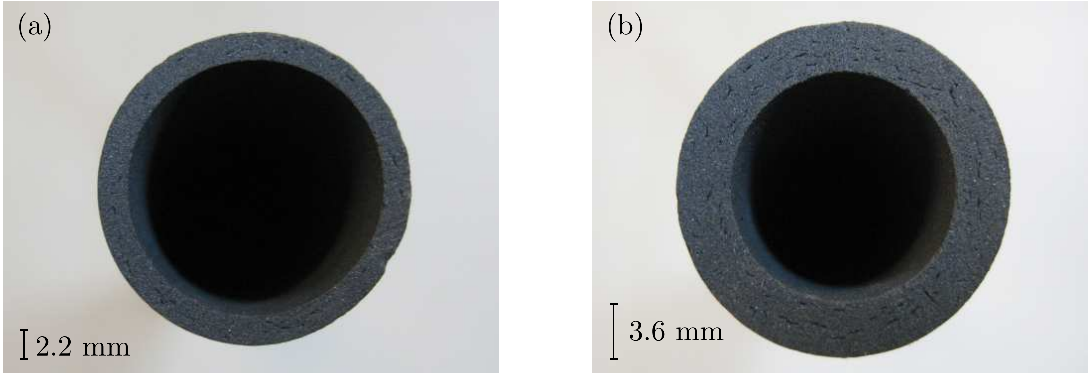

Figure 3.4: Pictures of the cross-section of the two types of monotubes made with the improved extruder. (a) A thin-walled monotube with a wall thickness of 2.2 mm. (b) A thick-walled monotube with a wall thickness of 3.6 mm. Both monotubes have an outer diameter of 21.3 mm.

We also made a new part for the extruder head with new adjustment screws, see the working drawing in Appendix F.1. In Fig. 3.3(b) the new adjustment screws are labeled '2'. The screws could not be placed too close to the end of the cylinder, since the SiC-clay had to split to pass the screws and join on the other side. The screws were therefore placed about 40 mm from the end of the extruder head. Furthermore the screws were made thin to prove as small an obstacle as possible.

During the extrusion of the monotubes it was important that the piston pushed the SiC-clay through the extruder head at the right speed. If it went too slow, the monotubes might get an elliptical shape, before being put at the drying table. If it went too fast, the clay would not have time enough to join after passing the adjustment screws. Through trial-and-error we found the best speed of the piston to be approximately 12 cm/min when extruding the thick-walled monotubes, and approximately 4 cm/min when extruding the thin-walled monotubes.

The monotubes were extruded out onto a table provided by LiqTech, the so-called air table, shown in Fig. 3.2(b), with a channel formed as the bottom half of a cylinder. Air could be blown out through small holes in the bottom of the channel, making the monotubes hover and reducing the friction significantly. Thereby the monotubes would not be dragged out of form during the extrusion. From the air table the monotubes were put into aluminum pipes to keep them straight and then left to dry in a drying box. During the drying process the aluminum pipes had to be turned often (at least every 2–3 minutes) so the monotubes kept their circular shape. In practice this was not doable, since the drying process took several hours and we had to turn the pipes by hand. Therefore all the monotubes dried this way got a slightly elliptical shape.

To avoid the monotubes getting an elliptical shape, LiqTech provided a table on which the aluminum pipes with the monotubes could be placed between two wheels and be turned at a constant velocity during the drying. Furthermore a fan was used to blow air through holes in a plate at the end of the table, see Fig. 3.5. By placing the aluminum

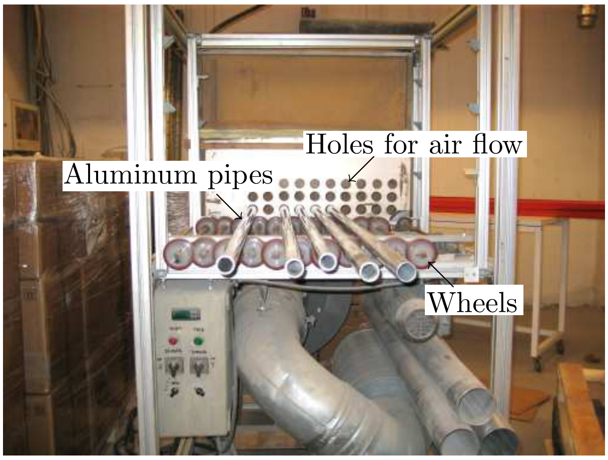

Figure 3.5: Table used to dry the extruded monotubes. The aluminum pipes were turned at a constant velocity by the wheels while air was blown through the aluminum pipes in order to dry the monotubes faster.

pipes in front of these holes, the drying time of the monotubes could be reduced. The air flow could not be too high, though, as cracks could appear in the monotubes if the surface dried too fast compared to the middle of the walls. Through trial-and-error we found an appropriate air flow using tape at the inlet of the aluminum pipes. The tape was used because the regulator for the fan was broken, setting the fan to maximum speed.

The monotubes dried faster upstream, since the air could absorb more moisture here. Further downstream less moisture could be absorbed due to the air becoming saturated, slowing the drying process. To optimize the drying process we turned the aluminum pipes 180° every 30 minutes during the first three hours. Hereafter the pipes were turned once every hour until the monotubes were dry. The drying process lasted about five hours for the thin-walled monotubes and eight hours for the thick-walled monotubes. Finally, the dried monotubes were sintered and oxidized in the same way as the plugs.

To sum up, the most important improvements we made to obtain the best possible monotubes are:

Monotubes extruded from one piece of material. The SiC-clay delivered by LiqTech was formed as rods with a diameter and length to fit inside the cylinder of the extruder thereby minimizing the risk of air pocket formation in the walls of the monotubes during extrusion.

New adjustment screws for the extruder head. The original adjustment screws on the extruder head were placed too close to the front, making it next to impossible to center the inner cylinder accurately and it was easy to move the inner cylinder out of place. A new part for the extruder head was therefore made with adjustment screws placed closer to the end of the extruder head.

New inner cylinder made from a harder material. The original inner cylinder was made out of plastic. This meant that the adjustment screws could be screwed into the surface of the cylinder, making it difficult to position it properly. Also the soft plastic bend easily and moved during extrusion. Thus new inner cylinders were made out of brass.

Improved drying table. During drying, the monotubes tended to get an elliptical shape if they were not turned often for several hours. Thus a drying table was used on which the monotubes could be rotated at a constant velocity while drying.

Initially only the thick-walled monotubes could be made as only one inner cylinder was available. The fabrication of the first three series of these monotubes was therefore used to improve the fabrication method. In the experimental setup the monotubes had to have a length of 305 mm to fit the housing. Since the thick-walled monotubes could be extruded to a length of about 500 mm from one piece of material, only one monotube could be cut from each extruded length. The thick-walled monotubes were then named as in the following example: IV-XV. 'IV' is the number of the series and 'XV' is the tube number from that series.

The naming of the thin-walled monotubes was slightly different. The thinner walls meant that the monotubes could be extruded to a length of 1.1 m from one piece of material, which made it possible to get up to three monotubes with a length of 305 mm from each extruded length. One long monotube with a length of 1 m could also be cut, that fit in a long housing. Thus thin-walled monotubes with two different lengths were made. The long thin-walled monotubes were named as in the following example: TI-XI. 'TI' means it is a thin-walled tube from the first series and 'XI' is the tube number from that series. The short thin-walled monotubes were named as: TI-VI-II. 'TI' again describes it as a thin-walled tube from the first series, 'VI' is the tube number extruded in that series and 'II' is the number of the short monotube cut from that tube length.

We fabricated a total of 20 thick-walled monotubes, with 12 of these being of good quality, in the final 4th series. All of these had a length of 305 mm, an outer diameter of 21.3 mm and a wall thickness of 3.6 mm. 38 short and four long thin-walled monotubes of good quality were fabricated from a total of 23 extruded tubes. All of the thin-walled monotubes have an outer diameter of 21.3 mm, and a wall thickness of 2.2 mm.

3.1.3 24-channel tubes

A set of tubes, called 24-channel tubes, containing many parallel channels was also fabricated, see Fig. 3.6. The channels are quadrilateral in shape and have a width of 3 mm. There are 16 full channels in the middle of the design, while the outer channels, cut to follow the circular shape of the tube, combine to approximately 8 full channels, thus explaining the name 24-channel tube. The walls have a thickness of 1 mm.

The 24-channel tubes are used in order to introduce a complex geometry in our experimental work that actually is used by CoMeTas in some of their membranes. It was not possible to fabricate the 24-channel tubes with the extruder used for the monotubes and they were instead fabricated by LiqTech. They were named as in the following example: XXIV-IV. 'XXIV' denotes "24-channel tube" and 'IV' is the specific tube number. A total of 20 24-channel tubes were fabricated, all of them having a length of 305 mm.

Figure 3.6: Picture of the cross-section of a 24-channel tube. The channels have a width of 3 mm and the walls have a thickness of 1 mm. The outer diameter of the tube is 25 mm.

3.1.4 Coating

The surface of the channels in the membranes produced by CoMeTas are coated with a thin SiC-membrane layer, and this is an essential part of their membranes. The membrane layer consists of small SiC-particles, and by changing the size of the particles the pore size in the membrane layer can be changed. The different types of membrane layers are named from their estimated mean pore size.

We coated some of the thin-walled monotubes and 24-channel tubes using the same procedure as CoMeTas. The membrane was mixed as a liquid and the channels of the tubes were coated with the membrane using a method called the dip coating method. In practice the tubes were positioned vertically and the membrane liquid was let into the channels from the bottom and slowly rising until it reached the top of the tubes and then the liquid level was decreased slowly again. By doing this a thin membrane film was left on the surface of the channels. When the membrane film was dry, the tubes were sintered and oxidized in the same way as mentioned above.

The tubes were coated twice with two different membrane layers. The first layer, called the middle layer, consists of relatively big particles and has a mean pore size of 1 µm. When the tubes had been coated with this membrane and sintered, they were coated with a membrane consisting of smaller particles. Two different types of membrane were used. The membrane used most often by CoMeTas has a mean pore size of 0.04 µm, therefore ten thin-walled monotubes and eight 24-channel tubes were coated with this membrane. CoMeTas also uses another membrane with a mean pore size of 0.1 µm, and four thin-walled monotubes and four 24-channel tubes were coated with this membrane.

It took about two weeks to coat the tubes first with the middle layer and then with the two types of membrane and sinter and oxidize them after each coating. Total production time of the tubes and plugs was approximately four weeks.

3.2 Characterization methods

The characterization methods described here have been abridged, and only the most important results are described.

3.2.1 CT-scan

We introduced the method of Computed Tomography scanning (CT-scanning) to CoMeTas in our studies of the homogeneity and quality of the porous SiC-tubes and plugs. CT-scanning is a medical imaging method, where digital geometry processing is used to generate a three-dimensional image of the inside of an object from a large series of two-dimensional X-ray images taken around a single axis of rotation. A CT-scan produces a volume of data which can be manipulated, in order to demonstrate various structures based on their ability to block the X-ray beam. The CT-scanner can thus be used to verify, if the SiC-tubes and plugs are homogeneous, or if holes or cracks are present, and thereby we can determine if the tubes and plugs are of high or low quality.

Unfortunately the CT-scanner available to us broke down during the summer 2008 and was not repaired before the end of our thesis work. Therefore we could not CT-scan the plugs and tubes used in our experimental work. However, we made some pictures of some of the thick-walled monotubes initially fabricated in our two first series of monotubes. A CT-picture of the cross-section of monotube II-V is shown in Fig. 3.7(a). The white areas on the surface of the monotube arise, when the different pictures are combined. Inside of the white edges the porous material seems quite homogeneous, due to the uniform grey color. If air in the form of a crack or hole is present in the material, it would appear as a black area (like the channel in the tube). The so-called CT-number, which is an expression of the amount of X-rays penetrating the object, can be used to determine, whether the object contains cracks, holes, or any sort of impurities. In Fig. 3.7(b) a black area is clearly seen in the upper region of the monotube. Judged from the color, this black area is most likely a hole in the material, which could either have been created during the extrusion, or when the tube was dried and subsequently sintered.

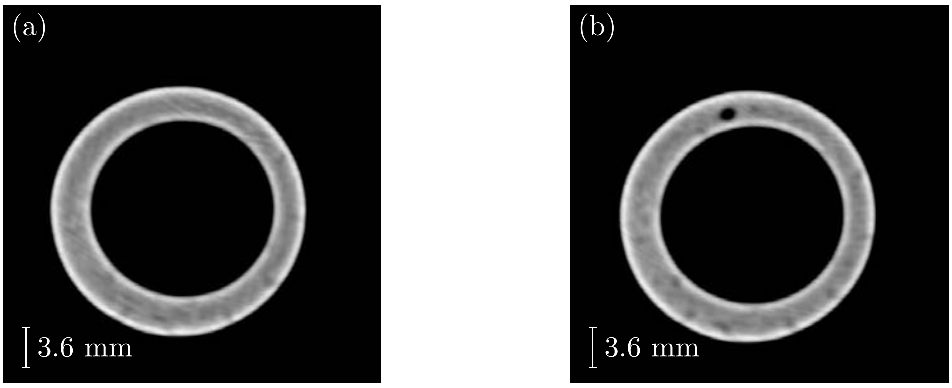

Figure 3.7: (a) CT-picture of the cross-section of monotube II-V showing no sign of any holes or cracks. (b) Another CT-picture of II-V showing a hole in the upper region.

3.2.2 Porosity

The porosity ϕ_{SiC} of the SiC used in our plugs and tubes can be found from a simple experiment with the thin-walled and thick-walled monotubes, see Appendix A.1. We used ten thin-walled and eight thick-walled monotubes for this porosity experiment. The mean porosity, in %, of the SiC was found to be

$$\phi_{\mathrm{SiC}} = (38.2 \pm 0.8)\%, \tag{3.1}$$

where the error is the standard deviation of the porosities found from each of the monotubes. A porosity of approximately 40% was expected for the SiC, and our results agree well with these expectations.

3.2.3 Capillary rise

One way to determine the mean pore size d_{m} of a porous medium, is by use of the capillary rise method described in Appendix A.2. The contact angle θ at the water-SiC-air contact line is unknown, but as a rule of thumb it can be assumed to be $\theta = 0°$ for very hydrophilic materials. Three long monotubes were used for the capillary rise experiment and using $\theta = 0°$ the average pore size was found to be approximately $d_{\mathrm{m}} = 27\,\mu\mathrm{m}$ which is nearly three times higher than the expected pore size of around 10-12 µm. The contact angle should be more than 60° in order to obtain the expected average pore size in the porous media.

We made a small observation during the preliminary experiments concerning the capillary rise. Surprisingly, the first SiC-tubes we used showed no sign of water rise. We discovered that this was because the tubes had not been oxidized, and thus we found that an easy way to see, if our tubes and plugs had been oxidized, was to check if they could absorb water.

3.2.4 Bubble point

The maximum pore size $d_{\max}$ as well as the homogeneity of our plugs and tubes, can be found using the so-called bubble point method described in Appendix A.3. Using 13 monotubes the average maximum pore diameter is found to be approximately 16 µm, when a contact angle of $\theta = 0°$ is assumed. As mentioned, the mean pore diameter is expected to be around 10-12 µm, and it is expected that the maximum pore diameter is only slightly larger. Thus, our results agree well with our expectations at a contact angle of $\theta = 0°$, opposed to the results found in the capillary rise method. The reason for this is unknown and has not been investigated further.

The bubble point test can be used not only for estimating the maximum pore diameter, but may also indicate if our plugs and tubes are damaged. If bubbles form at a lower pressure than expected, and only in one region of the SiC-sample, it could indicate a hole or a crack in the sample.

Since the results from the capillary rise method and the bubble point method do not agree, no conclusions are made from the methods presented here. The methods are still usable, however, as they give useful information concerning the quality of the SiC-samples.

Chapter 4

Experimental setup

The setup used for the experimental part of this thesis was provided by CoMeTas. It was installed at the new premises of the company when our work was initiated. In the following we give a brief description of the setup and present only the most important information relevant for our work. In particular we focus on the thorough check and improvements we had to make on this new setup to obtain satisfactory results. In total we spent two months of work to get the setup fully operational.

4.1 Description of the experimental setup

Basically the setup consists of four valves (V01–V04), one pump (P01), three adjustable valves (AV01–AV03), two flow transmitters (FT01 and FT02), three pressure transmitters (PT01–PT03) and one temperature transmitter (TT01). The position of the different parts on the experimental setup can be seen in the sketch of Fig. 4.1 and the pictures of Fig. 4.2. The specifications of the components are listed below.

Valves: 2/2-way angle seat valve, type 2000 DN 40 (Bürkert Fluid Control Systems).

Pump: CRNE 5-16 multistage centrifugal pump with MGE 90 engine. 16-stage pump with nominal flow rate of $5.7\,\mathrm{m^3/h}$ (Grundfos).

Adjustable valves: Piston actuated angle seat valve, type 2702 DN 40, with side control positioner 1067 (Bürkert Fluid Control Systems).

Flow transmitters: Sitrans F M Magflo electromagnetic flowmeter. Sensor type: MAG 3100 HT, DN 40, with PTFE liner. Converter type: MAG 5000 IP 67. Measuring range: $0\,\mathrm{L/s}$ – $2.5\,\mathrm{L/s}$. Error from calibration report: ±0.09% at 90% of full-scale flow; ±0.12% at 25% of full-scale flow (Siemens Instruments).

Pressure transmitters: Siemens Sitrans P, series Z. Measuring range of original transmitters: $0\,\mathrm{bar}$ – $16\,\mathrm{bar}$. Measuring range of new transmitters[1]: two transmitters

---

[1] The new pressure transmitters will be discussed in Section 4.2

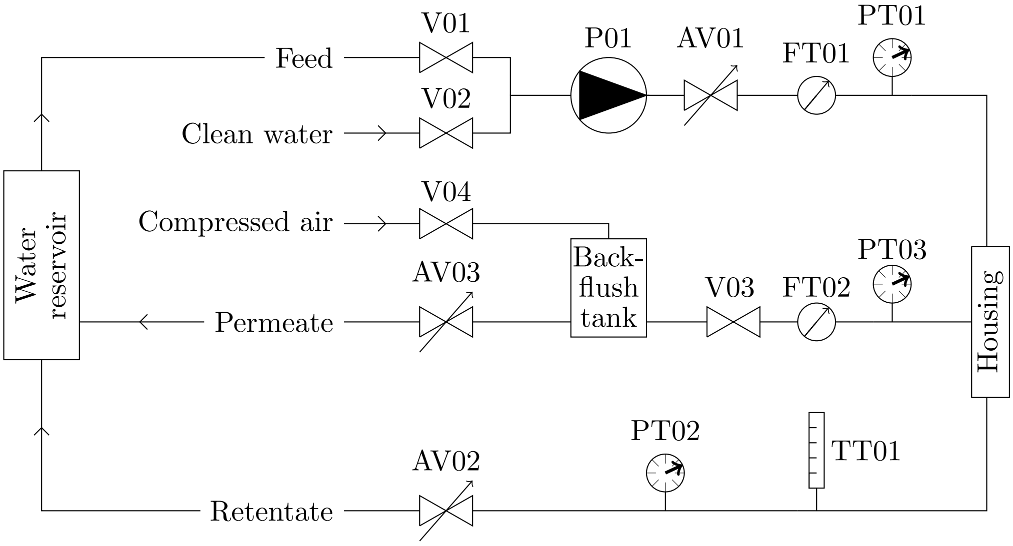

Figure 4.1: Diagram of the initial experimental setup containing four valves (V01–V04), a pump (P01), three adjustable valves (AV01–AV03), two flow transmitters (FT01 and FT02), three pressure transmitters (PT01–PT03) and a temperature transmitter (TT01). The plugs and tubes used in the experiments are positioned in the housing. In a cross-flow setup the experimental setup is used as shown in this diagram, but when dead-end experiments are conducted the permeate flow is let out through the retentate exit in order to measure the temperature. Thus the permeate exit is not used in the dead-end setup. The demineralized water is recirculated in the water reservoir.

with range 0 bar – 4 bar and one with range 0 bar – 1.6 bar. Maximum error: ±0.5% of full-scale value (Siemens Instruments).

Temperature transmitter: Siemens Sitrans TF2. Measuring range: from -50°C to +200°C. Maximum error: ±0.5% of full-scale value (Siemens Instruments).

During the experiments the pump was used to control the feed pressure p_f and thus the flow rate Q through the plugs and tubes. In the cross-flow experiments the adjustable valves on the retentate and permeate (AV02 and AV03, respectively) were used to control the retentate and permeate pressure (p_r and p_p, respectively) behind the tubes and thus the amount of flow coming through the retentate and permeate. The temperature transmitter measures the temperature of the retentate flow when conduction cross-flow experiments, and in order to measure the fluid temperature in the dead-end setup, the permeate flow is let through the retentate exit in these experiments. Thus the permeate exit is not used when conduction dead-end experiments. The dead-end and cross-flow setups are described in Section 4.1.2. The valves and the pump are controlled directly on the experimental setup, using a control panel. All the data from the pump, valves and transmitters are logged on a computer connected to a PLC-server on the experimental setup. The water used in the experiments is recirculated in the water reservoir, labeled '7' in Fig. 4.2(a). It is led from the reservoir into the setup through the feed inlet (label '6' in Fig. 4.2(b)) and out into the reservoir again through the retentate and permeate outlets ('4' and '5', respectively, in Fig. 4.2(b)).

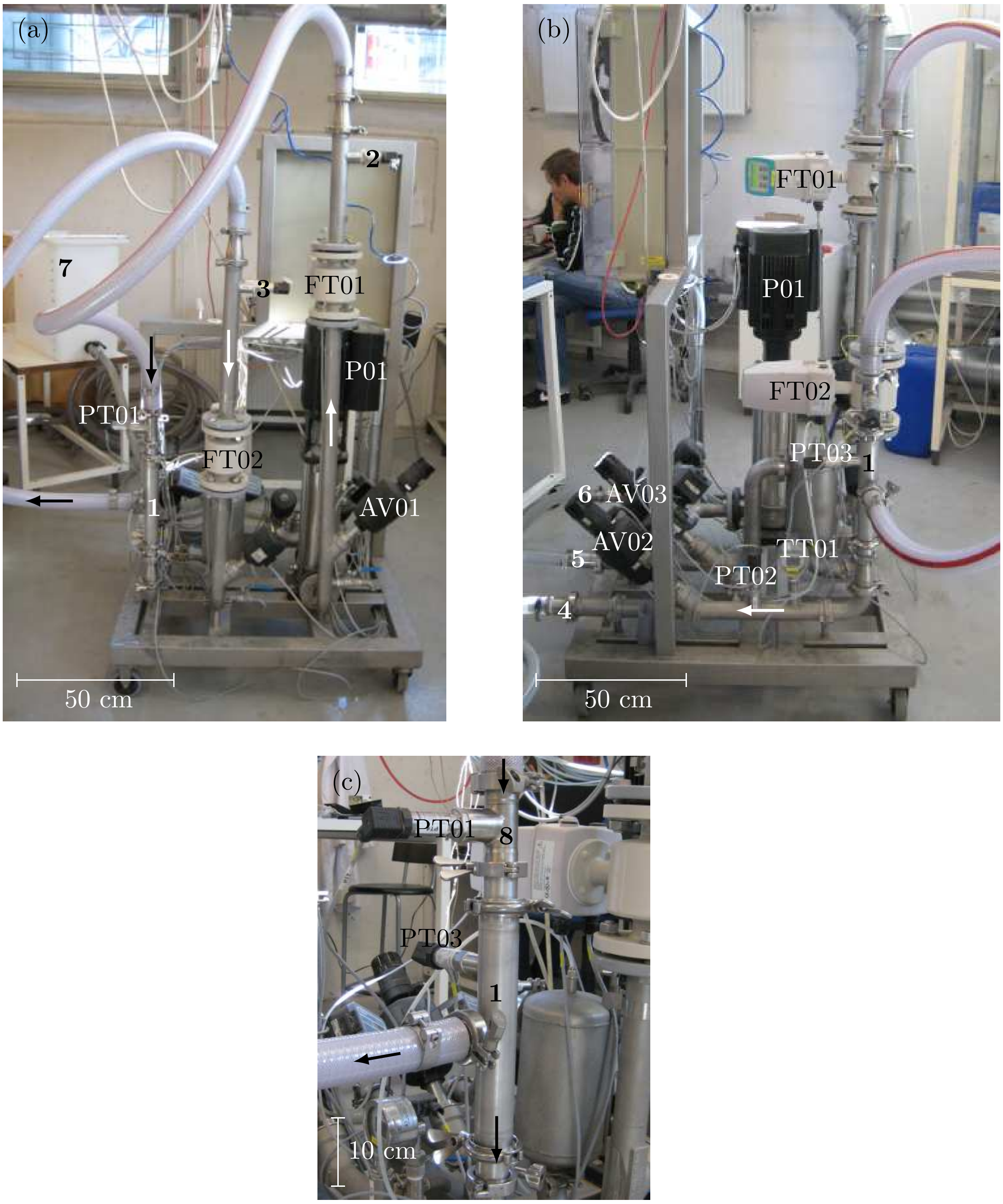

Figure 4.2: Pictures of the experimental setup. The arrows represent the flow direction. The labels of the different parts are the same as in Fig. 4.1. (a) Back-view of the setup. The housing containing the plugs and tubes marked '1'. (b) Side-view of the setup. (c) Zoom of the housing. Initial position of the pressure transmitters on feed ('2') and permeate ('3'), retentate ('4') and permeate ('5') outlet, feed inlet ('6'), water reservoir ('7'), extra pipe part for pressure transmitter ('8').

The initial position of the pressure transmitters used to measure the feed pressure and the permeate pressure is shown in Fig. 4.2(a) (labeled '2' and '3'). The extra pipe part we made to mount a pressure transmitter on is seen in Fig. 4.2(c) (labeled '8'). The reason why we changed the position of these transmitters and made an extra pipe part will be discussed in Section 4.2.

Furthermore the setup has a so-called back-flush tank, which is filled with water during the experiment. If a filter cake builds up in a filter, the cake can be loosened by flushing back through the filter using the water in the back-flush tank. We only worked with clean water in our project and therefore we did not use this tank. During our initial plug measurements we used ordinary tap water. At later stages we used the demineralized water made available to us.

4.1.1 Setup for plug experiments

The plugs were mounted in the housing as shown in Fig. 4.3 and used in a dead-end flow setup. In practice, the housing was positioned vertically as shown in Fig. 4.2(c), and the permeate flow was guided through the retentate exit (labeled '4' in Fig. 4.2(b)).

The pressure transmitter positioned at the housing, PT03, was used to measure the feed pressure using a pressure transmitter with a range of 0 bar – 4 bar. At the permeate side of the plug the water was led into an open pipe, and the permeate pressure was therefore equal to the atmospheric pressure.

Because of the low flow rate in the plug experiments, the flow transmitters on the experimental setup could not be used. We therefore decided to measure the flow rate by weighing the amount of water penetrating the plug during a given period of time. In order to minimize the error on the measured flow rate, a sampling time of 3 minutes was used. We checked if this was an acceptable way to measure the flow rate by making ten consecutive measurements at two different pressure levels, with one pressure level being

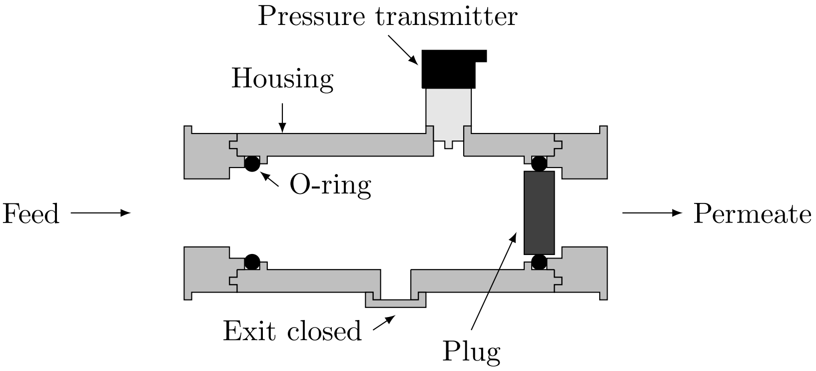

Figure 4.3: Cross-section of the cylindrical housing (light grey) showing the setup with a plug (dark grey) mounted in the housing. For clarity the dimensions of the housing have been altered on the sketch. The pressure at the feed side of the plug is measured at the housing, while the pressure at the permeate side is the atmospheric pressure. In the experiments the housing is positioned vertically with the plug facing downwards.

in the low end of the measuring range and the other in the high end. The maximum deviation from the mean value at the two pressure levels was 3%.

The plugs were mounted in the housing with an O-ring and it was made sure that no water passed the plugs without going through them. We checked this by making two plugs impermeable with glue. The plugs were then put in the housing and the pressure increased up to our maximum pressure of 4 bar. No leakages were observed and we concluded that the sealing of the plugs was tight.

4.1.2 Setup for tube experiments

The monotubes and the 24-channel tubes were mounted with O-rings in the housing in much the same way as the plugs as shown in Fig. 4.4. A pressure transmitter with a range of 0 bar – 1.6 bar was used to measure the permeate pressure at the housing.

Cross-flow setup

In the cross-flow experiments the setup was used as shown in Fig. 4.2. The extra pipe part was mounted just before the housing and the feed pressure was measured here using the pressure transmitter called PT01. The retentate pressure was measured using PT02 after the housing. Both PT01 and PT02 had a range of 0 bar – 4 bar. As Fig. 4.2(b) shows, PT02 is positioned slightly below the housing and therefore measures a too high pressure due to the hydrostatic pressure implied by the height difference. During the data processing we compensated for the hight difference to get the pressure just after the housing.

The feed flow rate Q_f was measured using FT01 while the permeate flow rate Q_p was measured using FT02. The retentate flow rate Q_r could then be calculated as $Q_\mathrm{r} = Q_\mathrm{f} - Q_\mathrm{p}$.

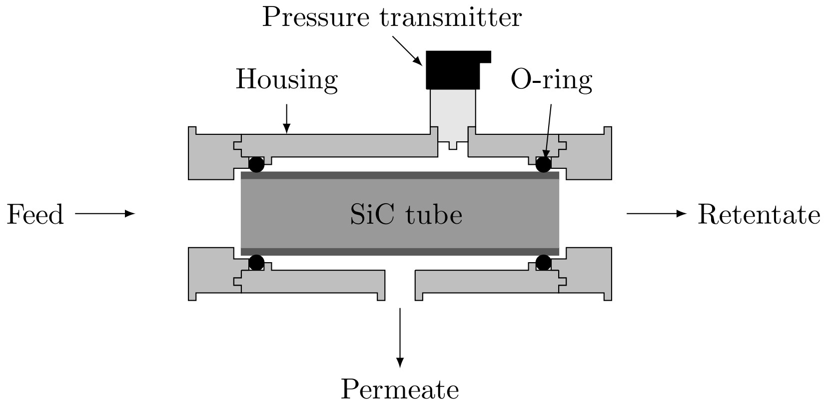

Figure 4.4: Cross-section of the cylindrical housing (light grey) showing the setup with a tube (dark grey) mounted in the housing. For clarity the dimensions of the housing have been altered on the sketch. The pressure transmitter mounted at the housing is used to measure the permeate pressure.

Dead-end setup

We changed the setup slightly for the dead-end experiments. The housing was mounted horizontally at the retentate outlet so that the temperature transmitter could be used. Since the experiments could go on for a day with the water being recirculated through the setup, the water temperature might rise. In order to measure this temperature change the water had to flow past the transmitter.

In this setup PT02 was used to measure the feed pressure, while the pipe part with PT01 was mounted after the housing to measure the possible pressure change down the length of the tube. The pipe part was as well used to seal the retentate exit on the housing. The flow rate was measured using FT01.

Most of the tube experiments were conducted using the dead-end setup.

4.2 Improvements of the experimental setup

As mentioned the experimental setup was new, when we began our experiments. Therefore, we checked the setup thoroughly before the experiments were conducted.

All three pressure transmitters (feed, retentate and permeate) were positioned some distance away from the housing where the pressures should be measured, see Fig. 4.2. To see if there might be a pressure difference between where the pressure was measured and where we wanted to know the pressure, we calculated the pressure drops in the setup at a low and a high flow rate. At the feed and retentate, flow rates of $Q_\mathrm{f} = Q_\mathrm{r} = 1\,\mathrm{m}^3/\mathrm{h}$ and $Q_\mathrm{f} = Q_\mathrm{r} = 4\,\mathrm{m}^3/\mathrm{h}$ were used while $Q_\mathrm{p} = 0.5\,\mathrm{m}^3/\mathrm{h}$ and $Q_\mathrm{p} = 2\,\mathrm{m}^3/\mathrm{h}$ were used as permeate flow rates. We calculated the pressure drops using equations found in chapter 8 in [3] and the calculations are given in Appendix B. Smooth pipes are assumed throughout all the calculations and it is assumed that the housing is mounted vertically as shown in Fig. 4.2.

From the calculations we found that the pressure drop from the feed pressure transmitter (PT01) to the housing would be in the order of $\Delta p = 0.3\,\mathrm{bar}$ at a flow rate of $4\,\mathrm{m}^3/\mathrm{h}$ which corresponds to an error of approximately $\varepsilon = 15\%$ on the measured feed pressure. A pressure drop of $\Delta p = 0.1\,\mathrm{bar}$ was calculated between the housing and the permeate pressure transmitter (PT03) corresponding to an error of almost $\varepsilon = 100\%$ at a flow rate of $2\,\mathrm{m}^3/\mathrm{h}$. By compensating for the hydrostatic pressure measured by the retentate pressure transmitter (PT02) the pressure drop was negligible here at both the low and the high flow rate.

The pressure drops at the feed and permeate were mainly due to two narrow tubes with a diameter of $D = 20$ mm connecting the housing with the transmitters. We changed these tubes with tubes having a diameter of $D = 45$ mm thereby reducing the resistance in the tubes by a factor of $2.25^4 \approx 25$, assuming laminar flow. Even with the reduction of the tube resistance significant pressure drops in the order of $5 - 10\%$ at high flow rates between the housing and PT01 and PT03 were found. In the end we therefore decided to simply move the transmitters closer to the housing. We placed PT03 on the housing itself and made a small pipe part for PT01, which could be placed just before the housing, see Fig. 4.5. This way the approximately correct pressures were measured.

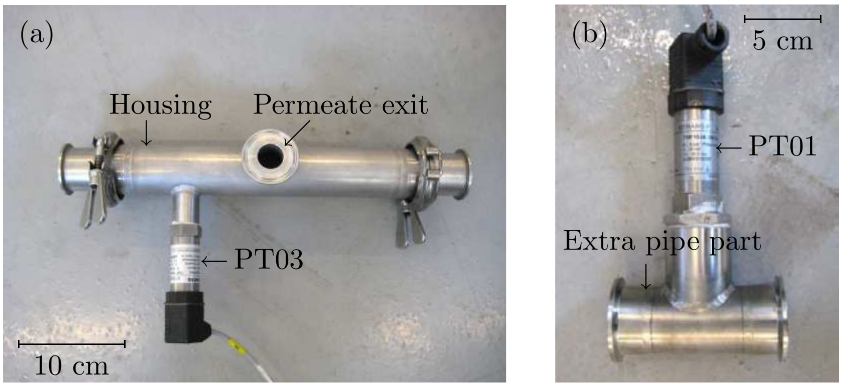

Figure 4.5: New parts made for the experimental setup. (a) The permeate pressure transmitter PT03 was mounted on the housing. (b) An extra pipe part for the feed pressure transmitter PT01 was made which could be mounted just before the housing.

The pressure transmitters delivered with the experimental setup had a measuring range of 0 bar – 16 bar. We only needed to measure in a range of about 0 bar – 4 bar on the feed and retentate and 0 bar – 1 bar on the permeate so a range of 0 bar – 16 bar was very high. The maximum error on the pressure transmitters was given as $\varepsilon = \pm 0.5\%$ of the full-scale value and the error on the pressure could then be reduced by getting pressure transmitters with a lower range. We therefore purchased two pressure transmitters with a range of 0 bar – 4 bar for the feed and retentate and one transmitter with a range of 0 bar – 1.6 bar for the permeate. In Table 4.1 the maximum error at different pressures is given for the initial and the new pressure transmitters. By getting the new transmitters we reduced the error on the measured feed and retentate pressure by a factor of four, while it was reduced by a factor of ten on the permeate.

We checked that the error on both the new and old pressure transmitters was within the maximum error stated by Siemens Instruments, and the control measurements showed that the measured error was well within the maximum error on all the pressure transmitters. It was not necessary to check the flow transmitters as these had been checked by Siemens Instruments before delivery and a maximum error of $\varepsilon = \pm 0.12\%$ had been found.

Below the improvements we made on the experimental setup are listed:

New tubes. The original tubes connecting the housing with PT01 and PT03 had very

Table 4.1: Maximum relative error ε, in %, at different working pressures for pressure transmitters with different measuring ranges.

p [bar]	ε [%] [0 bar – 16 bar]	ε [%] [0 bar – 4 bar]	ε [%] [0 bar – 1.6 bar]
0.1	80	20	8
0.5	16	4	1.6
1	8	2	0.8
3	2.7	0.7	-

small diameters. We acquired new tubes with a larger diameter which reduced the pressure drop in the tubes by a factor of approximately 25, assuming laminar flow and constant velocity.

Changed position of PT01 and PT03. PT01 and PT03 were placed too far from the housing, thus they did not measure the correct pressures. We changed their position and mounted PT03 on the housing while an extra pipe part was made for PT01 which could be mounted in front of the housing.

New pressure transmitters. The initial pressure transmitters had a too high measuring range of 0 bar – 16 bar which resulted in an unacceptable high error in the used measuring range. We purchased two new pressure transmitters for the feed and retentate with a range of 0 bar – 4 bar and one for the permeate with a range of 0 bar – 1.6 bar. Thus we reduced the error on the measured feed and retentate pressure by a factor of four and on the permeate pressure by a factor of ten.

Chapter 5

Experiments with SiC-substrates

In the following we first present our experiments with the simple SiC-plugs of four different thicknesses followed by the monotubes of two different wall thicknesses. The purpose of these experiments is to confirm Darcy's law for flow in porous materials, to find the permeability of the porous SiC, and to investigate if the permeability is independent of the thickness of the SiC.

Second we present our experiments with the 24-channel tubes. The goal is to get some experimental data with a more complicated geometry which can be compared to the results from our simulations and thereby verify our numerical models.

The experiments in this chapter represent two months of experimental work. During the plug experiments, three weeks were used to solve some encountered problems regarding contamination of our plug samples. We are thankful to Jørgen Wagner, senior application manager at CoMeTas, for discussions of the contamination problems, and for his good advice on how to solve them.

5.1 Plugs

The simplest way to measure the permeability of the porous SiC and to verify Darcy's law, was to make a plug out of SiC and force the water flow through it, i.e. use the plug as a dead-end filter. A 1D flow can then be assumed in the plug, and Darcy's law is given from Eq. (2.16). Assuming 1D flow in the plugs the permeating flow rate Q_p can be found from Eq. (2.39). Rewriting this equation slightly gives

$$Q_\mathrm{p} = \frac{\pi d^2 k}{4\eta w} p_\mathrm{tm}, \tag{5.1}$$

where d is the diameter of the plug and $p_\mathrm{tm} = p_\mathrm{f} - p_\mathrm{p}$ is the transmembrane pressure with p_f being the feed pressure and p_p the permeate pressure. The pressures are given as gauge pressures. The flow rate and the pressure are measured during the experiments, while η, d and w are known values. Thus, k can be found from Eq. (5.1). As mentioned in Chapter 4, ordinary tap water is used in the plug experiments since demineralized water was unavailable at the time the experiments were conducted. The water was kept at 20°C

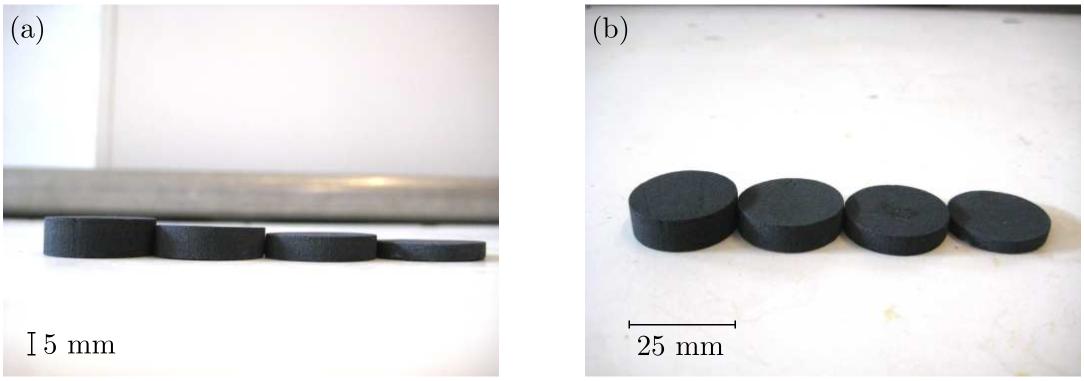

Figure 5.1: The four different plug thicknesses used. (a) Side-view of the plugs. From left to right, the plug thicknesses are 8.2 mm, 6.5 mm, 5.2 mm and 3.7 mm. All plugs have a diameter of 25 mm. (b) The same seen slightly from above.

at all times, thus $\eta = 10^{-3}\,\text{Pa s}$. We assume that the viscosity η of demineralized water and tap water is identical.

As described in Section 3.1.1 we fabricated plugs with four different thicknesses, 3.7 mm, 5.2 mm, 6.5 mm and 8.2 mm, see Fig. 5.1. Different thicknesses were produced in order to see how the flow rate through the plugs changed with the plug thickness and, more importantly, to see if the permeability was independent of the thickness. All plugs were produced with a diameter of 25 mm.

As described in Section 4.1.1 the pressure at the feed side of the plug is measured at the housing (see Fig. 4.3) while the permeate pressure is equal to the atmospheric pressure. This meant that $p_\text{p} = 0\,\text{bar}$ at all times during the plug experiments and $p_\text{tm} = p_\text{f}$. The pressure on the feed side was controlled by changing the efficiency of the pump. A plot of a raw data file of the measured pressure is shown in Fig. 5.2(a). The time scale of a complete measurement was typically around 40 minutes and the pressure was measured with a frequency of $f = 0.2\,\text{Hz}$. As the graph shows, the pressure was changed in steps from around 0.4 bar to 4 bar. The pressure was kept constant at each level for a given time in order to check that both the pressure and the flow rate was stable and to minimize the error on the measurements.

In Fig. 5.2(b) a zoom of one of the pressure steps is shown. The blue colored points in the figure are used to find the time averaged mean value of the pressure. When the pressure was changed it took a short while before the pressure and flow rate was stable. It tended to be a bit too high in the beginning before reaching a stable level, as Fig. 5.2(b) also shows. Therefore the first ten data points — referring to the first 50 seconds of each pressure step — are omitted from the mean value of the pressure. Also the last two data points are omitted to make sure that any eventual deviations in the end of a pressure step are not taken into account. To make sure that the flow rate was stable when it was measured, the flow rate measurement was only initiated approximately one minute after the pressure had been changed. From Eq. (5.1) we know that the measured flow rate and

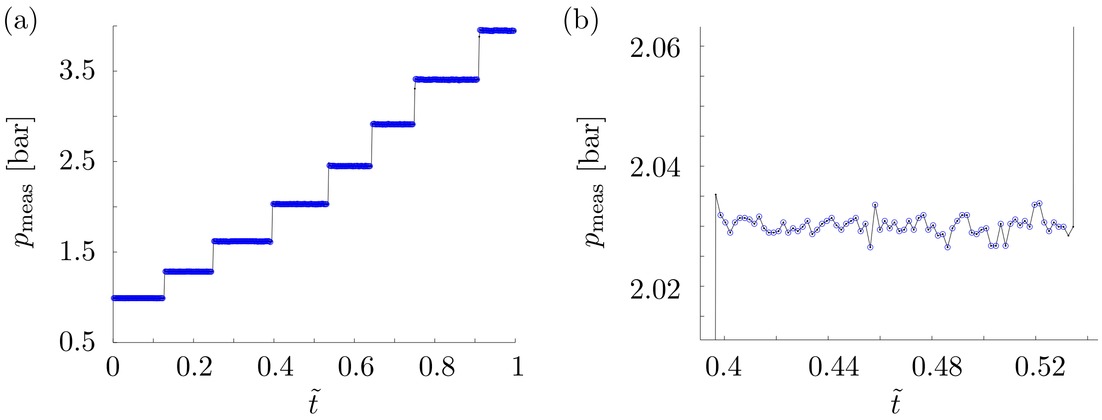

Figure 5.2: (a) Typical plot of the measured pressure p_{meas} at the housing as a function of normalized time, $\tilde{t} = t/T$. The time scale T of one measurement is typically around 40 minutes. The sampling frequency of the pressure was $f = 0.2\,\text{Hz}$. The pressure was increased or decreased stepwise by increasing or decreasing the pump efficiency. (b) A zoom of one of the pressure steps. A time averaged mean value of the pressure is found using the blue colored points between $\tilde{t} = 0.40$ and $\tilde{t} = 0.53$.

pressure should be linearly related on the form

$$Q_{\text{p}} = a p_{\text{tm}} + b, \tag{5.2}$$

where a and b are constants found by least-squares fitting.

5.1.1 Errors on the measured data

As mentioned in Section 4.1, the maximum error on the pressure transmitters is assumed to be ±0.5% of the full-scale value by Siemens Instruments. Our control measurements showed that the error was well within this range, but the maximum error is still used as the error on all the pressure measurements to be on the safe side. Since the pressure transmitter on the feed side had a range from 0 bar to 4 bar, the error on the transmembrane pressure was $\varepsilon_{p_{\text{tm}}} = 0.02\,\text{bar}$.

The error ε_{Q} on the flow rate is found from

$$\varepsilon_{\text{Q}} = \sqrt{\frac{1}{N-2}\sum_{i=1}^{N}(Q_i - b - a p_i)^2}, \tag{5.3}$$

where N is the number of points, while a and b are the constants for the best-fitted line. ε_{Q} takes into account both the error on the flow transmitter and any small fluctuations in the temperature during the measurements. Including the error $\varepsilon_{p_{\text{tm}}}$ on the transmembrane pressure, the errors ε_{a} and ε_{b} on the constants a and b can be found as

$$\varepsilon_{\text{a}} = \sqrt{\varepsilon_{\text{Q}}^2 + (a\varepsilon_{p_{\text{tm}}})^2}\sqrt{\frac{N}{\Delta}}, \tag{5.4}$$

$$\varepsilon_{\mathrm{b}} = \sqrt{\varepsilon_{\mathrm{Q}}^2 + (a\varepsilon_{\mathrm{p_{tm}}})^2}\sqrt{\frac{\sum_i p_{\mathrm{tm},i}^2}{\Delta}}, \tag{5.5}$$

where $\Delta = N\sum_i p_{\mathrm{tm},i}^2 - (\sum_i p_{\mathrm{tm},i})^2$.

The viscosity of the water is dependent on the temperature and an error on the measured temperature therefore leads to an error on the viscosity. The temperature transmitter has an error of ±0.5% of the full-scale value, which corresponds to ±1°C. Using table A.8 in [3] to find the variation of the viscosity with the temperature, the error corresponds to an error of approximately $\varepsilon_\eta = 2\%$ on the viscosity. This error influences on the permeability calculated from the experiments.

5.1.2 Challenges

The plugs have a relatively small surface area making them extremely sensitive to impurities in the water. This was a big problem when the experiments were initiated and it took more than two weeks to solve the problems and get the experiments to work properly. A lot of time was invested in solving these problems, both because it was important to get good results without the plugs getting contaminated, but also because solving these problems properly gave valuable experience and insight into which precautions should be made when conducting the experiments and in working with filters in general.

It was quickly discovered, that the plugs became contaminated with particles and impurities from the water. As a layer of particles build up on the plug, the flow rate decreased dramatically. This can be seen in Fig. 5.3(b), where the flow rate measurements have been repeated at the two highest pressure levels, clearly showing a decreasing flow rate. The contamination was both due to impurities in the water itself but mainly due

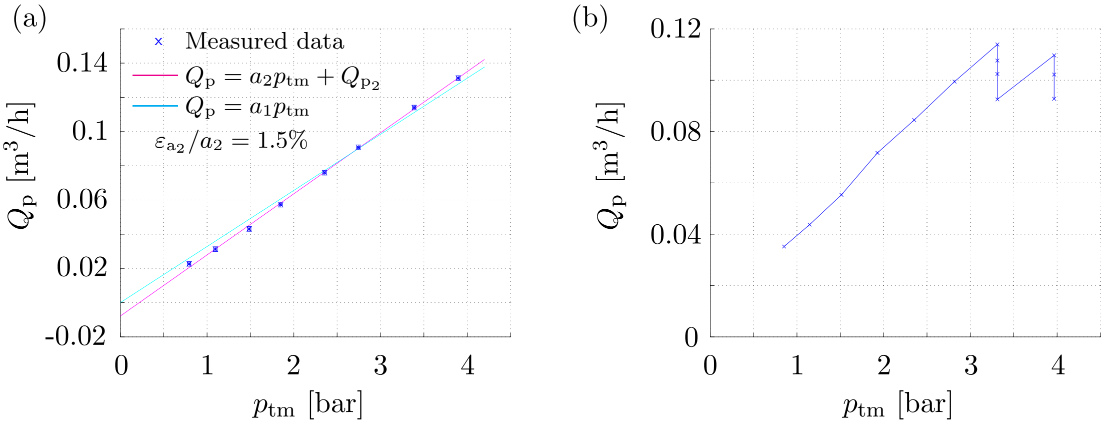

Figure 5.3: Two examples of bad measurements. (a) A measurement where the permeate flow rate Q_{p} does not increase linearly with the transmembrane pressure p_{tm}. This was due to air bubbles at the feed side of the plug. The measured points are shown with their calculated error bars, and it is seen that the error on the measurements is very small. The values for the two linearly fitted lines are: $a_1 = 3.28 \times 10^{-2}\,\mathrm{m^3/(bar\ h)}$, $a_2 = 3.57 \times 10^{-2}\,\mathrm{m^3/(bar\ h)}$, and $Q_{\mathrm{p}_2} = 7.81 \times 10^{-3}\,\mathrm{m^3/h}$. ε_{a_2}/a_2 is the relative error on the slope of the best-fitted line. (b) From the repeated permeate flow measurements at the two highest pressure levels it is clear that the flow decreases, which is due to the plug getting contaminated.

to impurities in the experimental setup. The setup had been used for some kind of oil solution that stuck to the inside of the tubes and pipes. During the experiments this oil solution was carried with the water and stuck to the surface of the plugs. A lot of time was used to clean the setup with everything from normal soap to chlorine and finally a very strong cleaning detergent, Divos 120CL from JohnsonDiversey, which proved successful. Even though the setup was cleaned thoroughly, the plugs were so sensitive, that just a tiny amount of impurities could be seen as a decrease in the flow rate. Therefore the final solution was to use a filter borrowed from CoMeTas to pre-filter the water before the plug.

The low flow rate meant that air could be present in the setup during the measurements. We observed, that if a plug was put in the housing and an experiment started from low pressure, air bubbles could influence the flow rate at the low pressures, so that a lower flow rate than expected was measured. As the pressure was increased, the air bubbles would disappear as they were pressed through the plug, giving a nonlinear relation between Q_p and p_tm. An example of such a measurement is shown in Fig. 5.3(a). Two lines have been fitted to the data points, one is forced through $(0, 0)$ while the other is the best linear fit. These two lines should ideally be the same, but due to the nonlinear relation they are not. The solution to the air problem was to increase the pressure to the maximum pressure of 4 bar to get the air bubbles out of the setup and then lower the pressure again before the measurements were begun.

As mentioned above, normal tap water was used in the plug experiments. When a plug had been used for an experiment and then dried, limescale became a problem in the pores of the plugs making it impossible to repeat a measurement. At first chlorine was used to try and solve this problem but it did not restore the flow rate to the state of the initial measurements. Our solution was citric acid since it dissolves the limescale better, making it easy to get it out of the pores in the plugs.

Bacteria growth in the water also became a problem during the experiments. If the water had been standing in the setup overnight the plugs would get contaminated by bacteria, called biofouling. The biofouling could be seen as a translucent, sticky film lying on the surface of the plugs. As it was not desirable to change the water in the setup every day, we decided to eliminate the bacteria using chlorine in the water. However, it was soon discovered that the chlorine reacted with the pipe weldings in the setup, making rust in the water a problem. The chlorine could react with the weldings because they had not been made from a stainless alloy. We solved this problem using nitric acid in the water instead of chlorine. This had two major effects: The nitric acid lowered the pH value thereby killing the bacteria and it dissolved the rust in the pipes created by the chlorine. Furthermore, it dissolved the limescale just as good as the citric acid. Three problems were thus solved using nitric acid in the water. Throughout all the experiments nitric acid was therefore used in the water to lower the pH value to approximately 3. It is assumed that the use of nitric acid does not change the viscosity significantly since the viscosity of nitric acid is close to that of water and only around 200 mL of nitric acid is used in 70 L of water.

To sum up the encountered problems together with our solutions are listed below:

Particles/impurities in the water and setup: This was solved using a strong cleaning detergent, Divos 120CL from JohnsonDiversey, to clean the setup and then pre-filter the water before the plug with a filter borrowed from CoMeTas.

Air in the setup: We increased the pressure to the maximum pressure used during the plug experiments of 4 bar and then lowered it again before an experiment was begun. This way the air was removed from the setup.

Limescale: Citric acid was used as it dissolved the limescale completely making it possible to remove the limescale from the pores of the plugs. Later we used nitric acid with equally good results.

Biofouling: Bacteria growth in the water resulting in biofouling of the plugs was eliminated by lowering the pH value of the water to approximately 3 using nitric acid.

Rust: Rust in the setup due to chlorine reacting with the weldings was dissolved using nitric acid in the water.

5.1.3 Results

During the experiments with the different plugs the repeatability of the measurements was checked in several ways. The pressure was both increased and decreased to see if any hysteresis effect could be seen, the plugs were taken out of the housing and put in again, they were turned around in the housing, they were left to dry for several days and finally they were left in the setup during a weekend. None of these checks showed any deviations in the measurements. It was also checked several times if the plugs got contaminated. This was done by keeping the pressure level constant for at least an hour and measure the flow rate in the beginning and in the end of this hour.

In Fig. 5.4 a plot is shown of four measurements made with the same plug, P5-1-5.2. The four measurements lie very close together showing good repeatability of the experiments. The error bars on the measured points and the relative error for the best linear fit $\varepsilon_{\mathrm{a}_2}/a_2$ have been calculated as described in Section 5.1.1, and it is clear that the error on the experimental method is insignificant.

In measurement one and three the pressure was increased, while it was decreased in measurement two and four. From this it can be concluded that no hysteresis effect is found. Eight points were made in each of the four measurements giving a total of 32 points in the plot. Three different lines have been fitted to the points; the cyan colored is a linear fit forced through $(0, 0)$, the magenta is the best linear fit and the green is a second order fit. From Darcy's law a linear relationship going through $(0, 0)$ is expected between Q_{p} and p_{tm}. The three fitted lines confirm that this is the case. The two linear fits have the same slope of $a_1 = a_2 = 4.32 \times 10^{-2}\,\mathrm{m}^3/(\mathrm{h\ bar})$ and the intersection with the Q-axis of the best linear fit, $Q_{\mathrm{p}_2} = 1 \times 10^{-4}\,\mathrm{m}^3/\mathrm{h}$, is effectively zero, since the calculated error is $\varepsilon_{\mathrm{Q}_{\mathrm{p}_2}} = 6 \times 10^{-4}\,\mathrm{m}^3/\mathrm{h}$.

The second order fit is suppressed to a linear fit, which can be seen by comparing the second order term, $b_3 = -4.7 \times 10^{-4}\,\mathrm{m}^3/(\mathrm{h\ bar}^2)$, with the linear term, $a_3 = 4.54 \times 10^{-2}\,\mathrm{m}^3/(\mathrm{h\ bar})$. Since p_{tm} is in the order of 1 bar to 4 bar, $b_3 p_{\mathrm{tm}}$ is roughly two orders of magnitude lower than a_3, making it redundant in the expression. Furthermore

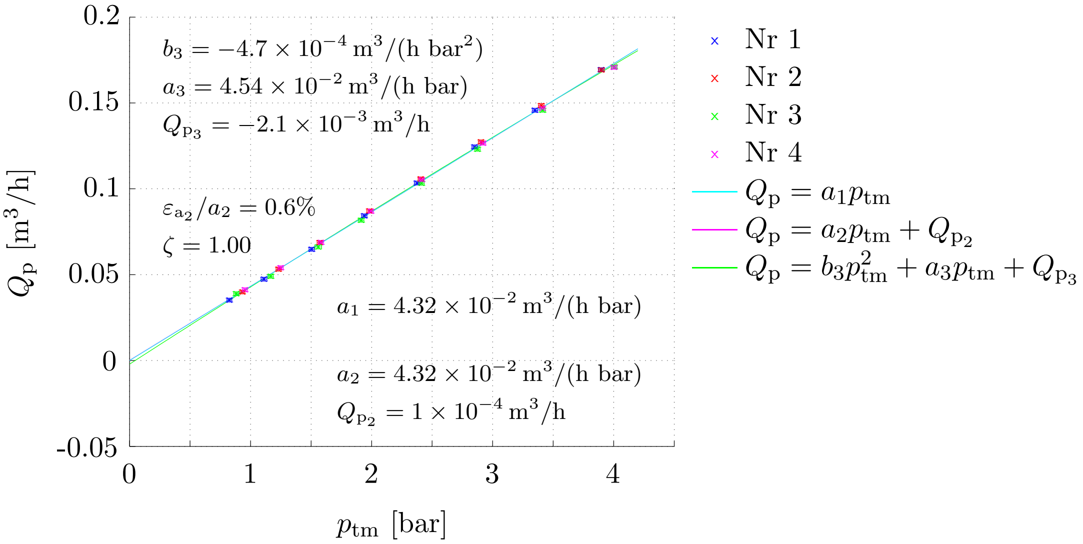

Figure 5.4: A plot of the permeate flow rate Q_p vs. the transmembrane pressure p_tm for plug P5-1-5.2. The measurements have been repeated four times showing good repeatability of the results. The pressure was increased in measurement one and three and decreased in measurement two and four. No hysteresis is found. Furthermore the flow rate through the plug grows linearly with the transmembrane pressure, which can be seen from the fitted lines and the correlation coefficient ζ calculated for the best-fitted line. Thus Darcy's law is confirmed. ε_{a_2}/a_2 is the relative error on the slope of the best-fitted line.

a_3 is almost equal to a_1 and a_2 and the correlation coefficient calculated for the best-fitted line is $\zeta = 1.00$. From these observations we conclude that Darcy's law is confirmed.

In Fig. 5.5 the results for all the plug experiments are shown. Nine plugs were used divided between the four different thicknesses. Unfortunately only one of the plugs from the P3 plate could be used since the others were ruined due to contamination by the oil solution described in Section 5.1.2. Four measurements were done for each of the plugs in order to check the repeatability of the results. Two of the measurements were conducted with increasing pressure, while the other two were conducted with decreasing pressure. Good repeatability as well as no hysteresis was found for all the plugs. Darcy's law was found to be valid for all the plugs.

Fig. 5.5 shows that the flow through P3-2-3.7 is the highest, which is expected, but it is only slightly higher than the flow through P5-1-5.2 even though this plug has a significantly higher thickness. Furthermore there is a big difference between the flow through P5-1-5.2 and P5-2-5.3 even though they have almost the same thickness. In fact P5-2-5.3 only has a slightly higher flow rate than three of the P6 plugs. It is surprising that P6-3-6.6 has the lowest flow rate of all the plugs, lower than the flow through the two P8 plugs. From Fig. 5.5 it can be concluded that there is a significant deviation in the flow rate between plugs from the same plate and there is no clear picture of the flow rate decreasing with increasing plug thickness.

The permeability is calculated from the slope of the best linear fit, a_2. From Eq. (5.1) an expression for the slope of the linear fit is found and by rearranging this expression the

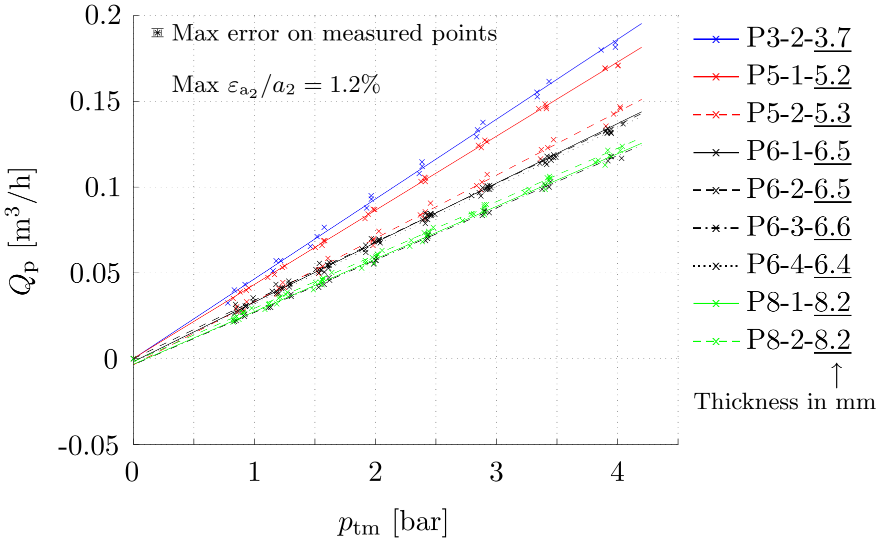

Figure 5.5: Plot of the measurements for all the plugs. The flow through P3-2-3.7 is the highest measured, but only slightly higher than P5-1-5.2. The two P5 plugs deviate a lot from each other. Also P6-3-6.6 is far from the other P6 plugs and has a lower flow than the two P8 plugs. Max ε_{a_2}/a_2 is the maximum relative error on the slopes of the best-fitted lines.

permeability is calculated from

$$k = \frac{4\eta w}{\pi d^2} a_2. \tag{5.6}$$

The error on the permeability ε_{k} is found from the error on the slope ε_{a_2} and the error on the viscosity ε_η,

$$\frac{\varepsilon_{\text{k}}}{k} = \frac{\varepsilon_{\text{a}_2}}{a_2} + \frac{\varepsilon_\eta}{\eta}. \tag{5.7}$$

Any errors on w and d have not been taken into account.

The permeability is found for all the plugs and the results have been plotted in Fig. 5.6 as a function of the plug thickness with the error bars representing ε_{k}. Ideally the points should have lied on a horizontal line in Fig. 5.6, but this is clearly not the case. A spread in the permeability between the plugs was expected because it is well known that the permeability of complicated porous materials vary in small samples, like our plugs. However, the permeability of the P8 plugs is 50% higher than the permeability of P3-2-3.7 and the figure shows a clear tendency of increasing permeability with increasing thickness. This tendency questions the quality of the plugs.

As described in Section 3.1.1 the plugs were fabricated using a press, which means that pressure was used to form the SiC-clay into flat plates. The thinner the plates had to be, the more pressure had to be used. Thus the thin plates were made with the highest pressure and the thick plates with the lowest pressure. It might be a result of the pressure difference we see as low permeability for the thin plugs and high permeability for the thick plugs. This means that the plugs have not been made properly. More experiments could have been carried out to confirm this hypothesis, but since the plug experiments are not

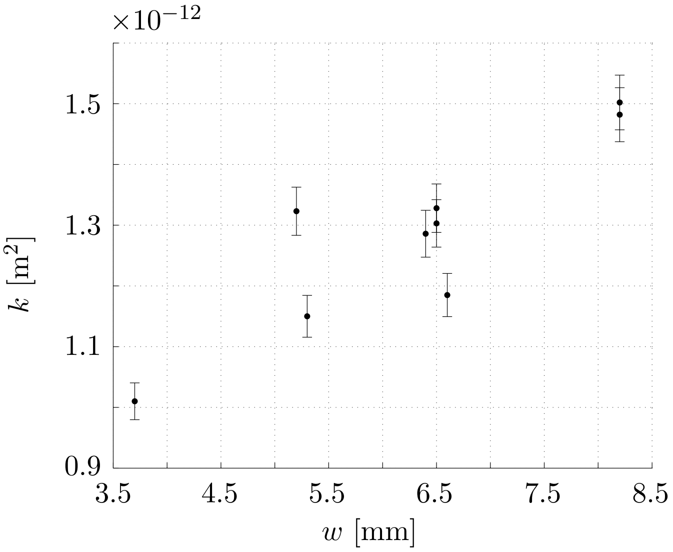

Figure 5.6: Overview of the measured permeability vs. plug thickness. The permeability seems to increase with the thickness. The error bars represent the calculated error ε_k.

essential to this project, it has not been done. A CT-scan of the plugs might also have verified the hypothesis, but unfortunately the CT-scanner had broken down and could not be used during the last four months of the project. A CT-scan of the plugs could therefore not be made. The CT-scan method is described in Section 3.2.1.

Since we suspect that the quality of the plugs is not good enough, the permeability found for the plugs will not be used further in this report.

5.2 Monotubes

Cross-flow measurements were carried out both with some monotubes and with some 24-channel tubes, see Appendix C.1. These measurements showed that the permeate flow rate Q_p was practically independent of the retentate flow rate Q_r for the monotubes but not for the 24-channel tubes, where it was seen that Q_p decreased if Q_r was increased relative to the feed flow rate Q_f. This decrease in Q_p with increasing Q_r was due to a significant channel resistance in the 24-channel tubes. To have the most optimal conditions for our tubes during the experiments, we therefore decided to conduct both the monotube and 24-channel tube experiments in a dead-end flow setup. This also made it easier to control that the same conditions were applied to all the tubes.

As described in Section 4.1.2 the housing had to be mounted horizontally at the retentate exit in order to be able to measure the water temperature using the temperature transmitter positioned at the experimental setup. It was controlled that the same results were achieved with the housing mounted vertically and horizontally in the setup, see Fig. 5.7.

The water was heated as it was recirculated and to keep the temperature constant

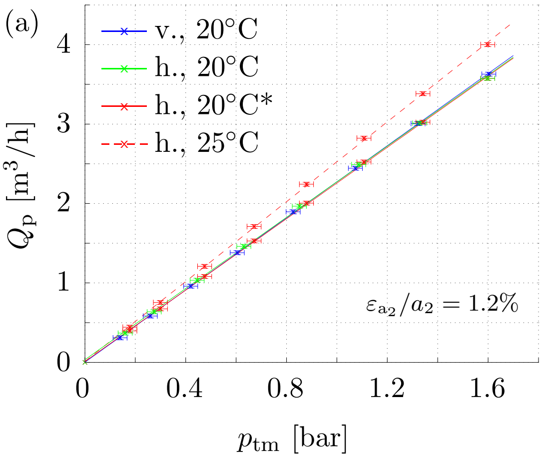

(b)

	a_2 [m^3/(h bar)]	Q_{p_2} [m^3/h]
v., 20°C	2.27	2.0×10^{-3}
h., 20°C	2.24	1.4×10^{-2}
h., 20°C*	2.25	1.1×10^{-2}
h., 25°C	2.51	1.2×10^{-2}

Figure 5.7: (a) Control measurements of the experimental method with TI-XII-III. The housing was positioned both vertically ('v.') and horizontally ('h.') and measurements were conducted at a water temperature of 20°C and 25°C. The flow rate at 25°C was compared to 20°C ('20°C*'), by compensating the difference in the viscosity of the water. No deviations were found. ε_{a_2}/a_2 is the relative error on the slope of the best-fitted lines, and it is representative for all the lines. (b) Table containing the constants for the best-fitted lines on the form $Q_\mathrm{p} = a_2 p_\mathrm{tm} + Q_{\mathrm{p}_2}$.

within ±0.5°C, cold water had to be added to the water reservoir. It was very difficult to keep the water at a temperature of 20°C, and we therefore decided to run the experiments at a water temperature of 25°C. It was checked that changing the temperature did not change the results, see Fig. 5.7. The flow rate measured at 25°C was higher due to the lower viscosity of the water. When compensating the flow rate at 25°C by the change in viscosity from 20°C to 25°C, using table A.8 in [3], the same flow rate as measured at 20°C was achieved.

During all the tube experiments (both monotubes and 24-channel tubes) a water temperature of approximately 25 ± 0.5°C is used. In all the results presented in this thesis the measured flow rate has been compensated to 20°C using the average temperature measured in each of the experiments.

A 2D flow approximation can be used for the water flow in the substrate of the monotubes. Therefore Darcy's law is used on the form given in Eq. (2.41) and repeated here for convenience

$$Q_\mathrm{p} = \frac{2\pi L k}{\eta \ln\left(1 + \frac{2w}{d_\mathrm{c}}\right)} p_\mathrm{tm}, \tag{5.8}$$

where d_c is the channel diameter of the monotube, L is the monotube length, w is the wall thickness and $p_\mathrm{tm} = (p_\mathrm{f} + p_\mathrm{r})/2 - p_\mathrm{p}$ is the transmembrane pressure, see Eq. (2.22), with p_f, p_r and p_p being the feed, retentate and permeate pressures, respectively.

The error on the measured data is calculated in the same way as given in Section 5.1.1 with only one difference. Since p_tm is now found using three measured pressures, the error has changed. All three pressure transmitters have a maximum error of 0.5% of their full-scale value. Using the standard method the error on p_{tm} can then be calculated to be

$$\varepsilon_{\mathrm{p_{tm}}} = \frac{\varepsilon_{\mathrm{p_f}} + \varepsilon_{\mathrm{p_r}}}{2} + \varepsilon_{\mathrm{p_p}} = \frac{0.02\,\mathrm{bar} + 0.02\,\mathrm{bar}}{2} + 0.008\,\mathrm{bar} = 0.028\,\mathrm{bar}. \tag{5.9}$$

From [12] we know that the upper limit of Darcy flow is Re ≈ 2.3 where the Reynolds number is based on the mean grain diameter. We can calculate an approximate value of the maximum permeate flow rate that should be used in the monotube experiments. The velocity v_0 in the porous SiC is found from the Reynolds number as

$$v_0 = \frac{2.3\eta}{\rho d_{\mathrm{m}}} = 0.23\,\mathrm{m/s} \tag{5.10}$$

using a SiC mean grain diameter of $d_{\mathrm{m}} = 10\,\mu\mathrm{m}$ and water with $\rho = 1000\,\mathrm{kg/m^3}$ and $\eta = 10^{-3}\,\mathrm{Pa\ s}$. Hereafter the maximum flow rate Q_{max} is found by integrating v_0 over the channel surface area of the tubes, $Q_{\mathrm{max}} = v_0 \pi L d_{\mathrm{c}}$. With $L = 305\,\mathrm{mm}$ and $d_{\mathrm{c,thin}} = 16.9\,\mathrm{mm}$ and $d_{\mathrm{c,thick}} = 14.1\,\mathrm{mm}$ for the thin and thick-walled monotubes, respectively, the flow rates are

$$Q_{\mathrm{max,thin}} \approx 13.4\,\mathrm{m^3/h}, \tag{5.11}$$

$$Q_{\mathrm{max,thick}} \approx 11.2\,\mathrm{m^3/h}, \tag{5.12}$$

where $Q_{\mathrm{max,thin}}$ and $Q_{\mathrm{max,thick}}$ are the maximum allowed permeate flow rate through a thin-walled and thick-walled monotube, respectively. As $Q_{\mathrm{max,thin}}$ and $Q_{\mathrm{max,thick}}$ are both very high the flow in the SiC should not exceed Darcy flow in our monotube experiments.

5.2.1 Short thin-walled monotubes

The repeatability of the tube experiments was checked in the same way as with the plug experiments and it was also checked frequently if the tubes got contaminated. In Fig. 5.8 four measurements, each with eight measuring points, have been conducted with monotube TI-XII-II. The pressure was increased in measurement one and three and decreased in measurement two and four. No hysteresis was found and the measurements show good repeatability of the experiments. PT01 and PT02, measuring the feed and retentate pressure, respectively, showed an insignificant pressure drop down the length of the monotube in the order of 10^{-2} bar at the highest flow rates, thus the channel resistance in the monotube is negligible.

Three lines have been fitted to the data, a linear fit through $(0,0)$ (cyan line), a best linear fit (magenta) and a power-law fit (green) on the form $Q_{\mathrm{p}} = Q_{\mathrm{p_3}}(p_{\mathrm{tm}}/1\,\mathrm{bar})^{c_3}$. This form is used because when the fit is linear $c_3 = 1$, but if the resistance in the monotube channel becomes significant the Q_{p}-p_{tm} relation becomes nonlinear and $c_3 < 1$. From Section 2.3 it is known that in fully turbulent channel flow the relation is $Q \sim p^{4/7}$, and thus it is expected that $4/7 < c_3 < 1$, if a nonlinear relation is seen.

From the three fitted lines it is clear, that there is a linear relation between Q_{p} and p_{tm} going through $(0,0)$. a_1 and a_2 are identical within the error on a_2 which was calculated to be $\varepsilon_{\mathrm{a_2}} = 3.2 \times 10^{-2}\,\mathrm{m^3/(h\ bar)}$ and $Q_{\mathrm{p_2}}$ is zero within the error of $\varepsilon_{\mathrm{Q_{p_2}}} = 2.6 \times 10^{-2}\,\mathrm{m^3/h}$

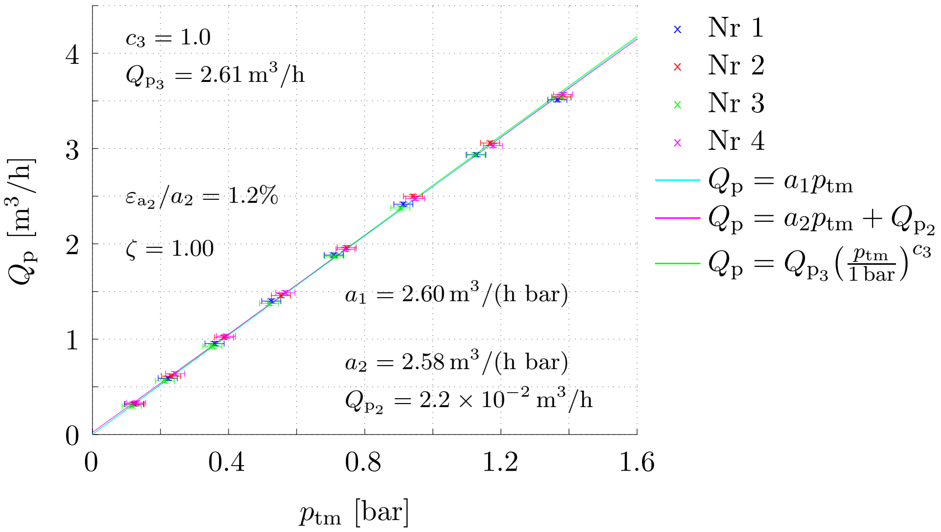

Figure 5.8: A plot of the permeate flow rate Q_p vs. the transmembrane pressure p_{tm} for monotube TI-XII-II. The measurements have been repeated four times showing good repeatability of the results. The pressure was increased in measurement one and three and decreased in measurement two and four. No hysteresis is found. Furthermore, Q_p grows linearly with p_{tm}, which can be seen from the fitted lines and the correlation coefficient ζ for the best-fitted line. Thus Darcy's law is confirmed. ε_{a_2}/a_2 is the relative error on the slope of the best-fitted line.

as well. Furthermore $c_3 = 1.0$ in the power-law fit and the correlation coefficient $\zeta = 1.00$ for the best-fitted line, which also confirms the linear relation.

In Fig. 5.9 all the measured data for the nine thin-walled monotube substrates used in the experiments are shown. The lines are the best-fitted linear lines. Four measurements, each with eight measuring points, were done for each of the nine monotubes, all of them showing good repeatability. Darcy's law was found to be applicable for all the tubes. The average constants including the standard deviation from each of the best-fitted lines are, $a_s = (2.6 \pm 0.2)\mathrm{m^3/(h\ bar)}$ and $Q_{p_s} = (0.05 \pm 0.02)\mathrm{m^3/h}$, where subscript 's' stands for substrate.

A spread of 30% is found on the slope of the best-fitted lines which can be directly transferred to a spread in the permeability of the tubes. As mentioned a spread of this size is not surprising due to a dispersion in the permeability of relatively small samples of porous materials. Furthermore the extrusion pressure in our fabrication method was difficult to control and different extrusion pressures might have led to a dispersion in the permeability. Fabrication of the monotubes is described in Section 3.1.2. As for the plugs the permeability of the monotubes is calculated from the slope of the best linear fit, a_2, where an expression for a_2 is found from Eq. (5.8). By rearranging this expression the permeability is calculated from

$$k = \frac{\eta \ln\left(1 + \frac{2w}{d_c}\right)}{2\pi L} a_2. \tag{5.13}$$

Using Eq. (5.13) the permeability is found for all the monotubes and the mean permeability

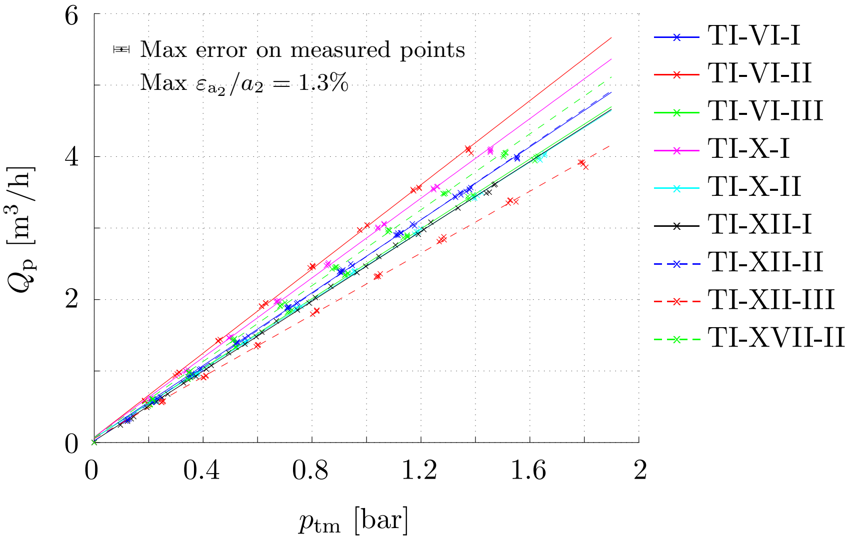

Figure 5.9: Plot of the measurements for all the thin-walled monotubes used. The spread on the slope of the best-fitted lines is 30%. The average slope a_s and average intersection Q_{p_s} with the Q_p-axis plus their standard deviations from the best linear fits are, $a_s = (2.6 \pm 0.2)\text{m}^3/(\text{h bar})$ and $Q_{p_s} = (0.05 \pm 0.02)\text{m}^3/\text{h}$. Max ε_{a_2}/a_2 is the maximum relative error on the slopes of the best-fitted lines.

is then found to be

$$k_{\text{m,thin}} = (8.6 \pm 0.8) \times 10^{-13}\,\text{m}^2, \tag{5.14}$$

where the error is the standard deviation of the permeability from each of the monotubes. The error on the slope on the best-fitted lines from each of the monotubes is not taken into account as it is negligible compared to the spread between the monotubes.

5.2.2 Thick-walled monotubes

The experiments with the thick-walled monotubes showed the same tendencies as the experiments with the thin-walled monotubes. Seven of the thick-walled monotubes were used and the measured data is shown in Fig. 5.10. Again four measurements, each with eight measuring points, were done for each of the monotubes and good repeatability was found. As for the thin-walled monotubes, Darcy's law was found to be valid in these experiments as well. The average constants including the standard deviation from each of the best-fitted lines are, $a_s = (1.29 \pm 0.09)\text{m}^3/(\text{h bar})$ and $Q_{p_s} = (0.06 \pm 0.02)\text{m}^3/\text{h}$.

Fig. 5.10 shows a spread in the flow rate between the monotubes as was also the case with the thin-walled monotubes. The spread on the slope of the best-fitted lines is 20%. The permeability of the tubes is calculated using Eq. (5.13) and the mean value is

$$k_{\text{m,thick}} = (7.9 \pm 0.5) \times 10^{-13}\,\text{m}^2, \tag{5.15}$$

where the error is the standard deviation of the permeability from each of the monotubes. This permeability is a bit lower than the mean permeability found for the thin-walled tubes, see Eq. (5.14). Taking the error on the permeability into account, the permeabilities

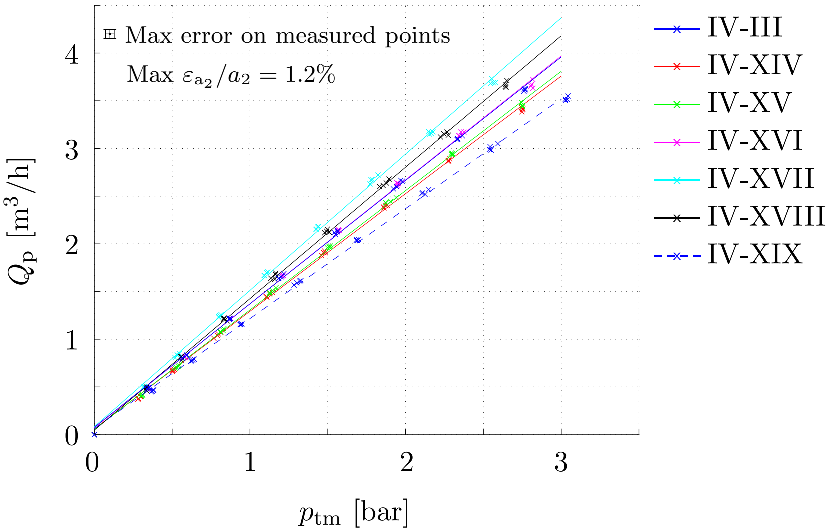

Figure 5.10: Plot of the measurements for all the thick-walled monotubes used in the substrate experiments. The spread of the slope of the best-fitted lines is 20%. The average slope a_s and average intersection Q_{p_s} with the Q_p-axis plus their standard deviations from the best linear fits are, $a_s = (1.29 \pm 0.09)\text{m}^3/(\text{h bar})$ and $Q_{p_s} = (0.06 \pm 0.02)\text{m}^3/\text{h}$. Max ε_{a_2}/a_2 is the maximum relative error on the slopes of the best-fitted lines.

found for the thin-walled and thick-walled monotubes are almost identical. From this observation we conclude that the permeability is independent of the wall thickness. The overall permeability of the SiC used in the work for this thesis can be found using the results from the nine thin-walled and the seven thick-walled monotubes to be

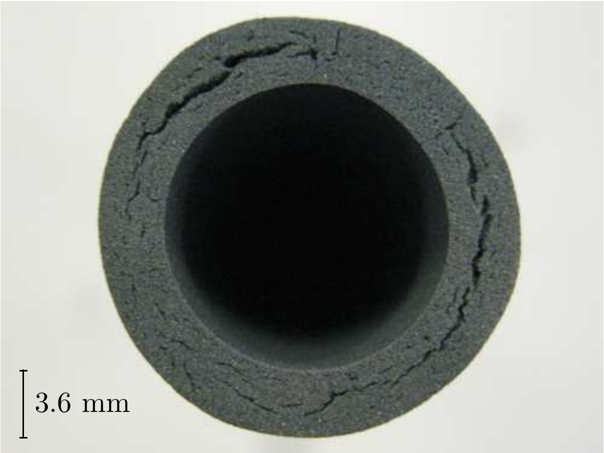

Figure 5.11: Cross-section of the thick-walled monotube IV-III that cracked during the drying and subsequent sintering process. Since the crack did not go from the channel to the surface no difference in the permeate flow rate was seen, compared to the high-quality monotubes.

$$k_{\mathrm{m}} = (8.3 \pm 0.7) \times 10^{-13}\,\mathrm{m}^2. \tag{5.16}$$

An experiment was carried out with a monotube (IV-III) that had cracked during the drying and subsequent sintering process, see Fig. 5.11. The crack did not go from the channel to the surface of the monotube, only lengthwise. Therefore there should be no difference in the permeate flow rate through the monotube compared to the high-quality tubes as the resistance in the porous SiC has just been split in two serial connected resistances. In Fig. 5.10 the flow rate measured for IV-III is placed in the middle of the other monotubes and it can be concluded that no difference compared to the high-quality monotubes is seen.

5.2.3 Long thin-walled monotubes

The flow experiments conducted with the 1 m long thin-walled monotubes are shown in Appendix C.2. It was difficult to measure the permeate pressure at the long housing since PT03 could not be positioned at the housing and therefore the measured pressure has a significant error. Furthermore a nonlinear relation is seen between Q_{p} and p_{tm}, due to a large hydraulic channel resistance. The results from these experiments are consequently not used when determining the permeability of the SiC-substrate.

5.2.4 Re-sintered monotubes

As described in Section 3.1 the coated tubes had to be sintered again twice because of the two membrane layers. To check if this re-sintering process changed the permeability of the substrate, two uncoated, short, thin-walled monotubes were also re-sintered. The

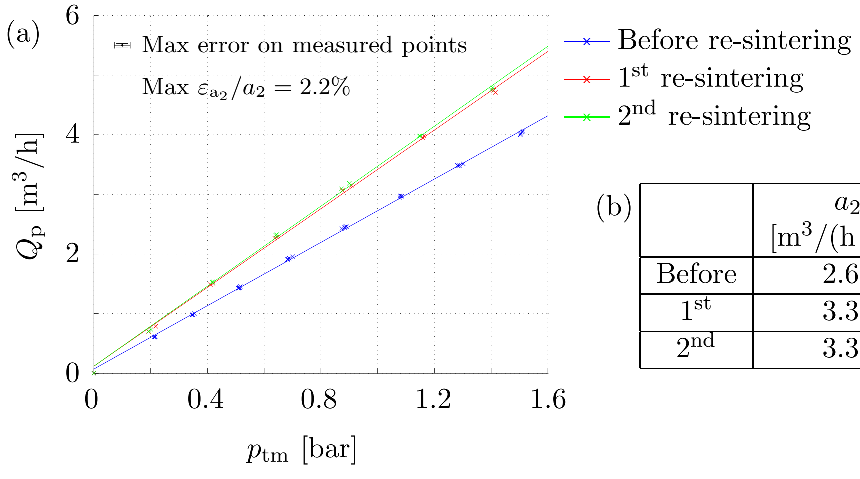

(b)

	a_2 [m^3/(h bar)]	Q_{p_2} [m^3/h]
Before	2.65	4.1×10^{-2}
1st	3.30	6.3×10^{-2}
2nd	3.34	6.6×10^{-2}

Figure 5.12: (a) The uncoated monotube TI-XVII-II was re-sintered twice with the coated monotubes when the membranes were sintered. The flow rate has increased by 25% due to so-called grain growth. As the flow rate is the same after the first and second re-sintering it can be concluded that grain growth has only happened during the first re-sintering process. Max ε_{a_2}/a_2 is the maximum relative error on the slopes of the best-fitted lines. (b) Table containing the constants for the best-fitted lines on the form $Q_{\mathrm{p}} = a_2 p_{\mathrm{tm}} + Q_{\mathrm{p}_2}$.

measurements conducted with TI-XVII-II are shown in Fig. 5.12. The figure shows a significant increase of 25% in the flow rate after the first re-sintering, while there is no change from the first to the second re-sintering. The same was seen for the other re-sintered monotube, TI-VI-III.

This increase in the flow rate is due to a so-called grain growth in the SiC, which means that the SiC-grains in the substrate increase their size, [22]. During the re-sintering the internal energy can only be reduced by decreasing the grain boundary area, thus small grains are consumed by larger grains and sharp edges become more round. Such a grain growth results in larger pores in the SiC-substrate and therefore a higher permeability. Since there is no change in the flow rate from the first to the second re-sintering it can be seen that the grain growth only occurs during the first re-sintering process.

Only two monotubes were re-sintered and therefore we cannot conclude that the permeability changes in the substrate during the re-sintering, but only state that there is a clear tendency that this is the case. In order to give a more significant conclusion, more monotubes should have been re-sintered.

5.3 24-channel tubes

The experiments with the 24-channel tubes were conducted in a dead-end flow setup in the same way as the monotube experiments. The 24-channel tubes are not used in order to find the permeability of the SiC-material, but in order to introduce a more complex geometry in the thesis which is used by CoMeTas in some of their membranes.

In Fig. 5.13 four measurements carried out for XXIV-V are shown. As with the mono-

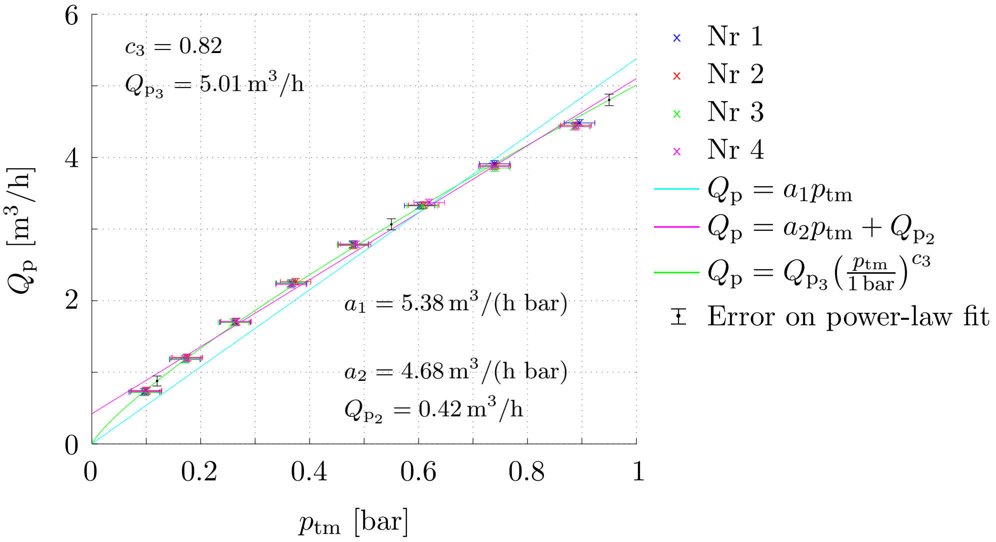

Figure 5.13: A plot of the permeate flow rate Q_p vs. the transmembrane pressure p_{tm} for 24-channel tube XXIV-V. The flow rate is not linearly related to the transmembrane pressure because the channel resistance in the tube becomes significant.

tubes excellent repeatability is found in the experiments, but there is no longer a linear relation between Q_p and p_tm. The power in the power-law fit is $c_3 = 0.82$ clearly indicating a nonlinear profile, and also the two linear fits are no longer identical.

The nonlinear profile is due to a significant hydraulic resistance R_hyd in the channels of the 24-channel tube. The channels have a width of 3 mm, which is approximately five times smaller than the diameter of the channel in the monotubes. Assuming laminar flow, the hydraulic resistance in the quadrilateral channels of the 24-channel tubes can be found from [1] as

$$R_\mathrm{hyd,24} = 28.4\eta L \frac{1}{h^4} = 1.1 \times 10^8 \,(\mathrm{Pa\ s})/\mathrm{m}^3, \tag{5.17}$$

with $\eta = 10^{-3}\,\mathrm{Pa\ s}$, $L = 305\,\mathrm{mm}$ and $h = 3\,\mathrm{mm}$. The hydraulic resistance in the monotubes can be found from Eq. (2.28),

$$R_\mathrm{hyd,mono} = \frac{128\eta L}{D^4\pi} = 2.5 \times 10^5 \,(\mathrm{Pa\ s})/\mathrm{m}^3, \tag{5.18}$$

with $D = 15\,\mathrm{mm}$. Hence, the hydraulic resistance has increased by approximately a factor of 400, and it is thus not surprising that it is no longer negligible.

p_tm is found as $p_\mathrm{tm} = (p_\mathrm{f} + p_\mathrm{r})/2 - p_\mathrm{p}$ under the assumption of laminar channel flow and a constant pressure drop in the channels, as described in Section 2.2.4. This assumption holds well even in turbulent flow, if the pressure drop in the channels is negligible as it is in the monotubes. In the 24-channel tubes a pressure drop of $p_\mathrm{f} - p_\mathrm{r} \approx 0.25\,\mathrm{bar}$ is measured down the length of the tubes at a flow rate of $Q_\mathrm{p} \approx 4.5\,\mathrm{m}^3/\mathrm{h}$ and the pressure drop is therefore no longer negligible.

In pipe flow the flow is laminar until Re $\approx$ 2300 and by assuming the same average velocity in the channels, an estimate of the maximum flow rate with laminar flow in the channels can be made. The average velocity is

$$v_\mathrm{max,lam} = \frac{2300\eta}{\rho h} = 0.77\,\mathrm{m/s}, \tag{5.19}$$

with $\rho = 1000\,\mathrm{kg/m}^3$, $\eta = 10^{-3}\,\mathrm{Pa\ s}$ and $h = 3\,\mathrm{mm}$ being the channel width. An estimate of the flow rate is found by assuming 24 channels with the same cross-sectional area of $\mathcal{A}_\mathrm{c} = (3\,\mathrm{mm})^2$

$$Q_\mathrm{max,lam} = 24\mathcal{A}_\mathrm{c} v_\mathrm{max,lam} \approx 0.6\,\mathrm{m}^3/\mathrm{h}. \tag{5.20}$$

As seen in Fig. 5.13 all the measurements are done at higher flow rates and therefore the flow is not laminar in the channels. This means that the assumptions used to find p_tm are wrong. The non-linear relation between flow rate and p_tm is due to the poor estimate of p_tm and Darcy's law is still valid in the porous SiC of the 24-channel tubes.

Fig. 5.13 shows that the measured data agrees well with the power-law fit at the low flow rates, while at the higher flow rates there is a tendency that the points lie below the fit. This is both because the flow changes from laminar to turbulent in the channels, but also because the boundary conditions at the inlet of the 24-channel tube will become more and more influential as the flow rate increases which might contribute to the nonlinear behavior. However, overall the power-law fit agrees well with the measured data.

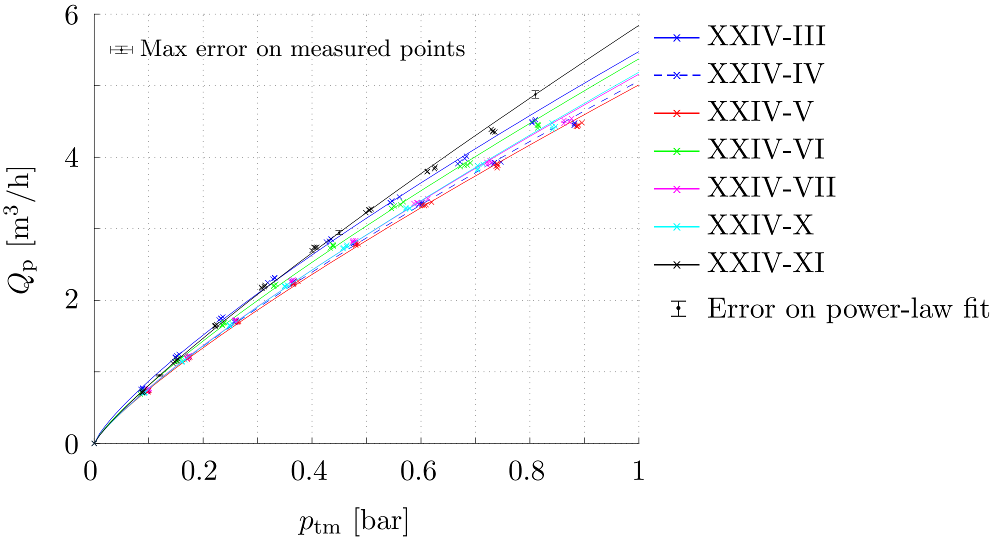

Figure 5.14: Plot of the measurements for all the 24-channel tubes used in the substrate experiments. The error of the fitted lines is shown in three places on the slope of XXIV-XI. The error bars in this figure are representative for all the measurements for the 24-channel tubes. The spread in the flow rate is approximately 20%. The mean constants including their standard deviations found from the power-law fits are, $c_\mathrm{s} = 0.82 \pm 0.02$ and $Q_{\mathrm{p_s}} = (5.3 \pm 0.3)\mathrm{m^3/h}$.

The error on the measured data is found in the same way as for the monotubes with only a few differences. Since the flow rate is no longer linearly related to the transmembrane pressure, the error on the measured flow rate is found relative to the power-law fit instead of the best linear fit. Also, the error is no longer calculated for the best-fitted linear line but instead for the power-law fit. This is done by fitting two lines to the measured points with their error added and subtracted, respectively, and using these two lines as a measure of the error on the power-law fit.

Fig. 5.14 shows all the data for the seven 24-channel tubes used in the substrate experiments. Just like for the monotubes a spread is seen in the flow rate between the tubes, which is approximately 20%. The 24-channel tubes were fabricated by LiqTech in controlled conditions, as described in Section 3.1.3, and since the tubes have a dispersion in the flow rate (and thus also in the permeability) of the same size as found for the monotubes, it confirms that we have fabricated monotubes of high quality.

All the 24-channel tubes have a nonlinear Q_p-p_tm relation and follows the power-law fit very well. It is consistent for all the tubes that the highest measured flow rates lie slightly below the fitted lines which is most likely due to the reasons described above.

5.4 Summary

Experiments with the plugs and monotubes confirm Darcy's linear law for flow in porous materials. Furthermore, all experiments show good repeatability of the results and the error on the experimental method is low.

Table 5.1: The measured permeabilities k, in m^2, from the experiments with the thin-walled and the thick-walled monotubes plus the overall permeability from both experiments. It is concluded that the permeability is independent of the thickness. The errors are the standard deviations of the permeability found from each of the used monotubes.

	k [m^2]
Thin-walled	$(8.6 \pm 0.8) \times 10^{-13}$
Thick-walled	$(7.9 \pm 0.5) \times 10^{-13}$
Overall	$(8.3 \pm 0.7) \times 10^{-13}$

In the plug experiments nine plugs divided between four different thicknesses are used and the results show a clear tendency of increasing permeability with increasing thickness. Due to this tendency it is concluded that the plugs have not been fabricated properly and the permeabilities calculated from these experiments are therefore rejected.

During plug experiments several problems concerning the experimental method are solved and much experience is achieved with the experimental setup and method which proved valuable when tube experiments were carried out.

Monotube experiments show good agreement for the permeability found from the nine thin-walled and seven thick-walled monotubes and we conclude that the permeability is independent of the wall thickness. The permeabilities are given in Table 5.1. A dispersion of up to 30% is measured in flow rate between the tubes and this tendency is seen for both monotubes and 24-channel tubes. It is expected that this dispersion is due to a variation in the permeability in between the tubes since the tubes are relatively small SiC-samples.

Experiments with 24-channel tubes show that the Q_p-p_tm relation no longer is linear. This nonlinearity is because of the hydraulic resistance in the channels of the tube being significant leading to a high pressure drop down the length of the 24-channel tubes. As the channel flow is not laminar the pressure drop is nonlinear in the channels. The estimate of the transmembrane pressure is therefore poor, which is the reason for the nonlinear relation between Q_p and p_tm. Darcy's law is still valid in the porous SiC of the 24-channel tubes.

Chapter 6

Experiments with coated SiC-tubes

An essential part of the filters used by CoMeTas is the membrane layer added to the surface of the channels. We therefore coated some of our thin-walled monotubes and some of our 24-channel tubes with two membrane layers as described in Section 3.1.4. All the tubes were coated with the same middle layer using a 1 µm membrane, while two different types of membrane were used for the outer layer, a 0.1 µm membrane and a 0.04 µm membrane. These membranes were chosen because CoMeTas uses them in their filters. Since the 0.04 µm membrane is the one most often used by CoMeTas, most of the tubes were coated with this membrane.

In the following we describe the experiments conducted with the coated monotubes and 24-channel tubes. We first present our experiments with the monotubes, which are used to find an estimate of the permeability in the two outer membrane layers. This membrane permeability can later be used in our simulations. Second we present our experiments with the 24-channel tubes, which will be used to verify our numerical models, just like the 24-channel tube substrate experiments.

In Chapter 5 we found that the error on the experimental method was very low. In order to save time we have therefore only conducted two measurements, instead of four, with each of the coated tubes in this chapter.

We have investigated the thickness of the membrane layers and the quality of the coating method by taking pictures of the membranes using a microscope. These pictures are also presented here.

6.1 Thin-walled monotubes

Some initial experiments were conducted with four monotubes after they had been coated with the 1 µm membrane. These experiments were carried out in order to see how this membrane affected the permeate flow rate through the tubes and they are presented in Appendix C.3.1. As expected the flow rate was still linearly related to the transmembrane pressure and a minor decrease in the flow rate of approximately 15% was found when comparing to the average flow rate from the substrate experiments.

6.1.1 0.1 µm membrane

Four thin-walled monotubes were coated with the so-called 0.1 µm membrane. The experiments are carried out in the same way as described in Chapter 5 and the results are shown in Fig. 6.1. A linear relation between the flow rate and the transmembrane pressure is still seen and by comparing with the results from the substrates shown in Fig. 5.9, it is seen that the flow rate has decreased by almost 70% in average. This is a significant decrease, and it can be concluded that the 0.1 µm membrane has a much lower permeability than the substrate.

The permeability in the membrane is estimated using the law of serial connected resistors, since the resistance R_{01} in the membrane has been added just before the resistance R_s in the substrate. In this estimate it is assumed that there is only one membrane layer and the 1 µm membrane layer is neglected. From Eq. (2.32) it is seen that $R = 1/a_2$, where a_2 is the slope from the best linear fit in the experiments. Using Eq. (2.34) we get

$$R_{\mathrm{s},01} = R_\mathrm{s} + R_{01} \quad \Rightarrow \quad a_{01} = \left(\frac{1}{a_{\mathrm{s},01}} - \frac{1}{a_\mathrm{s}}\right)^{-1} = \frac{a_\mathrm{s}\, a_{\mathrm{s},01}}{a_\mathrm{s} - a_{\mathrm{s},01}}, \tag{6.1}$$

where subscript 's' stands for substrate, 's,01' is substrate plus the 0.1 µm membrane, and '01' is only the 0.1 µm membrane. The slopes a_s and $a_{\mathrm{s},01}$ are the average slopes found in the respective experiments, while a_{01} is the fictive slope if we had measured only on the 0.1 µm membrane itself. Assuming a membrane thickness of $w_{01} = 0.1\,\mathrm{mm}$ we can

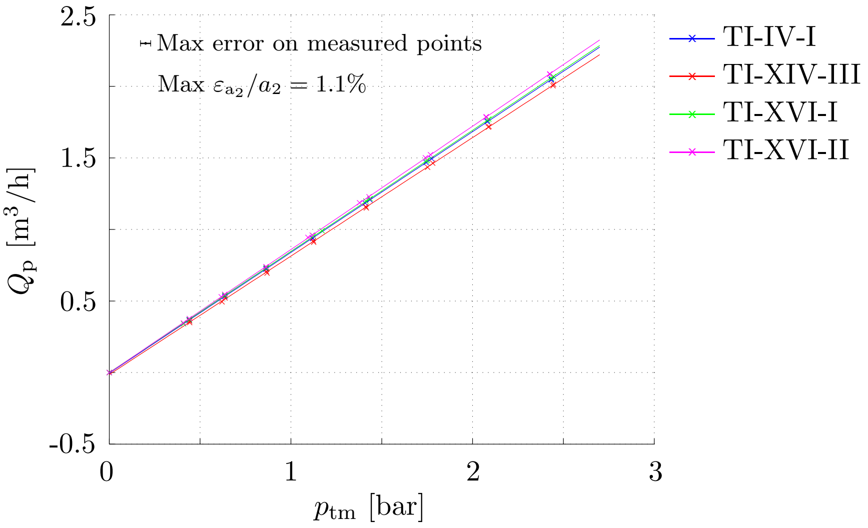

Figure 6.1: Plot of the measurements for four thin-walled monotubes coated with the 0.1 µm membrane. The flow rate has decreased approximately 70% compared to the substrate measurements. The spread on the measured flow rate is only 5%. Max ε_{a_2}/a_2 is the maximum relative error on the slopes of the best-fitted lines. The average slope $a_{\mathrm{s},01}$ and average intersection $Q_{\mathrm{p}_{\mathrm{s},01}}$ with the Q_p-axis plus their standard deviations from the best linear fits are, $a_{\mathrm{s},01} = (0.85 \pm 0.01)\mathrm{m}^3/(\mathrm{h\ bar})$ and $Q_{\mathrm{p}_{\mathrm{s},01}} = (-6 \pm 6) \times 10^{-3}\,\mathrm{m}^3/\mathrm{h}$.

use a 1D approximation of Darcy flow in the membrane as we did for the plugs and the permeability k_{01} can be calculated by changing Eq. (5.6) slightly,

$$k_{01} = \frac{w_{01}\eta}{d_c \pi L} a_{01} = 2.2 \times 10^{-14}\,\mathrm{m}^2, \tag{6.2}$$

with $\eta = 10^{-3}\,\mathrm{Pa\ s}$, $L = 305\,\mathrm{mm}$ and $d_c = 16.9\,\mathrm{mm}$. The channel diameter of the thin-walled monotubes is assumed unchanged. The estimate shows that the permeability in the membrane is significantly lower than in the substrate being almost two orders of magnitude lower. The permeability estimated here should not be seen as an attempt of finding the correct permeability of the 0.1 µm membrane, since the 1 µm membrane is not taken into account and the correct thickness of the membrane is unknown. It is merely an estimated value that can be used in our simulations of the flow rate through the tubes coated with the 0.1 µm membrane.

As Fig. 6.1 shows, the monotubes lie very close together and the spread in the flow rate is only 5%, six times smaller than the spread for the substrates. Even though only four monotubes have been coated with the 0.1 µm membrane, this is a clear tendency of a smaller spread for the coated monotubes which indicates that the monotubes have been uniformly coated. This was also seen for the experiments with the 1 µm membrane, see Appendix C.3.1.

A new contamination problem was encountered in the experiments with the coated tubes. We observed that if the tubes had been left to dry or even left in the housing on the experimental setup for a couple of days, the flow rate had decreased significantly. This problem could not be solved using nitric acid and had not been encountered with the substrates. It is suspected that the contamination was due to biofouling in the membrane layer and some of the bacteria could be flushed out at high pressures. In order to restore the initial flow rate, however, we had to heat the tubes to a temperature of 600°C. This problem was encountered for all the coated tubes, both monotubes and 24-channel tubes.

6.1.2 0.04 µm membrane

Ten thin-walled monotubes were coated with the 0.04 µm membrane. The results from the conducted experiments are shown in Fig. 6.2 and it is seen that three monotubes differ significantly from the others having a much higher flow rate. The spread is more than 100% and it is suspected that the three monotubes lying in the top have been poorly coated. To check this we carried out bubble point experiments with all the monotubes. The bubble point method is described in Appendix A.3. These experiments showed that the seven monotubes with the low flow rate had approximately the same bubble point pressure, while the three tubes with the high flow rate had a significantly lower bubble point pressure. Based on these experiments we therefore conclude that the three monotubes had been poorly coated and they are omitted from the results for the 0.04 µm membrane. It is not known why the three monotubes have been poorly coated, but all three had been used for the 1 µm membrane experiments, see Appendix C.3.1, and thus there seem to be a connection between the two.

The spread between the seven remaining monotubes is approximately 20% which is in the same order as the spread found for the substrates but four times higher than the

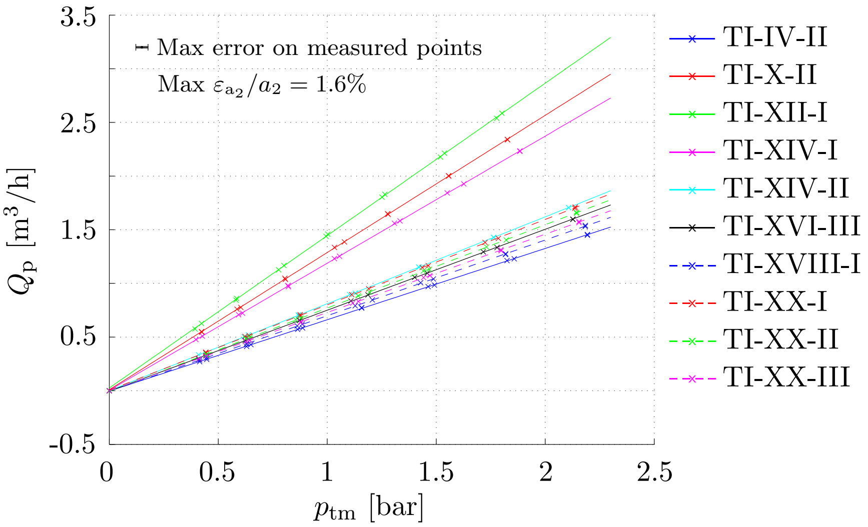

Figure 6.2: Plot of the measurements for the ten thin-walled monotubes coated with the 0.04 µm membrane. Big variations of more than 100% are seen in the flow rate. Seven monotubes lie reasonably close in the bottom, while the three last monotubes differ significantly having a much higher flow rate due to poor coating. The flow rate has decreased more than 70% for the monotubes in the bottom compared to the substrate measurements. Max ε_{a_2}/a_2 is the maximum relative error on the slopes of the best-fitted lines. The mean slope $a_{s,004}$ and mean intersection with the Q_p-axis $Q_{p_{s,004}}$ plus their standard deviations from the best linear fits of the seven monotubes in the bottom are, $a_{s,004} = (0.75 \pm 0.05)\mathrm{m}^3/(\mathrm{h\ bar})$ and $Q_{p_{s,004}} = (-2 \pm 4) \times 10^{-3}\,\mathrm{m}^3/\mathrm{h}$.

spread found for the monotubes coated with the 0.1 µm membrane. This indicates that the monotubes with the 0.04 µm membrane have not been as uniformly coated as the monotubes with the 0.1 µm membrane. The reason for this is unknown.

The flow rate has decreased slightly more than 70% in average compared to the substrate experiments and it is practically the same as measured for the tubes coated with the 0.1 µm membrane. Since the average pore size in the 0.04 µm membrane should be approximately 2.5 times smaller than in the 0.1 µm membrane, it was expected that the flow rate in the tubes with the 0.04 µm membrane was significantly lower, assuming the same membrane thickness. As the flow rates are approximately the same, it indicates that the 0.1 µm membrane is thicker than the 0.04 µm membrane.

An estimate of the permeability k_{004} in the 0.04 µm membrane is found using the same assumptions as for the 0.1 µm membrane. The fictive slope a_{004} is found from Eq. (6.1) with $a_{s,01}$ replaced by $a_{s,004}$ and the permeability is then found from Eq. (6.2) with a membrane thickness of $w_{004} = 0.1\,\mathrm{mm}$,

$$k_{004} = 1.8 \times 10^{-14}\,\mathrm{m}^2. \tag{6.3}$$

6.1.3 Investigation of the membrane thickness

This section has been abridged, and only the most important tendencies seen are described. Since we had some discrepancies in the experiments with our coated monotubes, we decided to check the thickness of the membrane layers using an optical Zeiss microscope. This microscope had an error of ±2 µm and all the pictures were taken with a magnification of five. Six monotubes were chosen, two were coated with the 0.1 µm membrane (TI-XIV-III and TI-XVI-II), and four were coated with the 0.04 µm membrane, two of these having a high flow rate (TI-X-II and TI-XII-I), and two having a low flow rate (TI-IV-II and TI-XX-I). We cut three cross-sectional slices from each tube, two slices 2 cm from each end and one in the middle.

The pictures shown in Fig. 6.3 give an impression of the tendencies seen for the membrane layers. Fig. 6.3(a) is a picture of a pure substrate, which can be used as a reference picture. In Fig. 6.3(b) the mid section of TI-XVI-II coated with the 0.1 µm membrane is shown. The 0.1 µm and 1 µm membrane layers are both easily visible and no irregularities are seen. This tendency was seen in all three slices from the two monotubes coated with the 0.1 µm membrane, which confirms that they have been uniformly coated. The thicknesses

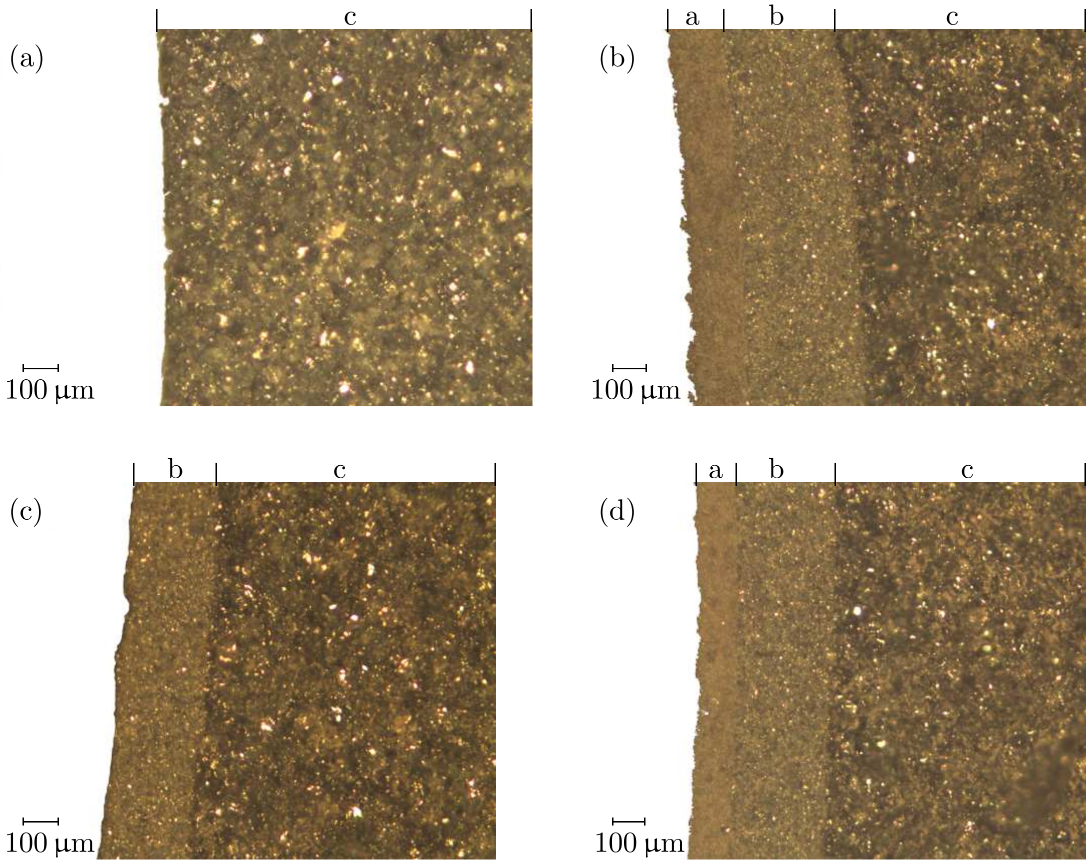

Figure 6.3: Pictures of the membrane thicknesses on the thin-walled monotubes. 'a' refers to the outer membrane layer, 'b' is the middle layer, while 'c' is the substrate. (a) Reference picture of a pure substrate. (b) Mid section of TI-XVI-II coated with the 0.1 µm membrane. The outer and middle layers are easily seen. (c) Mid section of TI-XII-I coated with the 0.04 µm membrane. However, only the middle layer is visible. (d) Mid section of TI-IV-II coated with the 0.04 µm membrane. Both membrane layers are visible.

of the membrane layers was measured to be $w_1 = (300 \pm 15)\mu\text{m}$ and $w_{01} = (180 \pm 20)\mu\text{m}$, where subscript '1' and '01' refers to the 1 µm and 0.1 µm membrane layers, respectively.

The mid section of TI-XII-I coated with the 0.04 µm membrane is shown in Fig. 6.3(c). Only the middle layer is visible which explains why this monotube had a surprisingly high flow rate. This was also seen in the slices from the other monotube having a high flow rate. A very thin layer of the 0.04 µm membrane having a thickness of no more than 5-10 µm was seen in some places on the two monotubes. The reason why the 0.04 µm membrane has almost disappeared is unknown, but as mentioned it is suspected to be caused by biofouling of the 1 µm membrane, since the two monotubes had been used for the 1 µm membrane experiments before being coated with the 0.04 µm membrane. Since the pictures show that the 0.04 µm membrane layer is missing, we conclude that the monotubes having a high flow rate have been poorly coated, and their results are therefore rejected.

Fig. 6.3(d) shows the mid section of TI-IV-II coated with the 0.04 µm membrane. Like in Fig. 6.3(b) showing the monotube coated with the 0.1 µm membrane, both membrane layers are visible and no irregularities are seen. The thicknesses of the membrane layers was measured to be $w_1 = (290 \pm 15)\mu\text{m}$ and $w_{004} = (120 \pm 20)\mu\text{m}$, where subscript '1' and '004' refers to the 1 µm and 0.04 µm membrane layers, respectively. The thickness of the middle layer is approximately the same as measured for the other monotubes, while the 0.04 µm membrane is 30% thinner than the 0.1 µm membrane. This explains why the monotubes coated with the two membranes had approximately the same flow rate.

6.1.4 Comparison of substrate and membranes

The experiments conducted with the thin-walled monotubes are compared in Fig. 6.4. The average best-fitted lines are presented from each of the experiments clearly showing that the flow rate decreases when the monotubes are coated. The flow rate decreases approximately 15% from the substrates to the tubes coated with the 1 µm membrane while it decreases approximately 70% when the monotubes were coated with the 0.1 µm and 0.04 µm membrane. It was expected that the flow rate would be much lower through the monotubes coated with the 0.04 µm membrane compared the ones coated with the 0.1 µm membrane due to the lower permeability, but as Fig. 6.4 shows the difference was only about 10%. Taking the dispersion of the measurements into consideration, they are thus practically equal. From the microscope pictures we found the reason was that the 0.04 µm membrane layer was approximately 30% thinner than the 0.1 µm membrane layer.

The error bars on the average best-fitted lines represent the standard deviation of the slopes from each monotube used in the four experiments. From the error bars it is seen that the dispersion of the measurements decreases significantly from the substrates to the coated monotubes, indicating that the monotubes have been uniformly coated without big deviations. This was confirmed by the microscope pictures from which it was seen that the membrane layers had approximately the same thickness on the monotubes investigated.

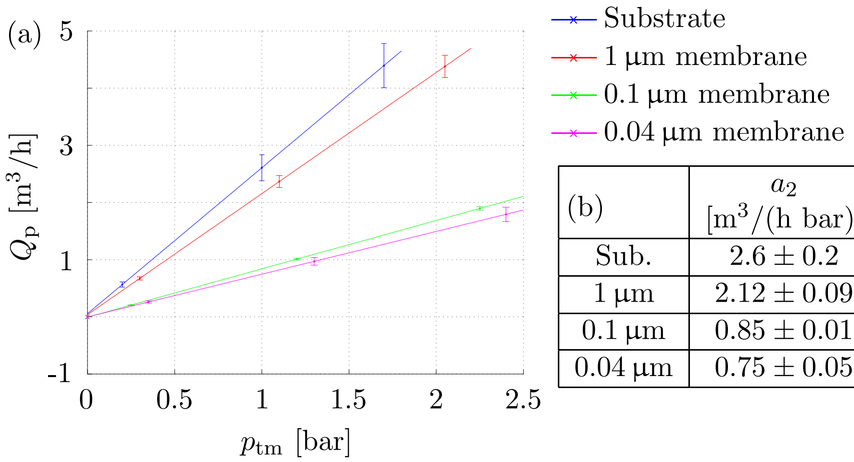

(b)	a_2 [m^3/(h bar)]	Q_{p_2} [m^3/h]
Sub.	2.6 ± 0.2	$(5 \pm 2) \times 10^{-2}$
1 µm	2.12 ± 0.09	$(3 \pm 1) \times 10^{-2}$
0.1 µm	0.85 ± 0.01	$(-6 \pm 6) \times 10^{-3}$
0.04 µm	0.75 ± 0.05	$(-2 \pm 4) \times 10^{-3}$

Figure 6.4: Comparison of thin-walled monotubes. (a) The mean best-fitted lines from the different experiments are plotted and the error bars represent the standard deviation of the slopes from the best fits. (b) Table containing the average constants including their standard deviations for the best-fitted lines on the form $Q_\mathrm{p} = a_2 p_\mathrm{tm} + Q_{\mathrm{p}_2}$. The flow rate is almost equal for the 0.1 µm and the 0.04 µm membrane due to a higher thickness of the 0.1 µm membrane. The error decreases significantly from the substrate to the membrane experiments, indicating that the monotubes have been uniformly coated.

6.2 24-channel tubes

As for the monotubes, initial experiments were conducted with four 24-channel tubes coated with the 1 µm membrane, see Appendix C.3.2. The experiments showed a decrease of 20% in average in the flow rate compared to the substrate experiments at $p_\mathrm{tm} = 1$ bar, which is in the same magnitude as seen for the monotubes. Further, the experiments showed a spread of 25% in the flow rate between the tubes which is more than seen for the monotubes. This might indicate that the 24-channel tubes have not been uniformly coated with the 1 µm membrane.

6.2.1 0.1 µm membrane

Four 24-channel tubes were coated with the 0.1 µm membrane and the results from the experiments are shown in Fig. 6.5. By comparing with the results from the substrate experiments shown in Fig. 5.14, it is seen that the flow rate has decreased by approximately 60% at a pressure of $p_\mathrm{tm} = 1$ bar. This is a bit less than the decrease seen for the monotubes coated with the 0.1 µm membrane, which is partly because the Q_p-p_tm relation has become more linear for the coated 24-channel tubes due to the lower flow rate. The mean power for the tubes coated with the 0.1 µm membrane is $c_{\mathrm{s},01} = 0.93$, while it was $c_\mathrm{s} = 0.83$ for the substrates clearly showing the more linear relation.

The spread in the flow rate is 12%, which is much lower than the spread seen in the experiments with the four 24-channel tubes coated only with the 1 µm membrane and also lower than the spread found for the substrates. This decrease was also seen for the monotubes and again it indicates that the tubes have been uniformly coated.

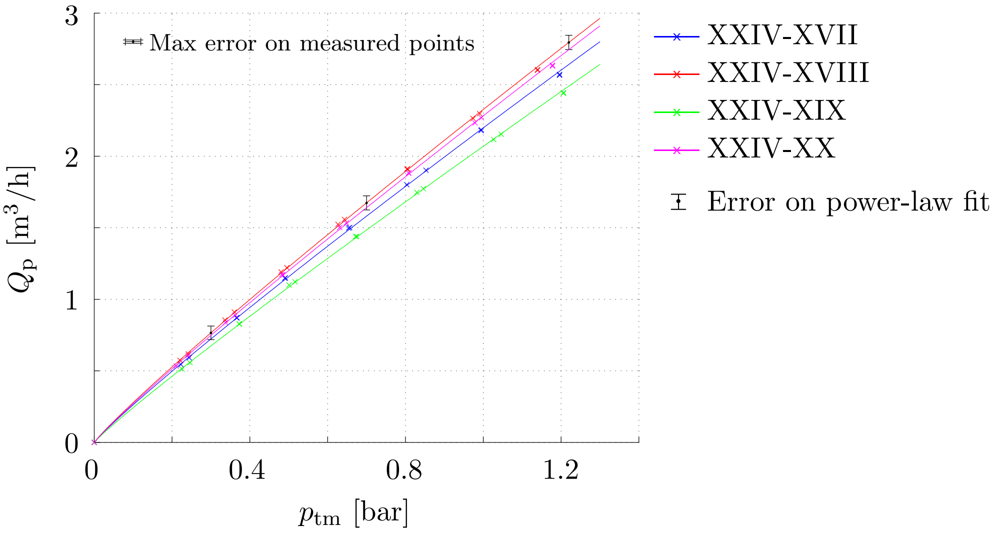

Figure 6.5: Plot of the measurements for four 24-channel tubes coated with the 0.1 μm membrane. The flow rate has decreased approximately 60% compared to the substrate experiments and is almost linearly related to the transmembrane pressure. The error on the power-law fits is given in three places on the slope of XXIV-XVIII. The spread on the measured flow rate from the tubes is 12%. The mean constants including their standard deviations found from the power-law fits are, $c_{\mathrm{s},01} = 0.93{\pm}0.01$ and $Q_{\mathrm{p}_{\mathrm{s},01}} = (2.2{\pm}0.1)\mathrm{m}^3/\mathrm{h}$.

6.2.2 0.04 μm membrane

Eight 24-channel tubes were coated with the 0.04 μm membrane. The results from the experiments are shown in Fig. 6.6 and it is seen that four of the 24-channel tubes lie very close in the bottom, while the other four differ significantly having a much higher flow rate. The exact same thing was seen for the monotubes coated with the 0.04 μm membrane, and again the four tubes with the high flow rate were the ones used for the 1 μm membrane experiments, see Appendix C.3.2. Bubble point experiments were carried out once more and again a much lower bubble point pressure was measured for the four tubes having a high flow rate compared to the other tubes. Thus we conclude that these 24-channel tubes have been poorly coated and they are omitted from the results for the 0.04 μm membrane.

Three of the four monotubes and all of the four 24-channel tubes used for the 1 μm membrane experiments have then been poorly coated with the second membrane layer. This has undoubtedly something to do with them being used in these experiments and it might be because of a biofouling layer, which prevents the 0.04 μm membrane from sticking to the surface of the tubes. This hypothesis has not been investigated, though, since it is not an important part of the work for this thesis.

The flow rate in the four 24-channel tubes lying in the bottom of Fig. 6.6 has decreased approximately 60% compared to the substrate experiments, and they have practically the same flow rate as the 24-channel tubes coated with the 0.1 μm membrane. Q_p and p_tm are almost linearly related with a mean power found from the four power-law fits of $c_{\mathrm{s},004} = 0.93$, exactly the same as found in the 0.1 μm membrane experiments. This tendency of equal flow rates through the 0.1 μm and 0.04 μm membrane was also seen for

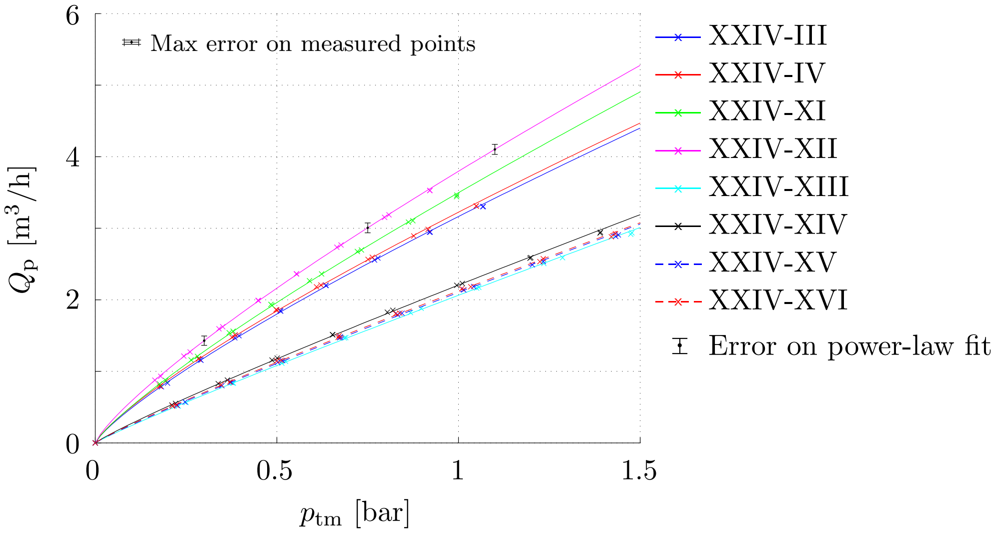

Figure 6.6: Plot of the measurements for the eight 24-channel tubes coated with 0.04 µm membrane. Variations of more than 90% are seen in the flow rate. Four of the 24-channel tubes lie close together in the bottom, while the four other tubes differ significantly having a much higher flow rate due to poor coating. The flow rate for the four tubes in the bottom has decreased approximately 60% at $p_\mathrm{tm} = 1\,\mathrm{bar}$ compared to the substrate experiments. The average constants including their standard deviations found from the power-law fits of the four 24-channel tubes in the bottom are, $c_{\mathrm{s},004} = 0.93 \pm 0.01$ and $Q_{\mathrm{p}_{\mathrm{s},004}} = (2.12 \pm 0.06)\mathrm{m}^3/\mathrm{h}$.

the monotubes. The pictures of the membranes on the monotubes showed that the 0.1 µm membrane layer was thicker than the 0.04 µm membrane, see Fig. 6.3(b) and (d), which was concluded to be the reason for the equal flow rates. It is therefore expected that the 0.1 µm membrane is thicker than the 0.04 µm membrane on the 24-channel tubes.

6.2.3 Investigation of the membrane thickness

This section has been abridged, and only the most important tendencies seen are described. As for our monotubes, we checked the membrane thicknesses of our 24-channel tubes using the optical Zeiss microscope. Six 24-channel tubes were chosen, two were coated with the 0.1 µm membrane (XXIV-XVIII and XXIV-XIX), and four were coated with the 0.04 µm membrane, two of these having a high flow rate (XXIV-III and XXIV-XII), and two having a low flow rate (XXIV-XIII and XXIV-XIV). We cut three cross-sectional slices from each tube, two slices 2 cm from each end, and one in the middle. The pictures of the 0.1 µm membrane and the 0.04 µm membrane presented in Figs. 6.7 and 6.8, respectively, show the tendencies seen for the coated 24-channel tubes.

Fig. 6.7(a) shows the corner of a channel in the mid section of XXIV-XIX. The 0.1 µm membrane layer lies evenly in the corner while the 1 µm membrane is missing. It can be seen in the top of the picture, but it disappears in the corner of the channel. This was seen in several regions of the six 24-channel tubes investigated and reveal that the 24-channel tubes have been poorly coated with the 1 µm membrane. The tendency was seen mostly

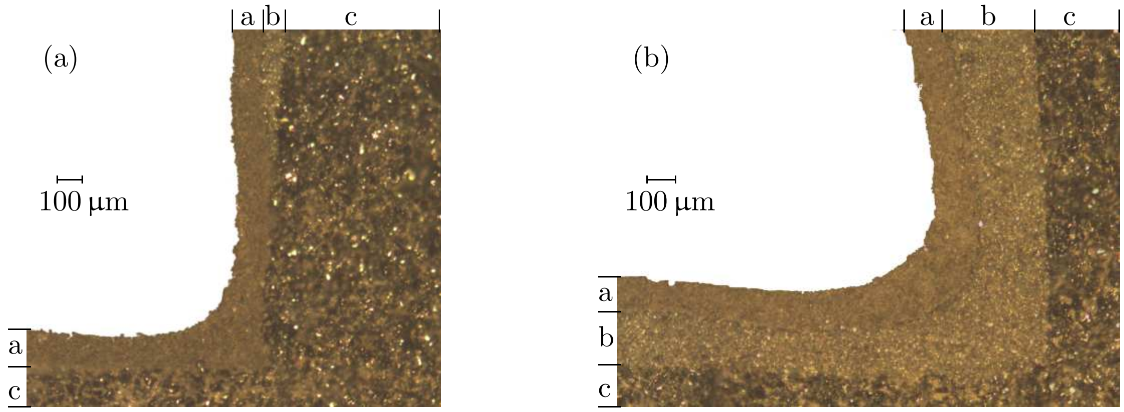

Figure 6.7: Pictures of the membrane thicknesses on the 24-channel tubes coated with the 0.1 µm membrane. 'a' refers to the outer membrane layer, 'b' is the middle layer, while 'c' is the substrate. (a) Corner of a channel in the mid section of XXIV-XIX. The 0.1 µm membrane lies evenly in the corner, but the 1 µm membrane is not visible. (b) Another channel in the same section. Both membrane layers are visible in the corner, though there is a tendency that the 1 µm membrane layer grows thinner closer to the corner.

in the small channels near the periphery of the tubes, thus it might be caused by a too low liquid flow in these channels during the coating. There was no sign of the 0.1 µm membrane missing in any of the corners.

In Fig. 6.7(b) both the membrane layers are visible and the picture shows how well the membranes could lie. Even here it is seen that the middle layer becomes thinner closer to the corner at both sides. This was mostly seen in the whole channels near the center of the 24-channel tubes. The average membrane thicknesses measured from the two tubes coated with the 0.1 µm membrane, were $w_1 = (50 \pm 50)\mu\text{m}$ and $w_{01} = (130 \pm 20)\mu\text{m}$ where subscript '1' and '01' refers to the 1 µm and 0.1 µm membrane, respectively. Comparing to the thicknesses measured at our monotubes, it is noticed that both membrane layers are significantly thinner at the 24-channel tubes. At the monotubes, the middle layer had a thickness of around 300 µm, and it is then six times thinner in average at the 24-channel tubes. The 0.1 µm membrane is approximately 30% thinner. This is probably due to the smaller channels. The big channels in the monotubes have a lower resistance therefore the fluid flows easier, and this might be reflected in the thicker membrane layers.

Some pictures of the 24-channel tubes coated with the 0.04 µm membrane are shown in Fig. 6.8. Fig. 6.8(a) shows a picture of a channel in one of the end sections of XXIV-XII. Neither of the two membrane layers are visible in the corner and only the 1 µm membrane can be seen to the left in the picture. This is seen in several regions of both the 24-channel tubes having a high flow rate, especially in the small channels near the periphery. The missing middle layer was also seen in the other 24-channel tubes, while the missing 0.04 µm membrane was seen in the monotubes with a high flow rate. As for the monotubes, the 24-channel tubes with a high flow rate had been used for the 1 µm membrane experiments. In Fig. 6.8(b) the thickest membrane layer found on XXIV-XII is seen. Even here the 0.04 µm membrane is only in the order of 10-15 µm.

Pictures of XXIV-XIV, which had a low flow rate, are shown in Fig. 6.8(c)-(d). They

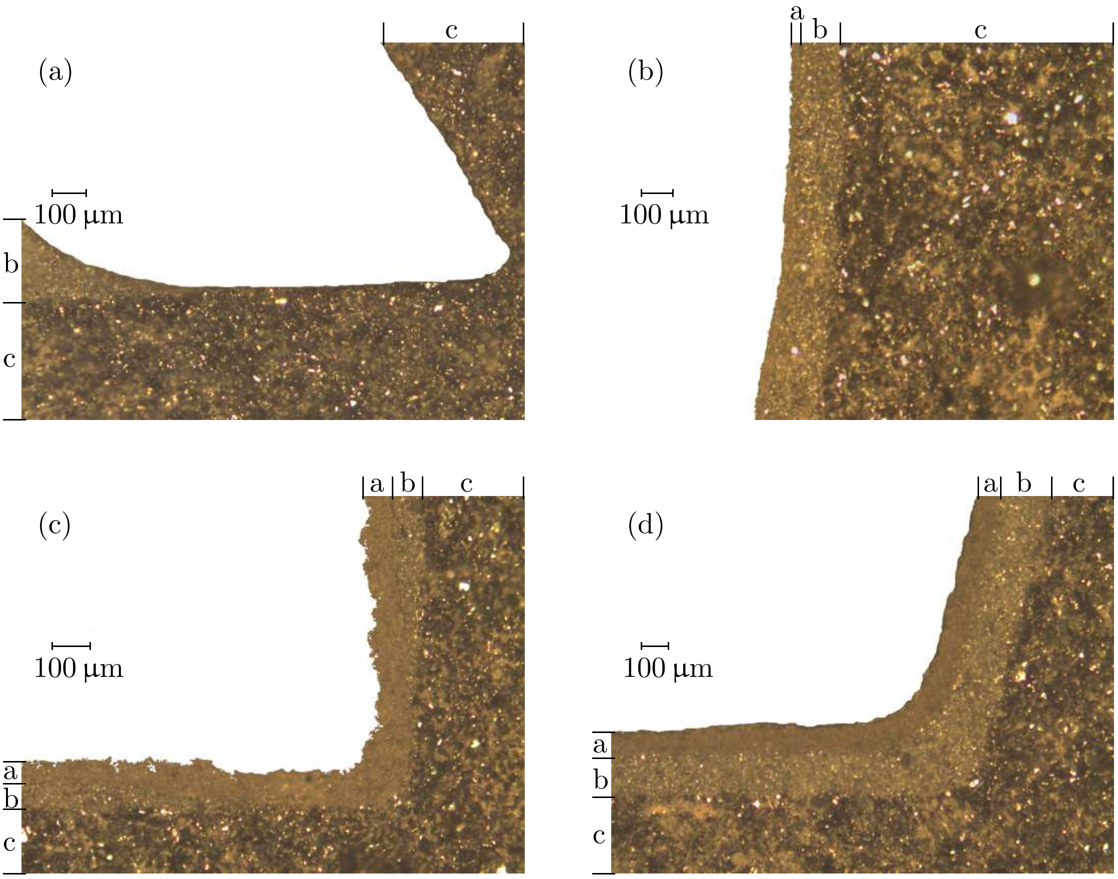

Figure 6.8: Pictures of the membrane thicknesses on the 24-channel tubes coated with the 0.04 µm membrane. The labels of the membranes and substrate are the same as in Fig. 6.7. (a) An end section of XXIV-XII. Neither of the two membrane layers are visible in the corner of the channel. (b) Another channel in the same section. Both membrane layers are visible, but the 0.04 µm membrane layer is very thin. (c) Mid section of XXIV-XIV. As for the 0.1 µm membrane, the 0.04 µm membrane lies evenly in the corner, but the 1 µm membrane is not visible. (d) Another channel in the same section. Both membrane layers are visible.

show the same tendencies as the pictures in Fig. 6.7 for XXIV-XIX coated with the 0.1 µm membrane. The middle layer is missing in some places, see Fig. 6.8(c), while there was no sign of the 0.04 µm membrane missing anywhere. The average membrane thicknesses were measured to be, $w_1 = (50 \pm 50)\,\mu\text{m}$ and $w_{004} = (80 \pm 15)\,\mu\text{m}$. Like for the monotubes, the 0.04 µm membrane layer is then significantly thinner, than the 0.1 µm membrane layer on the 24-channel tubes.

6.2.4 Comparison of substrate and membranes

All the experiments we have carried out with the 24-channel tubes are compared in Fig. 6.9. We see the same tendencies, as we did in the comparison of the monotube experiments. At $p_{\text{tm}} = 1\,\text{bar}$ the flow rate has decreased roughly 20% from the substrates to the 1 µm

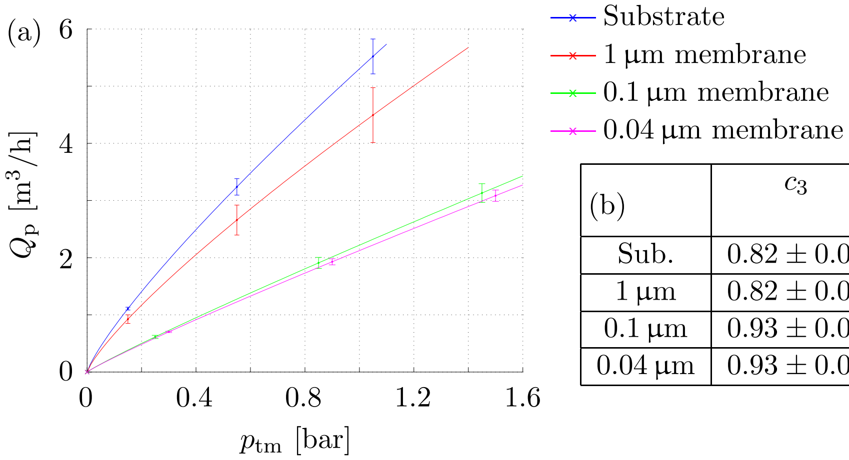

(b)	c_3	Q_{p_3} [m^3/h]
Sub.	0.82 ± 0.02	5.3 ± 0.3
1 µm	0.82 ± 0.02	4.3 ± 0.5
0.1 µm	0.93 ± 0.01	2.2 ± 0.1
0.04 µm	0.93 ± 0.01	2.12 ± 0.06

Figure 6.9: Comparison of 24-channel tubes. (a) The mean power-law fits from the different experiments are plotted and the error bars represent the standard deviation on the power-law fits for each of the 24-channel tubes. (b) Table containing the average constants including their standard deviations for the power-law lines on the form $Q_p = Q_{p_3}(p_{tm}/1\,\text{bar})^{c_3}$. As seen for the monotubes the flow rate is almost equal for the 0.1 µm and the 0.04 µm membrane due to a higher thickness of the 0.1 µm membrane.

membrane experiments, and approximately 60% from the substrate to the 0.1 µm and 0.04 µm membrane experiments. Again the flow rates through the tubes with these two membranes are almost equal due the 0.1 µm membrane being thicker than the 0.04 µm membrane, as seen in the microscope pictures. The dispersion of the measurements, reflected in the errors bars on the power-law lines, decrease from the substrate experiments to the membrane experiments, with the exception of the 1 µm membrane experiment. This is because the 24-channel tubes had been poorly coated with the 1 µm membrane. The reason for this is unknown.

The figure also shows that the flow rate becomes almost linearly related to the transmembrane pressure in the 0.1 µm and 0.04 µm membrane experiments, which is especially clear when looking at the power c_3 from the power-law fits, see Fig. 6.9(b). The closer c_3 is to 1, the more linear the fit.

6.3 Summary

Some thin-walled monotubes and some 24-channel tubes are coated with two different types of membrane, a 0.1 µm membrane and a 0.04 µm membrane. Ten monotubes and eight 24-channel tubes are coated with the 0.04 µm membrane, while four monotubes and four 24-channel tubes are coated with the 0.1 µm membrane. Experiments with the coated monotubes show that Darcy's law is valid.

In the experiments with both monotubes and 24-channel tubes coated with a 0.04 µm membrane, three of the ten monotubes, and four of the eight 24-channel tubes differ significantly from the others having a surprisingly high flow rate. Bubble point measurements showed that the seven tubes had a significantly lower bubble point pressure, compared

Table 6.1: Measured thicknesses w, in µm, with estimated errors of the three different membranes used. The membrane layers were significantly thinner on the 24-channel tubes compared to the monotubes.

	w_1 [µm]	w_{01} [µm]	w_{004} [µm]
Monotubes	295 ± 15	180 ± 20	120 ± 20
24-channel tubes	50 ± 50	130 ± 20	80 ± 15

to the other tubes coated with the 0.04 µm membrane, and it was suspected that the 0.04 µm membrane was either completely missing, or at least very thin on the seven tubes. We therefore decided to investigate the membrane thickness using a microscope, and this confirmed that the 0.04 µm membrane nearly was nonexistent on the seven tubes with a high flow rate. Therefore these tubes are neglected in the final results. We have used all the seven tubes for initial experiments with the middle layer (the 1 µm membrane) and we suspect that biofouling on the surface of the middle layer, making it difficult for the 0.04 µm membrane to stick to the surface, is the reason for the missing 0.04 µm membrane layer.

Both monotube and 24-channel tube experiments show that the flow rates are almost equal with the 0.1 µm membrane and the 0.04 µm membrane. This was not expected, since the permeability in the 0.04 µm membrane should be much lower than the permeability in the 0.1 µm membrane. Investigation with a microscope show that the 0.1 µm membrane is approximately 30% thicker than the 0.04 µm membrane on both monotubes and 24-channel tubes and this is assumed to be the reason for the equal flow rates. This investigation also show that the 1 µm membrane is missing in some regions of the 24-channel tubes and generally the membrane layers are significantly thinner on the 24-channel tubes compared to the monotubes, see Table 6.1. This is assumed to be due to the smaller channels having a lower fluid flow during the coating process. The reason for the poor coating of the 1 µm membrane on the 24-channel tubes is unknown.

An estimate of the permeabilities of the 0.1 µm and 0.04 µm membranes was found from monotube experiments assuming a membrane thickness of 0.1 mm for both membranes. The 1 µm membrane is neglected. The permeabilities were found to be

$$k_{01} = 2.2 \times 10^{-14}\,\mathrm{m}^2, \tag{6.4}$$

$$k_{004} = 1.8 \times 10^{-14}\,\mathrm{m}^2. \tag{6.5}$$

These values should not be seen as the correct membrane permeabilities, but only as estimates that can be used in our simulations.

Chapter 7

Numerical models and flow simulations

Two numerical models are developed to describe the flow in porous SiC-tubes. First a simple 2D model is developed based on potential flow theory to describe flow in a cross-section of a tube. The model is implemented in the program COMSOL MULTIPHYSICS™ Version 3.4 (COMSOL). Second, we develop a 3D model based on equivalent circuit (EC) theory using the program MATLAB Version 7.4. 2D EC models are made of the cross-section of a tube and these EC models are connected using the hydraulic resistance in the channels of the tube. In that way a 3D EC model is created that describes the flow in the entire tube. The two numerical models are presented in the following.

The numerical models are first used to simulate the flow in the substrate and the results are compared to the experimental results with substrate tubes presented in Chapter 5. The models are extended to include the membrane layer and these results are compared with the experiments with tubes coated with the 0.04 μm membrane presented in Chapter 6. The permeability of the substrate and the 0.04 μm membrane found in the monotube experiments will be used in the two models.

7.1 Comsol model

We have made a simple numerical 2D model based on the Laplace equation for the pressure, presented in Section 2.5, and Darcy's law, Eq. (2.9), for the velocity in the porous SiC. Solving the Laplace equation combined with Darcy's law is used in [14, 15]. The model is thus based on potential flow theory. The numerical model is implemented in COMSOL and the graphical user interface (GUI) is utilized.

We solved the pressure distribution and flow rate for a monotube analytically in Section 2.5 and the COMSOL simulations of monotubes are therefore left out since they are trivial. The simulations presented here are made for pure SiC-substrates without membrane. The permeability used for the porous SiC is the average permeability found in the monotube experiments $k_\mathrm{s} = 8.3 \times 10^{-13}\,\mathrm{m}^2$, see Section 5.2.

7.1.1 24-channel tube

The permeate flow rate Q_{p} is found by integrating the normal velocity $\mathbf{v}_{\mathrm{n}}$ at the surface of the 24-channel tube. The normal velocity is found as

$$\mathbf{v}_{\mathrm{n}} = (\mathbf{v} \cdot \mathbf{n})\mathbf{n}, \tag{7.1}$$

where $\mathbf{n}$ is the normal vector at the surface boundary, pointing outwards, and $\mathbf{v}$ is the velocity vector.

Only one eighth of the cross-section of a 24-channel tube is modeled in Comsol due to symmetry and thereby the number of elements in the simulations can be kept at a minimum. The modeled geometry is shown in Fig. 7.1 which also shows the labels of the different channels and the used boundary conditions (BC). Neumann BC's are used at the symmetry boundaries (green color), while Dirichlet BC's are applied at the boundaries of the channels (red color) and the rim of the tube (blue color). The pressures at the two boundaries are $p^* + \Delta p$ and p^*, respectively, where p^* is a specified reference pressure and Δp is the pressure difference from the channels to the surface. Throughout this section we use $\Delta p = 1\,\mathrm{bar}$ and $p^* = 0\,\mathrm{bar}$.

The mesh is generated with the free mesh feature incorporated in Comsol, using triangular elements. A convergence analysis is made to find the necessary number of elements in the mesh in order to get an accurate solution and at the same time keep the calculation time at a minimum. The permeate flow rate is calculated for increasing numbers of elements in the mesh and the relative error ε between two solutions is calculated as $\varepsilon = |Q_{\mathrm{p}_i} - Q_{\mathrm{p}_{i-1}}|/Q_{\mathrm{p}_i}$. The error is plotted versus the number of elements in Fig. 7.2 and it is clearly seen that it converges towards zero. The figure shows that the relative error is below 0.1 % when using above 5000 elements, which we find acceptable for these simulations. Thus we use approximately 5000 elements in the simulations of the 24-channel tube. The resulting pressure distribution is shown in Fig. 7.3 as a surface plot. It is

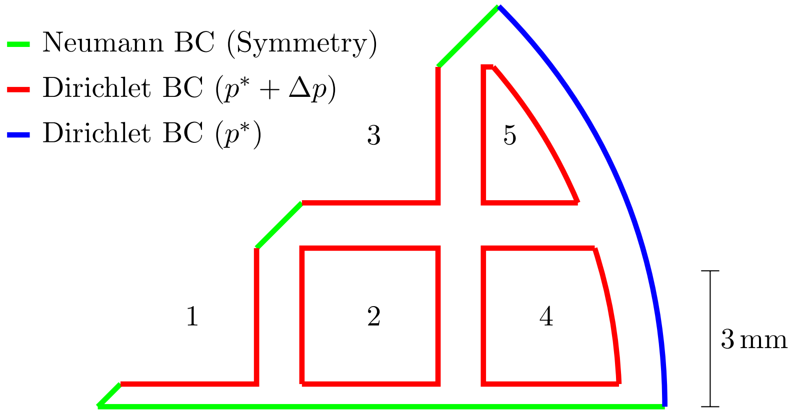

Figure 7.1: Cross-section of one eighth of a 24-channel tube. The color on the boundaries show where the different boundary conditions (BC) are applied. A Neumann BC is used on the symmetry boundaries and Dirichlet BC's are used at the channel boundaries and the rim of the tube, with $p^* + \Delta p$ and p^* given at the two boundaries, respectively. The channels are labeled as shown.

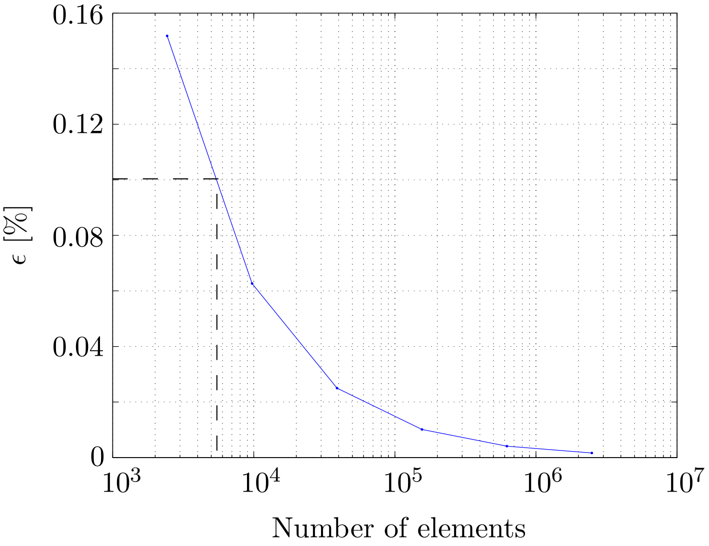

Figure 7.2: Convergence of the permeate flow rate Q_P leaving the tube. ε, in %, is the relative error of Q_P between two solutions with increasing number of elements, $\varepsilon = |Q_{\text{P}_i} - Q_{\text{P}_{i-1}}|/Q_{\text{P}_i}$. The relative error is below 0.1% when using above 5000 elements.

seen that the pressure is almost constant behind the peripheral channels, channel 4 and 5, which is because they make a screening pressure around the inner channels, channel 1, 2 and 3. There is thus only a pressure gradient present from the peripheral channel to the surface, and as it is the pressure gradient that drives the flow, the contribution from the inner channels is almost zero. Nearly all the permeate flow rate in a 24-channel tube is therefore delivered from channel 4 and 5.

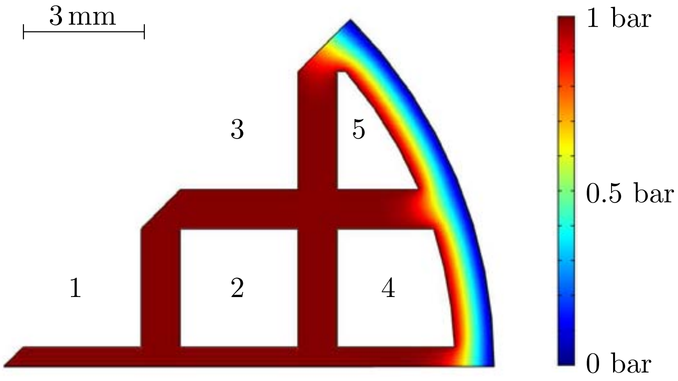

Figure 7.3: Pressure distribution for one eighth of the 24-channel tube with $\Delta p = 1\,\text{bar}$ and $p^* = 0\,\text{bar}$. The peripheral channels make a screening pressure around the inner channels which makes them inefficient as it is the pressure gradient that drives the flow.

The permeate flow rate calculated from the modeled part of the 24-channel tube is multiplied by 8 to get the full cross-section and then by $L = 305\,\mathrm{mm}$ to get the flow rate through a tube with same length as the ones used in the experiments. The flow rate from the simulations is then found to be $Q_\mathrm{p} = 6.51\,\mathrm{m^3/h}$, of which 98% is delivered from the peripheral channels.

Since we use $\Delta p = 1\,\mathrm{bar}$ and $p^* = 0\,\mathrm{bar}$ the simulations are made at a transmembrane pressure of $p_\mathrm{tm} = 1\,\mathrm{bar}$ and the corresponding average flow rate found from the experiments with the 24-channel tubes was $Q_\mathrm{p} = 5.3\,\mathrm{m^3/h}$, see Section 5.3. The flow rate calculated from the COMSOL model is then 23% higher than the measured flow rate. In the 2D model we assume constant pressure throughout the channels as we neglect the influence of hydraulic resistance. The experiments with the 24-channel tubes show a significant pressure drop down the length of the tubes and therefore it is expected that the simulations predict a too high flow rate. Though the simulations do not compensate for the pressure drop in the channels, they still describe the flow in the porous SiC well. Interesting phenomena, like the peripheral channels screening the inner channels, can be seen using this simple numerical model.

7.2 Equivalent circuit model

The nonlinear relation between flow rate and transmembrane pressure seen in the experiments with long, thin-walled monotubes and 24-channel tubes cannot be simulated in the simple 2D COMSOL model. We therefore develop a new model using the program MATLAB. The analog between the Hagen-Poiseuille law and Ohm's law described in Section 2.4 will be used to build a so-called equivalent circuit (EC) model, also called a resistor model, in which the hydraulic channel resistance can be taken into account. The hydraulic resistance in the channels is calculated from the energy equation and the friction factor described in Section 2.3, and the flow in the porous material is assumed to obey Darcy's law. The channels in the tubes are assumed to be smooth in all the simulations. As in the COMSOL model a permeability of $k_\mathrm{s} = 8.3 \times 10^{-13}\,\mathrm{m^2}$ is used in the SiC-substrate. Any inlet and outlet BC's on the tubes are not included in the model.

7.2.1 Monotube

An EC model of a short monotube is shown in Fig. 7.4. The model describes the flow in a monotube placed in a dead-end setup, as in the conducted experiments. The unknown flow rates and their positive direction, indicated by arrows, are also shown. The length $L = 305\,\mathrm{mm}$ of the monotube is discretized into ten parts, each with a length of $\Delta L = L/10$, in order to dissolve the nonlinear relations along the channels sufficiently but still keep the number of equations at a minimum. The linear relation between pressure difference and flow rate in the substrate is found from Eq. (2.41),

$$\Delta p = R_\mathrm{s} Q, \qquad R_\mathrm{s} = \frac{\eta}{k} \frac{\ln(1 + \frac{2w}{d_\mathrm{c}})}{2\pi L}, \tag{7.2}$$

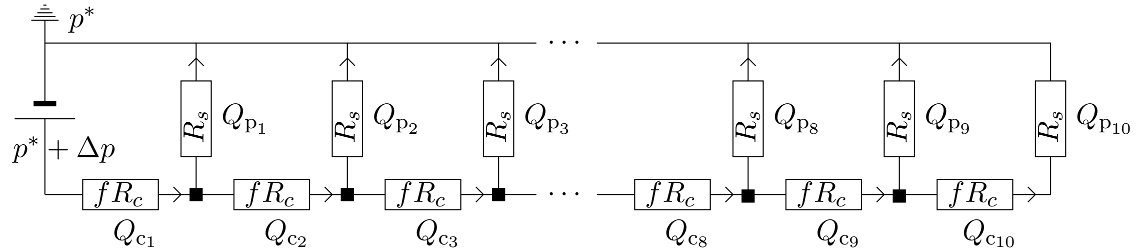

Figure 7.4: EC model of a monotube in a dead-end simulation. The length of the monotube is discretized into ten parts. The unknown flow rates and their positive directions are shown as well as the nodes symbolized as black squares. p^* is the reference pressure, Δp is the pressure difference applied at the inlet of the monotube, R_c and R_s are the channel resistance and substrate resistance, respectively, and Q_{c_1} to $Q_{\mathrm{c}_{10}}$ and Q_{p_1} to $Q_{\mathrm{p}_{10}}$ are channel flow rates and permeate flow rates.

where R_s is the substrate resistance, d_c is the channel diameter and w the wall thickness. The channel flow is found from Eq. (2.26) and repeated here for convenience,

$$\Delta p = R_\mathrm{c}\ f(\mathrm{Re})\ Q^2, \qquad R_\mathrm{c} = \frac{L}{D^5}\frac{8\rho}{\pi^2}, \tag{7.3}$$

where R_c is the channel resistance. In this model the friction factor varies throughout the channel, because of a varying channel flow rate and consequently a varying Reynolds number, and the friction factor is found as described in Section 2.3. The total permeate flow rate delivered from the monotube is found as the sum of the individual ten permeate flow rates Q_{p_1} to $Q_{\mathrm{p}_{10}}$ where $Q_{\mathrm{p}_{10}} = Q_{\mathrm{c}_{10}}$ due to the dead-end simulation. Q_{c_1} to $Q_{\mathrm{c}_{10}}$ are the channel flow rates. When the flow rates are known the pressure down the length of the channel can be calculated from Eq. (7.3).

The equations describing the flow in a monotube are found by applying Kirchhoff's laws, described in Section 2.4, to the EC model, see Fig. 7.4. This means that at every node (black squares) the sum of flow rates entering and leaving is zero and in every closed loop the sum of all pressure differences is also zero. This leads to 19 equations with 19 unknown flow rates Q_{c_1} to $Q_{\mathrm{c}_{10}}$ and Q_{p_1} to Q_{p_9}. The equations are implemented in MATLAB and the system of linear and nonlinear equations are solved by MATLAB's nonlinear system solver, `fsolve`.

A reference pressure of $p^* = 0\,\mathrm{bar}$ is used and different Δp's are applied at the inlet of the monotube in order to find the relation between permeate flow rate and transmembrane pressure. The transmembrane pressure is found as $(\Delta p + p_{\mathrm{c},10})/2$, where $p_{\mathrm{c},10}$ is the channel pressure found at the end of the monotube. The results of the simulations of a thin-walled monotube are seen in Fig. 7.5 together with the average best-fitted line found in the monotube experiments. The good agreement seen is expected since the permeability used in the simulations is extracted from the monotube experiments. It is seen that the hydraulic channel resistance in the thin-walled monotube is negligible in the simulations as the relation is linear. This was expected since the experiments with the monotubes showed a linear relation between flow rate and transmembrane pressure.

The EC model is also applied to a long, thin-walled monotube with a length of $L = 1\,\mathrm{m}$. The only difference compared to the short, thin-walled monotube is thus the length. The

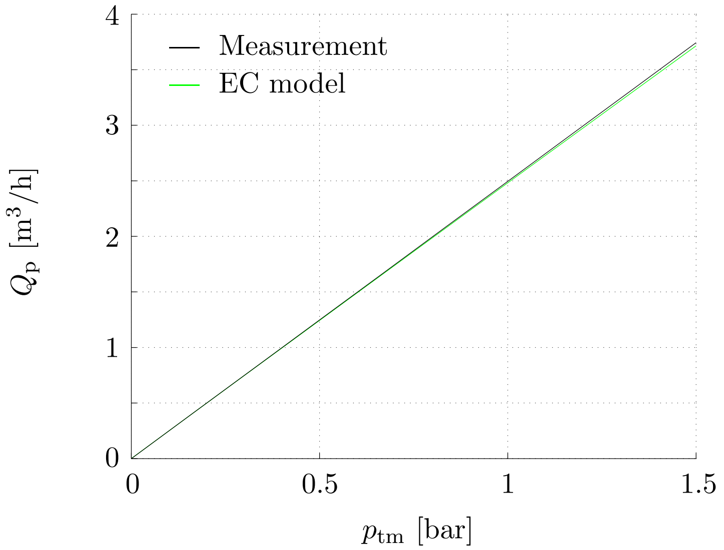

Figure 7.5: Comparison for permeate flow rate Q_p versus transmembrane pressure p_tm of the measurements and simulations for a short, thin-walled monotube. The permeability k_s is extracted from the monotube experiments and therefore the good agreement between simulations and experiments is expected.

results from the simulations are shown in Fig. 7.6 and compared to the experiments represented as the average fitted line through all measuring points. A 2D Comsol simulation is included as reference. Comparing the two simulations show that the hydraulic channel resistance is of importance in the long monotube. The EC model and the experimental

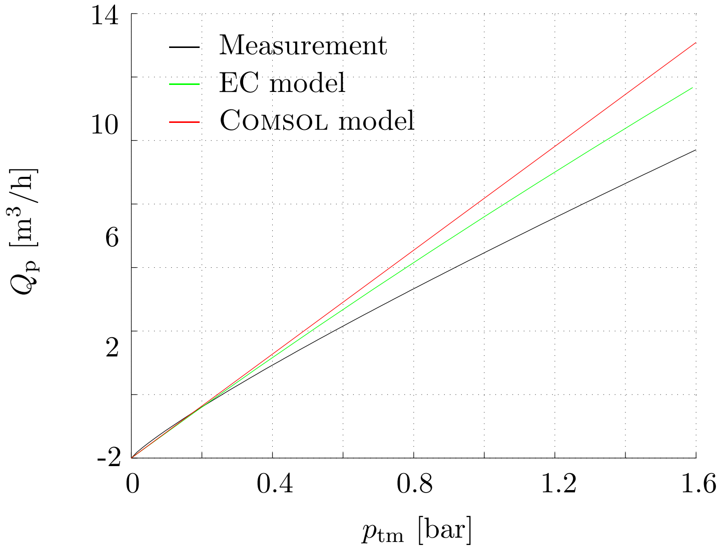

Figure 7.6: Comparison of the simulations to the average fitted line from the measurements for a thin-walled, long monotube. A 2D Comsol simulation of the long monotube is included as a reference. The resistance caused by friction in the channel having an important influence on the flow.

results agree well at low permeate flows which is expected since the channel resistance is negligible here. As the flow rate increases, and thus also the channel resistance, it becomes clear that only some of the observed nonlinearity is described by the EC model. The relative error between the EC simulations and the experiments is approximately $\varepsilon = 20\%$ at $p_{\mathrm{tm}} = 1.5\,\mathrm{bar}$. The too high flow rate in the EC simulations is expected since the channel in the monotube is assumed to be smooth as the relative roughness of porous SiC is unknown. If the roughness is taken into account the channel resistance will increase and the flow rate will consequently decrease, therefore the simulations might agree better with the experimental results. However, the roughness of the SiC has not been investigated further.

7.2.2 24-channel tube

The EC model of a 24-channel tube is much more complicated than the model of a monotube. It is build up from 2D models of the cross-section of a 24-channel tube connected by 1D hydraulic resistances in the channels. Thus it is effectively a 3D EC model.

First a 2D EC model is made of one eighth of the cross-section of a 24-channel tube, see Fig. 7.7. The black circles indicate channels and the black squares indicate nodes. Kirchhoff's laws are again used to find the governing equations for the flow giving 27 equations with 27 unknown flow rates. These equations are implemented in MATLAB and

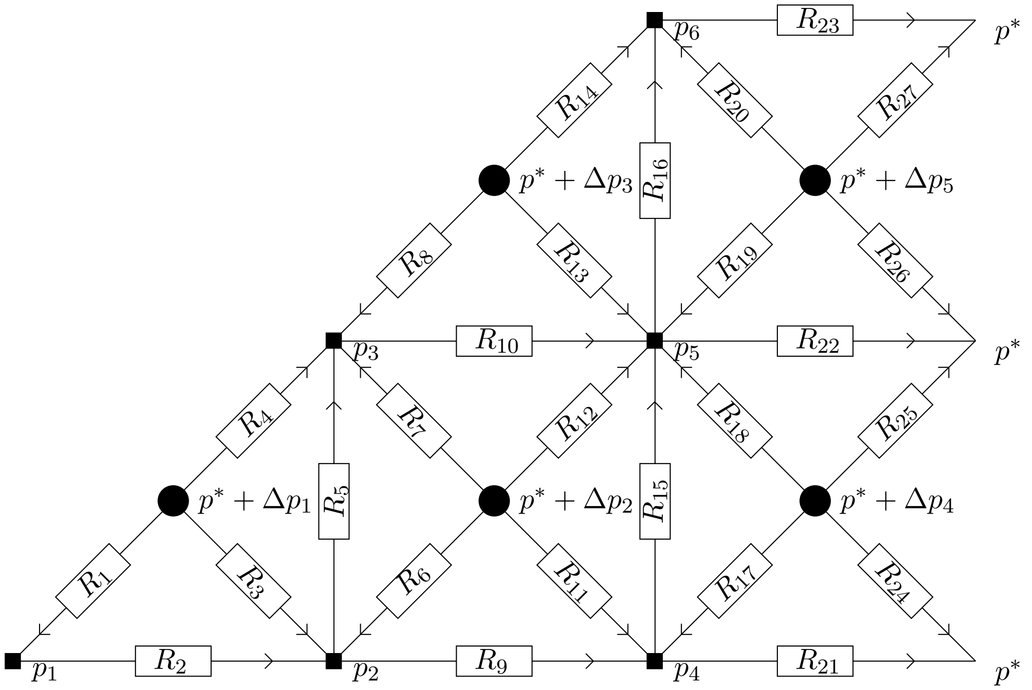

Figure 7.7: EC model of one eighth of the cross-section of a 24-channel tube. The five channels are symbolized as black circles and the nodes are the black squares. The positive direction of the flow rates is indicated with arrows.

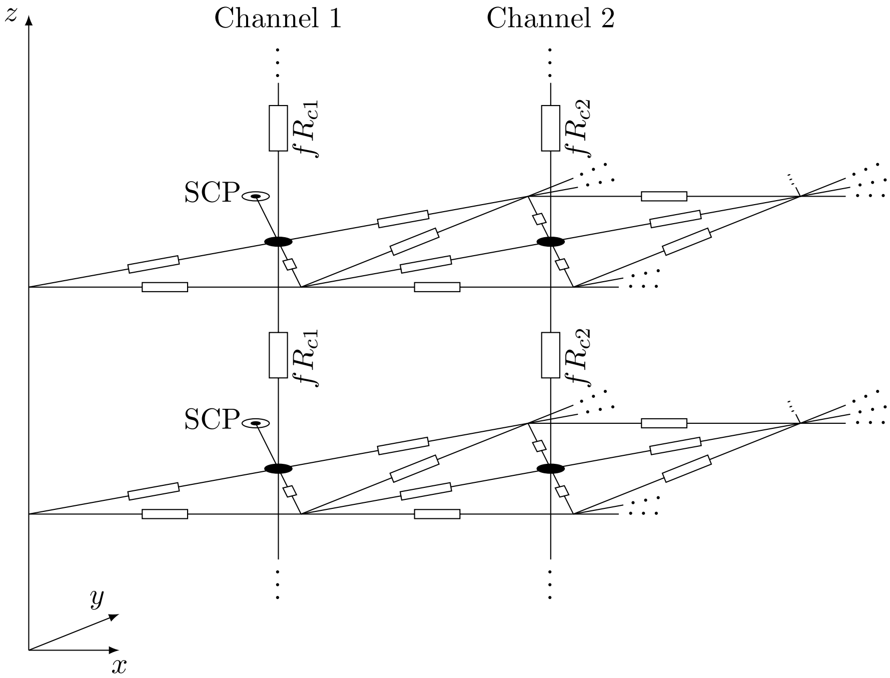

Figure 7.8: A segment of the 3D EC model of a 24-channel tube. The 2D EC models are connected by hydraulic resistances in the channels. A correction is made in channel 1 and 3 due to symmetry. A flow rate equal to the permeate flow rate calculated from these channels is lead into the symmetry correction point (SCP) to get the correct flow rate onwards in the channels.

the system of linear equations is solved with the \-solver. The substrate resistances are also unknown. An initial guess is made based on a simple 1D Darcy flow and thus

$$R_{\mathrm{s}} = \frac{w\eta}{\mathcal{A}k}. \tag{7.4}$$

The EC model is then calibrated against the developed 2D COMSOL model and in that way, the value of the 27 substrate resistances is found in an iterative process where the flow rate from each of the channels is compared to the corresponding flow rate in the COMSOL model. If the flow rate deviates, the resistances are changed and this iterative process only stops when the deviation between the COMSOL model and the EC model is below 1%. The 2D EC model is then converted into a function, which uses the pressure in the channels as input and gives the permeate flow rate from each of the channels as output.

The 3D EC model is made by connecting one 2D EC model to the next using hydraulic resistances in the channels, see Fig. 7.8. The 3D model is also shown in Fig. 7.9 where the 2D EC models are replaced by rectangles and the model is rotated 90°. The length of the tube is discretized into eleven channel resistances and ten 2D EC models. The experiments with 24-channel tubes are conducted in a dead-end setup, and thereby the pressures at the end of the channels are equal. This is modeled by connecting the five channels at the rear end, see Fig. 7.9.

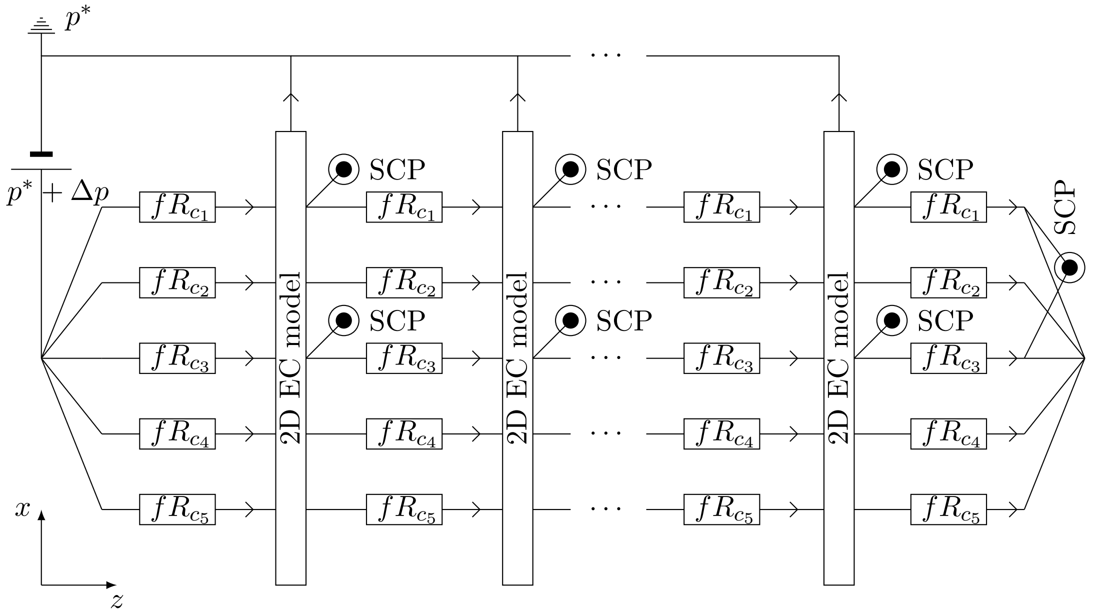

Figure 7.9: 3D EC model of one eighth of a 24-channel tube. The 2D EC models are modeled as seen in Fig. 7.7. At the rear end the channels are connected in order to ensure equal pressure in the end of the channels. The arrows indicate the positive direction of the flow rates. SCP is the symmetry correction point.

The five channels have different hydraulic resistances due to different hydraulic diameters $d_{\mathrm{h}} = (4\mathcal{A})/P$, where $\mathcal{A}$ is the cross-sectional area and P the wetted perimeter. The hydraulic diameter is used because the channels are quadrilateral and the calculated resistances are based on circular channels. The inner channels, channel 1, 2 and 3, have the same hydraulic diameter of $d_{\mathrm{h}} = 3\,\mathrm{mm}$, but the peripheral channels, channel 4 and 5, have smaller hydraulic diameters of $d_{\mathrm{h}} = 2.9\,\mathrm{mm}$ and $d_{\mathrm{h}} = 1.7\,\mathrm{mm}$, respectively.

In the EC model all the channels, even the channels that should be halved due to symmetry, i.e. channel 1 and 3, are handled as whole channels in order to find their hydraulic resistances and subsequently the pressure drops. Since only half of the symmetry channels are modeled in the 2D EC model only half of the permeate flow rate leaves these channels in the 2D model. Thus at every node where a 2D EC model is connected with a symmetry channel, a correction is made to ensure that the right flow rate proceeds down the channel. A flow rate equal to the permeate flow rate calculated from the symmetry channel is lead in to a so-called symmetry correction point (SCP) to get the correct flow rate onwards in the channels, see Figs. 7.8 and 7.9. Likewise the correction is applied at the node in the rear end of the EC model to ensure that the correct quantity of flow proceeds in the model.

Kirchhoff's laws are applied to the EC model, leading to 156 equations with 156 unknowns, both flow rates and pressures, solved in MATLAB with the nonlinear system solver `fsolve`. The transmembrane pressure is calculated using the given pressure difference Δp applied at the inlet of the 24-channel tube and the pressure found at the outlet of the

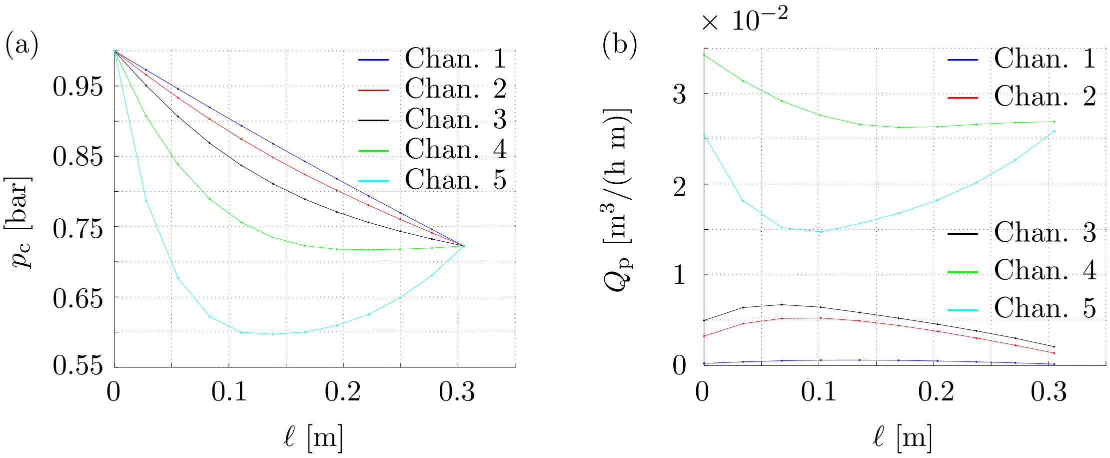

Figure 7.10: (a) Pressure p_c in the channels along the length ℓ of a 24-channel tube. A massive pressure drop is seen in the first section of channel 5 while a pressure increase is seen in the last half. (b) Permeate flow rate Q_p from the five channels along the length of a 24-channel tube. The peripheral channels deliver most of the total permeate flow while the contribution from the inner most channel, channel 1, is negligible.

tube. The reference pressure is $p^* = 0$ bar.

The pressure in the channels along the length of the tube is shown in Fig. 7.10(a) with $\Delta p = 1$ bar. The pressure is decreasing nearly linearly in channel 1 while it becomes more nonlinear in channel 2 and 3 with a total pressure drop of 0.27 bar. In channel 4 the pressure decreases significantly in the first half of the tube and then becomes almost constant in the last half. A massive pressure drop of around 0.4 bar is seen in the first half of channel 5, and in the last half the pressure then increases to 0.73 bar. The large pressure drop in channel 4 and 5 is both due to a higher friction as a consequence of the smaller hydraulic diameter and their higher permeate flow rate, compared to the other channels. The pressure increase seen in channel 5 indicates that there is a flow going back through the channel in the last half coming from channel 1, 2 and 3. These channels are then feed channels for the peripheral channels increasing their efficiency regarding permeate flow rate in the last half of the tube.

The amount of permeate flow rate from the five channels along the length of a tube is shown in Fig. 7.10(b) with $\Delta p = 1$ bar. The two peripheral channels, channel 4 and 5, are much more efficient than the other channels as it was seen in the COMSOL model.

The permeate flow rates from the peripheral channels decrease in the first sections of the tube and then increase towards the end of the tube, this is most significant in channel 5. This is because of the dead-end simulation in which all the flow has to permeate through the porous walls. The easiest way for the fluid in the inner channels to permeate out of the tube is then to flow back through the peripheral channels and permeate out of the walls here.

The pressure drop Δp_{tube} lengthwise in a 24-channel tube is estimated at different permeate flow rates and compared to the measured data, see Fig. 7.11. The measured data is represented as the average fitted line through all the measuring points. Fig. 7.11 shows that the simulated pressure drop is comparable to the measured pressure drop, but

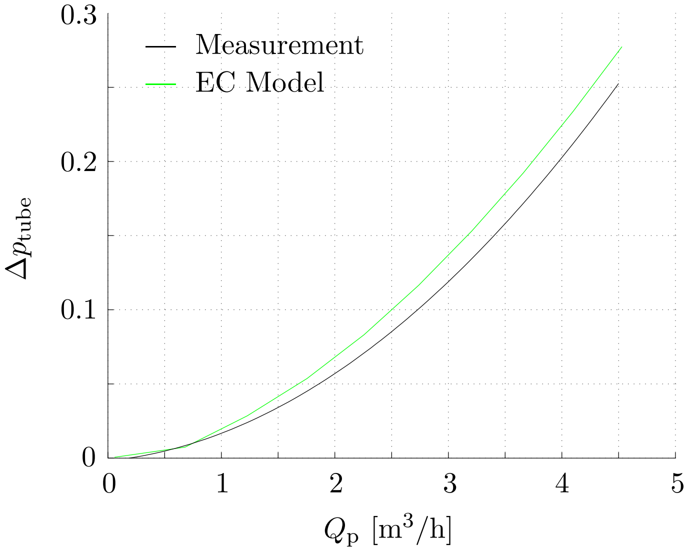

Figure 7.11: The calculated pressure drop Δp_{tube} down the length of a 24-channel tube is compared to the measured pressure drop at different permeate flow rates, Q_p. The measured pressure drop is represented as the average fitted line from the experiments.

the EC model estimates a slightly too high pressure drop with a relative error of $\varepsilon = 10\%$ at a flow rate of $Q_\text{p} = 4.5\,\text{m}^3/\text{h}$. It is a bit surprising that the model predicts a higher pressure drop than measured since the channels are assumed smooth. The deviation is most likely due to the lack of inlet and outlet BC's, but we can conclude that the EC model includes the most vital parts in describing the pressure drop down the tube.

The permeate flow rate predicted by the EC model and the COMSOL model is compared to the results from the experiments at different transmembrane pressures, see Fig. 7.12. The experimental results are represented as the average power-law fit. The EC model and the experimental results agree reasonably well with a maximum relative error of $\varepsilon = 14\%$ at $p_{\text{tm}} = 0.3\,\text{bar}$.

Since the model only includes hydraulic resistance caused by wall friction, assuming smooth surfaces, while no inlet and outlet conditions or inertial forces are included, we expected a higher flow rate from the simulations compared to the measured flow rate. However, it is seen, that the model predicts a lower flow rate in the investigated area. Surprisingly, the COMSOL model also predicts a lower flow rate until $p_{\text{tm}} = 0.3\,\text{bar}$ than the experiments which is not expected as the COMSOL model is a linear model. We are confident that our measurements have been conducted correctly and we suspect that the unexpected deviation is due to the permeability used in the simulations. This was found from the monotube experiments and is assumed to be correct for the 24-channel tubes. As described in Section 5.2.4 we found that the permeability could increase significantly in the SiC if the tubes were re-sintered. We could not fabricate the 24-channel tubes ourselves and these were provided by CoMeTas, and we can therefore not rule out the possibility that they have been re-sintered thus having a higher permeability than assumed in the simulations. This would explain the unexpected deviation between the experimental

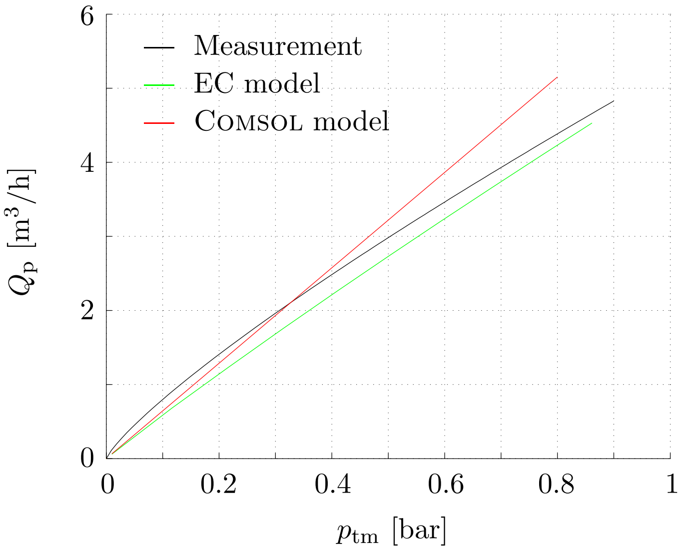

Figure 7.12: Comparison of the permeate flow rate found in the EC model and experiments with 24-channel tubes. The experiments are represented as the average power-law fit found. The 2D COMSOL model is included as a reference. The experiments have a higher flow rate than even the COMSOL model until $p_\mathrm{tm} = 0.3$ bar, which is unexpected.

results and the simulations.

Still, the 3D EC model of a 24-channel tube shows good results and agrees well with the experimental results. It describes some of the nonlinear effects observed in the experiments and additionally it shows that there is a large pressure drop in the peripheral channels, due to the smaller hydraulic diameters, which decreases the efficiency of the tube regrading the permeating flow rate.

7.3 Membrane simulations

A membrane layer is added on the surface of the tubes in the two numerical models. The thickness of the membrane layer is assumed to be 0.1 mm as when the permeability of the membranes was estimated, see Chapter 6. In the COMSOL model the membrane is modeled as an extra thickness added on the inside of the channels, while it is included as an extra resistance in a serial connection with the substrate resistance in the EC model. The permeability $k_{004} = 1.8 \times 10^{-14}\,\mathrm{m}^2$ of the 0.04 µm membrane found in Section 6.1.2 will be used in the simulations because most of the experiments are conducted with this membrane and because the same tendencies are seen in the experiments with the 0.1 µm membrane and the 0.04 µm membrane.

7.3.1 Comsol model

The Dirichlet BC $p^* + \Delta p$ is applied at the boundary between the channels and the membrane layer and a Neumann condition is applied on the internal boundaries between

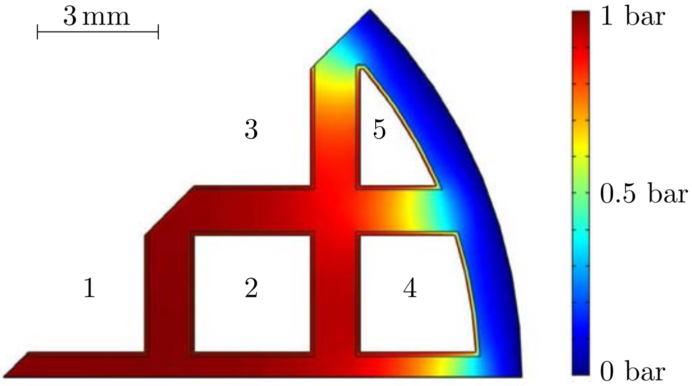

Figure 7.13: Pressure distribution for one eighth of a 24-channel tube coated with a 0.04 µm membrane with $\Delta p = 1\,\mathrm{bar}$ and $p^* = 0\,\mathrm{bar}$. The peripheral channels still make a screening pressure around the inner channels, though not as significant as seen in the substrate simulations.

the membrane layer and the substrate, $\mathbf{n}\cdot\mathbf{v}_\mathrm{s} = \mathbf{n}\cdot\mathbf{v}_{004}$, where $\mathbf{v}_\mathrm{s}$ and $\mathbf{v}_{004}$ are the velocities in the substrate and 0.04 µm membrane, respectively. The remaining BC's described in Section 7.1 are left unchanged. More elements are needed in the mesh because the thin membrane layer has to be dissolved sufficiently. A convergence analysis states that approximately ten times as many elements should be used in order to get a relative error below 0.1%, compared to the substrate model. Thus approximately 5×10^4 elements are used in these simulations.

The same pressures as in the substrate simulations are used, i.e. $\Delta p = 1\,\mathrm{bar}$ and $p^* = 0\,\mathrm{bar}$. The pressure distribution in a 24-channel tube with a 0.04 µm membrane is shown in Fig. 7.13. The peripheral channels still make a screening pressure around the inner channels but not as significant as in the substrate simulations. Channel 2 and 3 therefore become more efficient than before and now 87% of the total flow rate is delivered from channel 4 and 5 compared to the 98% in a pure substrate tube.

The permeate flow rate is found to be $Q_\mathrm{p} = 1.51\,\mathrm{m^3/h}$ which is about one fourth of the flow rate predicted from a 24-channel tube without a membrane. In the 0.04 µm membrane experiments the corresponding average permeate flow rate is $Q_\mathrm{p} = 2.2\,\mathrm{m^3/h}$, see Section 6.2.2. The simulations thus predict a lower flow rate, even though constant pressure is assumed in the channels. From the investigation of the membrane thicknesses on the monotubes and the 24-channel tubes, see Sections 6.1.3 and 6.2.3, we know that the membrane layer on the monotubes is approximately twice as thick compared to the 24-channel tubes, taking both the thickness of the 0.04 µm membrane and the 1 µm membrane into account. Thus, the membrane should have approximately half the thickness on a 24-channel tube in the simulations when using the estimated permeability. Conducting a simulation with a membrane thickness of 0.05 mm gives a flow rate of $Q_\mathrm{p} = 2.33\,\mathrm{m^3/h}$. Now the 2D simulation predicts a higher flow than the experiments as expected, though it is only slightly higher. The thinner membrane also decreases the efficiency of the inner channels and now 91% of the total flow rate is delivered from channel 4 and 5.

7.3.2 Equivalent circuit model

The EC model of the coated 24-channel tube is the same as the model for the substrate tubes described in Section 7.2.2 with only one addition. The 0.04 µm membrane layer is modeled as an extra resistance which is inserted in a serial connection with the existing substrate resistance from the channels. The membrane resistances are found in an iterative process in the same manner as the substrate resistances were found in Section 7.2.2, with the permeate flow rates from the COMSOL model including the membrane used as a benchmark.

The resulting pressure distribution in the channels along the length of the tube is shown in Fig. 7.14(a) using $\Delta p = 1\,\mathrm{bar}$ and $p^* = 0\,\mathrm{bar}$. The pressure distributions in the channels have the same tendencies as in the substrate simulations, see Fig. 7.10(a), but the total pressure drop is now 0.04 bar which is five times smaller than the pressure drop found in the substrate simulation. This lower pressure drop is due to a lower permeate flow and consequently lower channel flow rate caused by the added membrane resistance. Fig. 7.14(b) shows the permeate flow rate from the channels along the length of the tube. The majority of the permeate flow rate is still delivered from the peripheral channels.

The relation between permeate flow rate and transmembrane pressure is shown in Fig. 7.15 comparing simulations from the EC model and the COMSOL model with the experimental results, represented as the average power-law fit through all measuring points. Due to the lower flow rate compared to the substrate simulations the nonlinear effect induced by the hydraulic channel resistances is reduced, thus the COMSOL model and the EC model are almost equal. The EC model predicts a too low flow rate compared to the experiments due to the membrane thickness, just like the COMSOL model, and the relative error is $\varepsilon = 29\%$ at $p_{\mathrm{tm}} = 1\,\mathrm{bar}$. Therefore we have made a simulation with the EC model

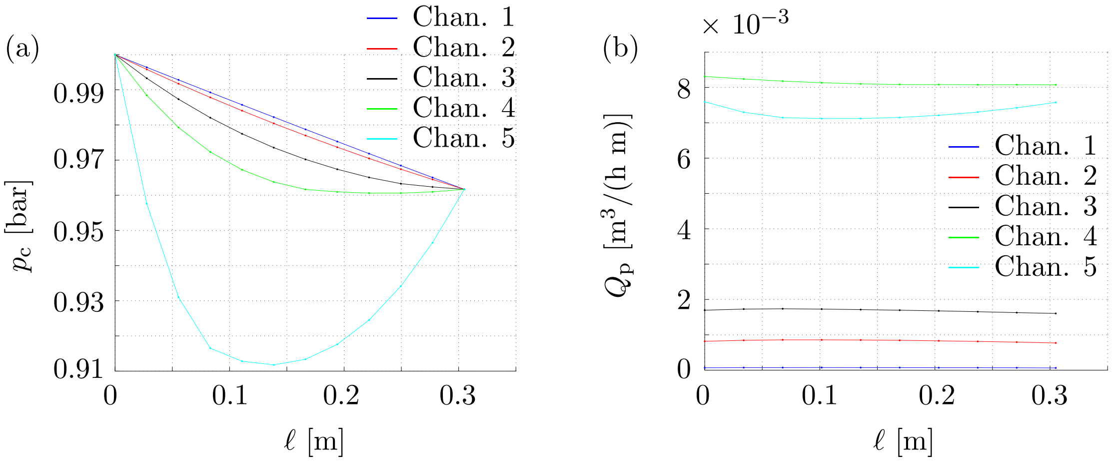

Figure 7.14: (a) Pressure p_c in the channels along the length ℓ of the channels. (b) Permeate flow rate from the five channels down the length of the tube. The peripheral channels deliver most of the total permeate flow, but the efficiency of channel 2 and 3 has increased slightly compared to the substrate simulations.

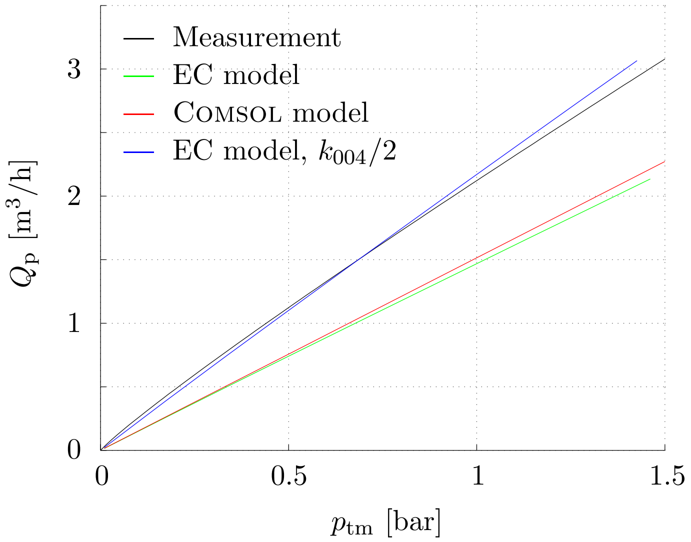

Figure 7.15: Comparison of the permeate flow rate found in the EC model and experiments with 24-channel tubes coated with the 0.04 µm membrane. The experiments are represented as the average power-law fit. The 2D COMSOL model is included as a reference. Both numerical simulations lie significantly lower than the experimental results due to a wrong membrane thickness in the simulations. A simulation is also conducted with the EC model using half the membrane thickness which agrees well with the experiments.

using half the membrane thickness also shown in Fig. 7.15. This simulation agrees very well with the experimental results with a relative error of only $\varepsilon = 3\%$ at $p_{\mathrm{tm}} = 1$ bar. Still the simulations are expected to lie even higher due to the lack of inlet and outlet BC's and inertia. Thus the membrane thickness should maybe be even thinner in the simulations. This is hard to determine, however, since the membrane thickness was so different between the monotubes and 24-channel tubes. Furthermore the quality of the 1 µm membrane was poor on the 24-channel tubes making it even more difficult to get the simulations and the experiments to agree.

Based on these considerations and the presented results we thus conclude that the EC model of a 24-channel tube describes the flow well. The deviations seen between the simulations and the experiments are expected to be mainly due to the quality and thickness of the membrane layers on the 24-channel tubes used in the experimental work.

7.4 Summary

We have developed two numerical models describing flow in porous SiC-tubes. Both models use the permeability for the SiC-substrate and the estimated permeability for the 0.04 µm membrane found in the monotube experiments. The first model is a simple 2D model made in COMSOL based on potential flow theory using the Laplace equation for the pressure and Darcy's law for the velocity in the porous SiC. The other model is a 3D equivalent circuit model based on the analogy between the Hagen-Poiseuille law and Ohm's law from electricity. This model includes the hydraulic resistance in the channels of the tubes due to wall friction, assuming smooth channels.

The 2D COMSOL model of the pure 24-channel substrate show that the peripheral channels make a screening pressure of the inner channel. This means that 98% of the permeate flow rate from a 24-channel tube is delivered by the peripheral channels in the substrate tubes while the peripheral channels deliver 87% of the flow rate in tubes coated with the 0.04 µm membrane. Thus the inner channels are almost redundant in the 24-channel tube.

We found that the EC model predict the pressure drop down the length of a 24-channel tube well compared to the measured pressure drop. Furthermore a significant pressure drop was found in the peripheral channels due to small hydraulic diameters and higher flow rates compared to the inner channels. This pressure drop decreases the efficiency of the tubes because the peripheral channels deliver the majority of the permeate flow. The EC model predicts a lower permeate flow rate than seen in the experiments with the 24-channel substrates with a maximum deviation of $\varepsilon = 14\%$. It was expected that the model predicted a higher flow rate since the channels are assumed smooth and inlet and outlet BC's and inertia are neglected. Also the COMSOL model predicts a lower flow rate than the experiments until $p_{\mathrm{tm}} = 0.3\,\mathrm{bar}$ which is unexpected as it is a linear model and thus uses the most optimal conditions. We suspect that this is due to the 24-channel tubes having a higher permeability than expected, which might be because they have been re-sintered, but this is unknown to us.

The simulations with 24-channel tubes coated with 0.04 µm membrane give a significantly lower flow rate than seen in the experiments with a relative error of $\varepsilon = 29\%$ at $p_{\mathrm{tm}} = 1\,\mathrm{bar}$. The lower flow rate is due to the assumption of equal thickness of the 0.04 µm membrane on the 24-channel tubes and on the monotubes. Investigations of the membrane have shown that it is only approximately half as thick on 24-channel tubes compared to monotubes and using half the thickness in the EC simulations give good agreement with the experiments.

Chapter 8

Geometrical optimization

The two numerical models presented in Chapter 7 will be used to optimize the geometry of the SiC focusing on increasing the permeate flow rate. The optimization process is done assuming clean, demineralized water, and therefore no considerations concerning the size of the membrane area (the surface area of the channels in the tubes) or contaminated fluid are made.

First, we make some simple optimization suggestions of a 24-channel tube based on the flow phenomena seen in Chapter 7. We will therefore focus on increasing the surface area in order to avoid screening of the inner channels and we will increase the size of the channels in order to decrease the pressure drop throughout the length of the tubes. The optimized geometries will be compared to the simulations of the original 24-channel tube and both the COMSOL model and the EC model will be used to estimate the flow rate delivered from these new design suggestions. Both substrate and 0.04 µm membrane simulations will be made but only the results will be presented.

Secondly, we compare the achieved results with data from a standard membrane used by CoMeTas, the so-called COM-144-865-(2*2)-0.04, using both experimental results for the original 24-channel tubes and the simulations of the best optimized geometry. Some suggestions on how to improve the large standard membrane used by CoMeTas are presented and the efficiency is compared to simulations of the original membrane.

We have decided that the new geometries should have a uniform wall thickness to minimize the risk of cracks appearing in the drying or sintering process. Furthermore, the ratio between wall thickness and channel dimensions is kept above 0.25 for the structure to be self-sustaining when extruded, [22]. We are thankful to Johnny Marcher, technical director at LiqTech, for good advice and technical discussions concerning limitations and possibilities of new designs.

8.1 Optimizing surface area

The results from the COMSOL simulations of a 24-channel tube with length $L = 305\,\mathrm{mm}$ are listed in Table 8.1 and these results will be used as comparison values for the optimization suggestions. Unless otherwise noted the following parameters will be used throughout

Table 8.1: (a) The permeate flow rate leaving the original 24-channel tube with $L = 305\,\text{mm}$ uncoated and coated with a $0.04\,\mu\text{m}$ membrane. (b) The surface and membrane areas of the tube.

(a)

	Q_p [m^3/h]
Substrate	6.51
0.04 µm membrane	1.51

(b)

	$\mathcal{A}$ [m^2]
Surface area	2.39×10^{-2}
Membrane area	1.08×10^{-1}

this chapter: $L = 305\,\text{mm}$, $d_\text{o} = 25\,\text{mm}$, $\Delta p = 1\,\text{bar}$, $p^* = 0\,\text{bar}$, $k_\text{s} = 8.3 \times 10^{-13}\,\text{m}^2$, $k_{004} = 1.8 \times 10^{-14}\,\text{m}^2$ and $w_{004} = 0.1\,\text{mm}$, where d_o is the outer diameter of the tubes and w_{004} is the thickness of the $0.04\,\mu\text{m}$ membrane.

In the original 24-channel tube the permeate flow rate is largely delivered by the peripheral channels because the inner channels are screened by the pressure in these channels, see Section 7.2.2. The efficiency of the 24-channel tube can then be increased by reducing the screening, which can be done by increasing the surface area. The simplest way to do this is by making a cut into the original geometry of the 24-channel tube, see Fig. 8.1 where the pressure distribution is shown for such a suggestion. Fig. 8.1(a) is the pressure distribution in a pure substrate while the substrate is coated with the $0.04\,\mu\text{m}$ membrane in Fig. 8.1(b). In this design the cut is one channel wide and three channels deep and all the walls still have a thickness of 1 mm. Some of the inner channels now contribute to the permeate flow rate in both simulations which can be seen from the pressure gradient. The permeate flow rate for both the substrate and the tube coated with a $0.04\,\mu\text{m}$ membrane has increased by 29%, see Fig. 8.1(c), compared to the original 24-channel tube. Thus a relatively simple change in the geometry leads to a significant increase in the permeate flow

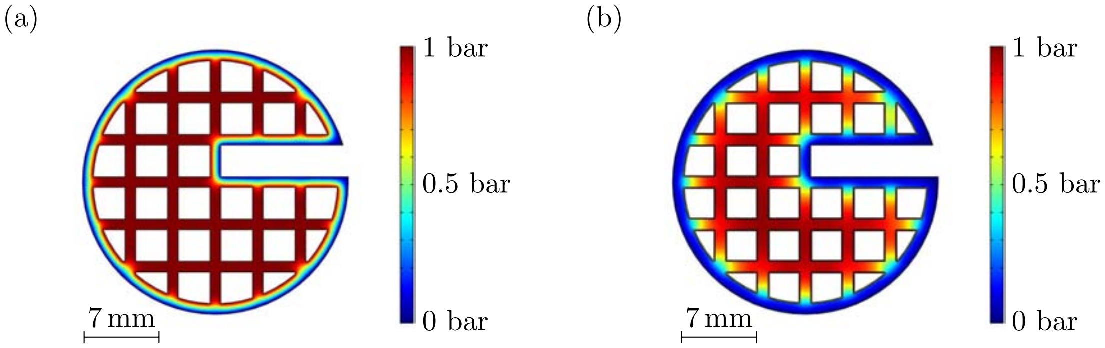

(c)

	Q_p [m^3/h]
Substrate	8.39
0.04 µm membrane	1.93

(d)

	$\mathcal{A}$ [m^2]
Surface area	3.11×10^{-2}
Membrane area	9.73×10^{-2}

Figure 8.1: Pressure distribution in a 24-channel tube with a cut which is three channels deep and one channel wide. The thickness of the walls is still $w = 1\,\text{mm}$ and the length is $L = 305\,\text{mm}$. (a) The pressure distribution in a substrate tube. (b) Tube coated with $0.04\,\mu\text{m}$ membrane. (c) The permeate flow rates for both simulations. (d) Surface and membrane areas of the new geometry.

rate. In Fig. 8.1(d) the surface and membrane areas are listed. The membrane area has decreased by 10% as the three channels are removed, while the surface area is increased by 30%. Thus the increase in surface area and the increase in permeate flow rate are almost equal.

When studying Fig. 8.1(a) and (b) it is seen that some of the channels are still inefficient and the permeate flow rate can therefore be increased even more. The surface area is now increased by removing three additional channels at the center of the 24-channel model with a cut. The resulting pressure distribution for the substrate and the 0.04 µm membrane are shown in Fig. 8.2(a) and (b), respectively. The permeate flow rate delivered is listed in Fig. 8.2(c) while the surface and membrane areas are shown in Fig. 8.2(d). This geometry has a 50% increase in surface area compared to the original 24-channel tube and a 49% higher permeate flow rate both the for uncoated and the coated tube. Once again a connection is then seen between the increase in surface area and increase in permeate flow rate. All the channels in the coated tube are now active and no channels are screened by a surrounding high pressure. Therefore it is difficult to optimize the 24-channel geometry more with this simple method.

From the two designs presented here it is obvious that significant increases in permeate flow rate can be achieved when the surface area is increased. Furthermore it is observed that the increased surface area seems to be proportional to the increase in permeate flow rate. We can conclude that the surface area is a crucial factor when optimizing the SiC-geometry regarding permeate flow rate.

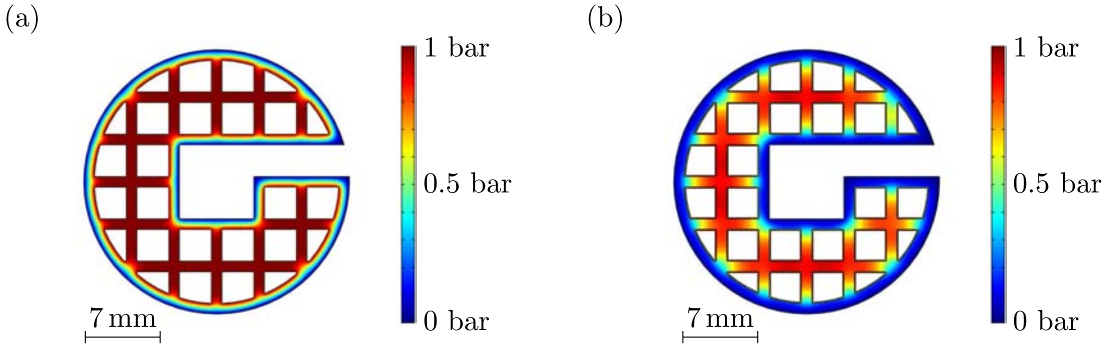

(c)

	Q_p [m^3/h]
Substrate	9.73
0.04 µm membrane	2.24

(d)

	$\mathcal{A}$ [m^2]
Surface area	3.60×10^{-2}
Membrane area	8.63×10^{-2}

Figure 8.2: Pressure distribution in improved 24-channel tube with six channels removed. (a) Substrate simulation. (b) Tube coated with a 0.04 µm membrane. (c) Permeate flow rate results. (d) Surface and membrane areas.

8.2 Optimizing channel dimensions

In the original 24-channel tube the peripheral channels have smaller hydraulic diameters compared to the inner channels. Since the peripheral channels deliver the majority of the permeate flow rate these channels should have a large hydraulic diameter to minimize the pressure drop down the length of the channels. However, we cannot just increase the size of the channels if the new designs shall be possible to extrude. The ratio between wall thickness w and the hydraulic diameter d_{h} of the channels should not be lower than $w/d_{\mathrm{h}} = 0.25$ for the structure to be self-sustaining when extruded, [22]. Since we want to keep the wall thickness small in order to have a high permeate flow rate this limits the size of the channels. For simplicity the wall thickness is kept constant at $w = 1\,\mathrm{mm}$ in the designs presented here.

A design is made with a new channel distribution and the resulting pressure distribution is seen in Fig. 8.3(a) and (b), for the substrate tube and the tube coated with a $0.04\,\mu\mathrm{m}$ membrane, respectively. The position of the channels has been changed so that they follow the geometry and hereby we avoid the small channels near the surface as seen in the 24-channel geometry. The permeate flow rates are listed in Fig. 8.3(c) while the surface and membrane areas are shown in Fig. 8.3(d). The hydraulic diameters of the channels are $d_{\mathrm{h}} = 3.0\,\mathrm{mm}$ in the inner channels, $d_{\mathrm{h}} = 3.8\,\mathrm{mm}$ in the second row of channels, and $d_{\mathrm{h}} = 3.5\,\mathrm{mm}$ in the peripheral channels. The size of the smallest channels is then comparable to the biggest channels in the original 24-channel tube. The wall thickness is $w = 1\,\mathrm{mm}$ and a total of 21 channels are present in this new design, thus naming it a 21-channel tube.

The surface area is identical to that of a 24-channel tube, but the membrane area is

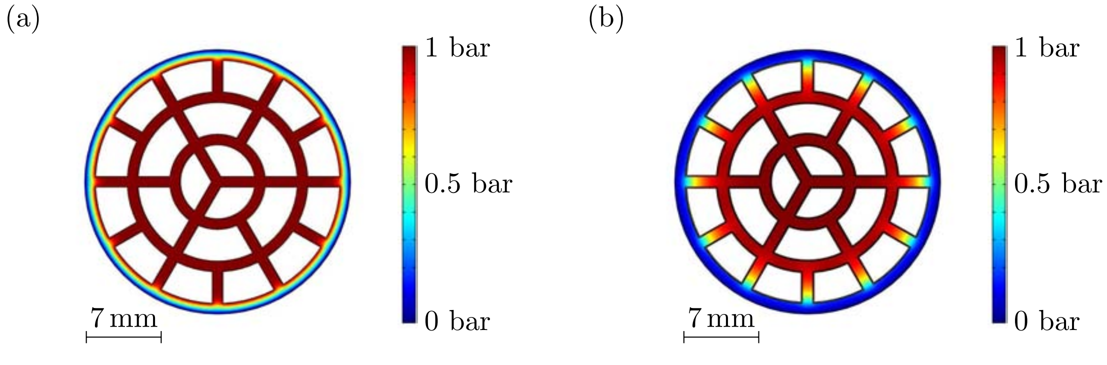

(c)

	Q_{p} [m^3/h]
Substrate	6.69
$0.04\,\mu\mathrm{m}$ membrane	1.41

(d)

	$\mathcal{A}$ [m^2]
Surface area	2.39×10^{-2}
Membrane area	9.49×10^{-2}

Figure 8.3: Pressure distribution in a new design named a 21-channel tube due to the 21 channels. (a) Substrate tube. (b) Coated with a $0.04\,\mu\mathrm{m}$ membrane. (c) Permeate flow rates for the two simulations. (d) Membrane and surface areas of the geometry.

12% smaller. Only a 3% increase in the permeate flow rate is seen for the substrate tube, and a decrease of 7% is observed for the tube coated with a 0.04 µm membrane. The decrease is seen as a consequence of the longer distance from the channels in the second row to the surface and therefore these channels are almost redundant in the 21-channel model.

To clarify the effect of different hydraulic diameters a so-called 60-channel tube is introduced. This tube is one of CoMeTas' standard tubes and build in the same way as the 24-channel tube, but with 60 channels having a size of only 2 mm × 2 mm. The wall thickness is $w = 0.8\,\mathrm{mm}$ and the outer diameter of the tube is $d_\mathrm{o} = 27\,\mathrm{mm}$. A 60-channel tube is thus only slightly larger than a 24-channel tube but contains more than twice as many channels. The pressure distribution in a 60-channel tube is comparable to that of a 24-channel tube and it is therefore not included here. The 60-channel tube is used as comparison to show the importance of the size of the channels.

EC models of the 21-channel and 60-channel tubes are made and the relation between flow rate and transmembrane pressure is shown in Fig. 8.4 together with the EC results for the original 24-channel tube. The dotted lines represent simulations from the 2D COMSOL model and these are included as a reference to see the influence of the hydraulic channel resistance. Simulations with substrates are shown in Fig. 8.4(a) and from these results it is clear that the size of the channels has a significant influence when the permeate flow rate is high. The 60-channel tube has the highest flow rate in the COMSOL simulations, but because of the small channels this tube has the lowest permeate flow at $p_\mathrm{tm} = 1\,\mathrm{bar}$. The 21-channel tube has the lowest reduction in flow rate compared to its COMSOL simulation and it is clearly the most efficient of the three tubes. From these results it is obvious that the hydraulic diameter of the channels should be taken into account when tubes are uncoated.

The results from the simulations with a 0.04 µm membrane added are shown in Fig. 8.4(b).

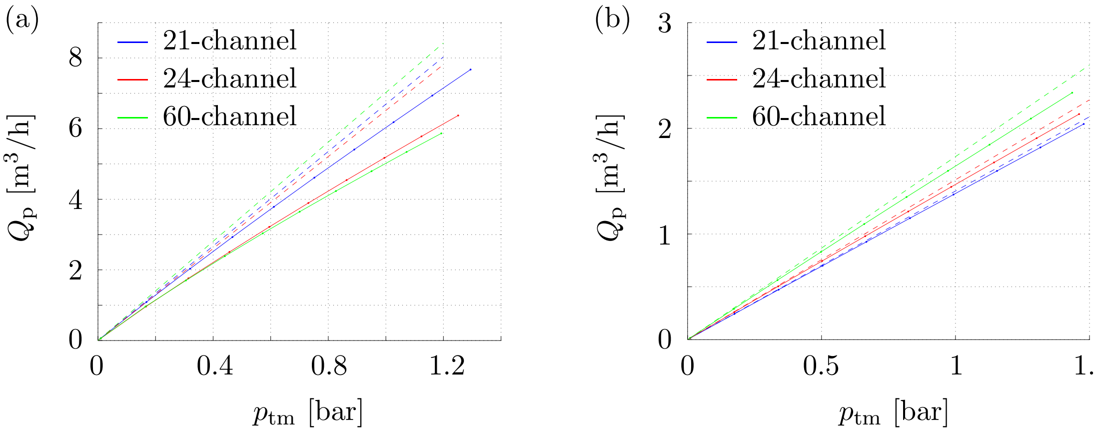

Figure 8.4: Q_p as a function of p_tm for three tubes simulated in the EC model. The hydraulic diameter of the channels is different in the three tubes leading to different hydraulic channel resistances. The dotted lines are simulations from the COMSOL model included as a reference. (a) Substrates. (b) Tubes with a 0.04 µm membrane.

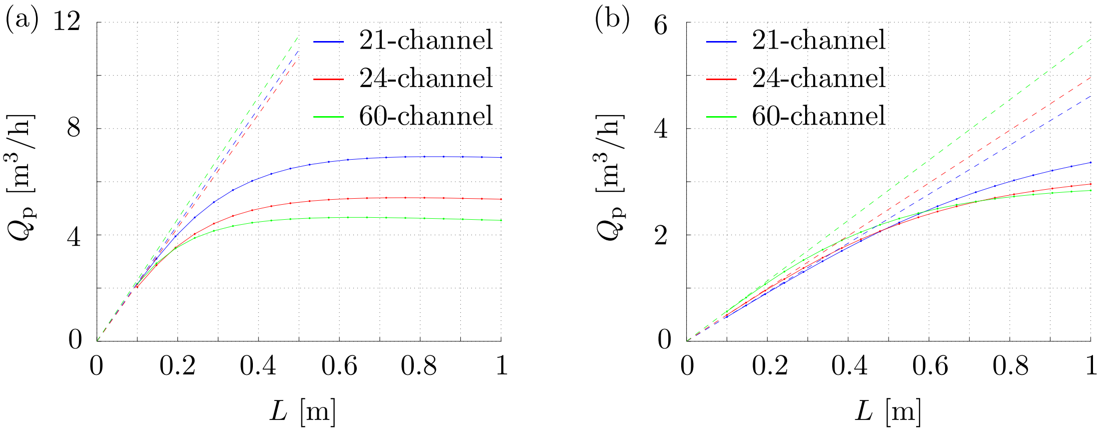

Figure 8.5: Permeate flow rate Q_p versus tube length L for the three tubes. The size of the channels is different in the three tubes leading to different hydraulic channel resistances. The dotted lines are COMSOL simulations included as a reference. (a) Substrates. (b) Tubes with the 0.04 µm membrane added.

The flow rates are lower compared to the substrate simulations due to the added membrane and the influence of the channel sizes has thus decreased significantly. The 60-channel tube now has the highest flow rate in the EC model while the 21-channel tube has the lowest. From these two figures we can see that the hydraulic resistance is very important in the substrate tubes, but when a membrane is added the resistance is of less importance even in the small channels of the 60-channel tube.

Besides flow rate and channel size the resistance is also influenced by the length of the tubes. The permeate flow rate at different tube lengths is plotted in Fig. 8.5(a) for the substrate tubes while the same is shown for the tubes coated with 0.04 µm membrane in Fig. 8.5(b). COMSOL simulations are as before included as a reference. All the simulations are made with $\Delta p = 1$ bar at the inlet of the tubes and the transmembrane pressure then changes as the tubes are made longer. Fig. 8.5 thus cannot be compared directly with Fig. 8.4. For all the substrate tubes the flow rate reaches a maximum at a tube length of approximately $L = 0.5$ m and further increase in the permeate flow rate cannot be achieved beyond this length at a constant inlet pressure. The 21-channel tube is clearly the most efficient, while the 60-channel tube delivers the least permeate flow rate as a consequence of the small channels.

Fig. 8.5(b) shows that even with the 0.04 µm membrane added the hydraulic resistance becomes important when the tube length is increased. At small lengths until approximately $L = 0.3$ m the resistance is unimportant, but at larger lengths the flow rates start to decrease compared to the COMSOL models. At $L = 0.6$ m the 21-channel tube becomes the most efficient while the 60-channel tube becomes the least efficient.

This study proves that the channel size has a great impact on the flow rate and therefore is an essential factor when designing a new tube. The present simulations have been conducted in a dead-end flow and influence of the hydraulic resistance would become even higher if the simulations were conducted in a cross-flow setup.

8.3 Proposal for a new design

With the results achieved in Sections 8.1 and 8.2 a proposal for an optimized design is developed with 18 channels naming it the 18-channel tube, see Fig. 8.6. The design has a large surface area with a 44% increase compared to the original 24-channel tube, and the hydraulic diameter of the channels is between $d_\mathrm{h} = 3.3\,\mathrm{mm}$ and $d_\mathrm{h} = 3.7\,\mathrm{mm}$. The cut is 3 mm wide and the center hole has a diameter of 7 mm. The pressure distribution found in the COMSOL model for a substrate tube and a tube with the 0.04 µm membrane added is seen in Fig. 8.6(a) and (b), respectively. The permeate flow rate is given in Fig. 8.6(c) while the surface and membrane areas are listed in Fig. 8.6(d). An increase of 46% is seen for the flow rate from the substrate tube compared to the original 24-channel tube, whereas the coated tube delivers a 34% higher flow rate. This tube is then not as efficient in the COMSOL simulations as the best optimized 24-channel geometry shown in Fig. 8.2. In the substrate simulations the optimized 24-channel tube has a 2% higher flow rate while it is 10% higher when the membrane is added. As seen in Section 8.2 the channel resistance has a significant impact on the flow rate for the substrate and the 18-channel tube will be the most efficient when this is taken into account. With the membrane added the two proposals would probably be almost equal when the tubes have a length of $L = 305\,\mathrm{mm}$ while the 18-channel tube will be the most efficient if the tubes have a length of $L = 1\,\mathrm{m}$. An EC model has not been created of the optimized 24-channel geometry, and this can therefore not be investigated.

An EC model of the 18-channel tube is made in order to determine the total im-

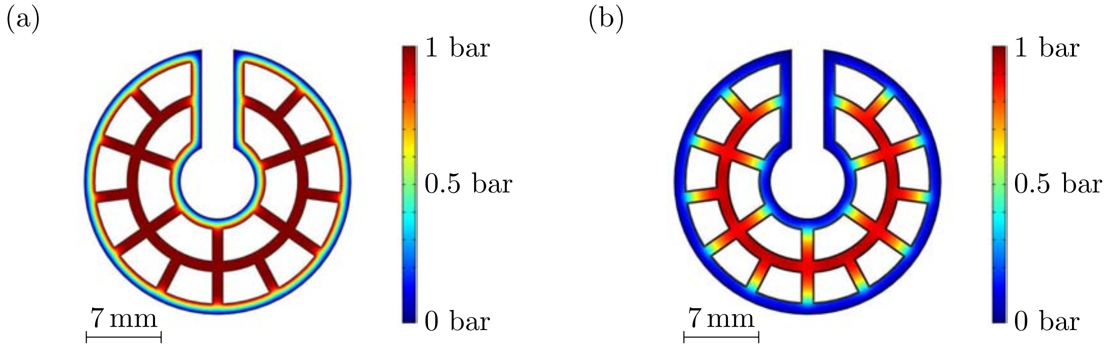

(c)

	Q_p [m^3/h]
Substrate	9.54
0.04 µm membrane	2.03

(d)

	$\mathcal{A}$ [m^2]
Surface area	3.45×10^{-2}
Membrane area	7.87×10^{-2}

Figure 8.6: Pressure distribution in a new design, the 18-channel tube, with bigger channels and a cut into a center hole. This new geometry has an increase in surface area of 44% compared to the original 24-channel tube and the hydraulic diameter of the channels is between $d_\mathrm{h} = 3.3\,\mathrm{mm}$ and $d_\mathrm{h} = 3.7\,\mathrm{mm}$. (a) Substrate. (b) Coated with the 0.04 µm membrane. (c) Permeate flow rate results. (d) Surface and membrane areas.

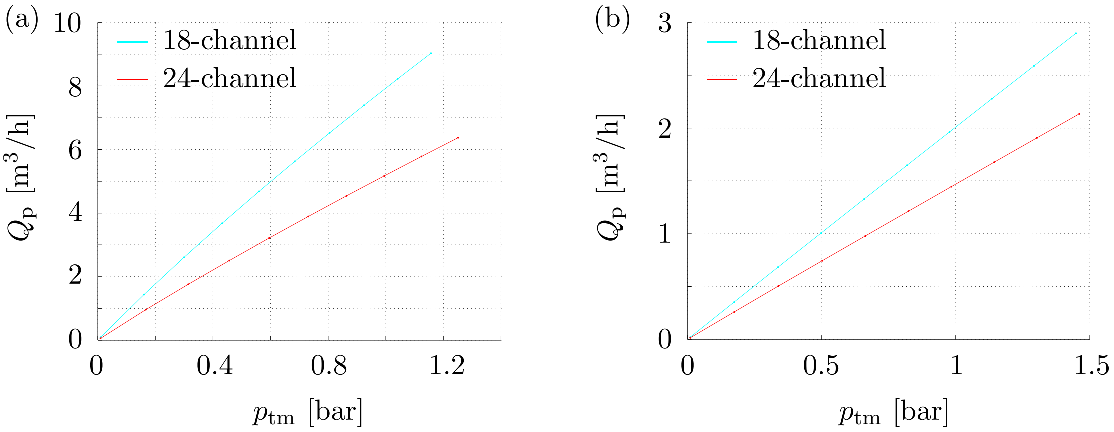

Figure 8.7: Comparison of the 18-channel tube and the original 24-channel tube. (a) Substrates. (b) Coated with the 0.04 µm membrane. A significant increase in permeate flow rate is seen for both the coated and the uncoated 18-channel tube compared to the original 24-channel tube.

provement compared to the original 24-channel tube. In Fig. 8.7(a) and (b) the permeate flow rates at different transmembrane pressure are shown for the substrate tubes and the tubes coated with a 0.04 µm membrane, respectively. At a transmembrane pressure of $p_\mathrm{tm} = 1\,\mathrm{bar}$ the substrate 18-channel tube has an improved permeate flow rate of 53% compared to the 24-channel tube, and if the tubes are coated an increase of 37% is seen. Comparing the results from the EC model to the results from the COMSOL model, show that the majority of the increased permeate flow rate is obtained from an increased surface area.

Another new design, a hexagonal tube, is presented in Appendix D. The hexagonal tube is smaller than the 18-channel tube with a side length of only 10 mm and thus has a lower permeate flow rate. In a hexagonal design, however, it is possible to have a lower ratio between wall thickness and channel size, [22]. The hydraulic diameter is more than $d_\mathrm{h} = 4.5\,\mathrm{mm}$ in the channels of the hexagonal design, which is significantly larger than the biggest channels in the 18-channel design having a maximum hydraulic diameter of $d_\mathrm{h} = 3.7\,\mathrm{mm}$. If long tubes are needed the hexagonal tubes might therefore be preferable to the 18-channel tube due to the lower hydraulic resistance. Furthermore, the hexagonal design presented in Appendix D can be optimized if the surface area is increased.

8.4 Improvements and comparison of large tubes

One of CoMeTas' large membranes, the so-called COM-144-865-(2*2)-0.04, has an outer diameter of $d_\mathrm{o} = 144\,\mathrm{mm}$, a length of $L = 865\,\mathrm{mm}$, contains around 1900 quadrilateral channels with a size of $2\,\mathrm{mm} \times 2\,\mathrm{mm}$, a wall thickness of $w = 0.8\,\mathrm{mm}$, and it is coated with the 0.04 µm membrane. The COM-144-865-(2*2)-0.04 thus is a larger version of the 60-channel tube. It has a permeate flow rate of $1000\,\mathrm{l/(m^2\ h\ bar)}$, which is flow rate in liters per membrane area in m^2 per hour per transmembrane pressure in bar, see Appendix E. The membrane area is $\mathcal{A} = 14.7\,\mathrm{m}^2$ and by multiplying with this value and assuming a transmembrane pressure of $p_{\text{tm}} = 1\,\text{bar}$ the permeate flow rate becomes $Q_{\text{p}} = 14.7\,\text{m}^3/\text{h}$.

8.4.1 Parallel connected tubes

Results from the experiments with the original 24-channel tubes coated with a $0.04\,\mu\text{m}$ membrane, see Section 6.2.2, are compared to the permeate flow rate from the COM-144-865-(2*2)-0.04. At $p_{\text{tm}} = 1\,\text{bar}$ an average permeate flow rate of $Q_{\text{p}} = 2.2\,\text{m}^3/\text{h}$ was found in the experiments, therefore only seven original 24-channel tubes would deliver approximately the same permeate flow rate as a COM-144-865-(2*2)-0.04. Furthermore the COM-144-865-(2*2)-0.04 is nearly three times longer than the 24-channel tubes. From this simple comparison we can see that improvements should be attainable in the large membranes.

It is investigated how large an increase can be achieved by making a module of parallel connected 24-channel tubes. The module has a diameter equal to that of COM-144-865-(2*2)-0.04 and is sketched in Fig. 8.8. It can contain 19 original 24-channel tubes when the gab between two 24-channel tubes is at least 3 mm. The investigations presented here are very idealized as we do not consider how the modules would be made in practice but just assume that is possible. Dead-end results are used and we do not take into account that normally cross-flow is used in a filtering process, which might change the comparison values. Furthermore, we assume that all the tubes have the same permeate flow rate, i.e. no screening of the inner tubes is considered.

The overall permeate flow rate from the module containing 19 original 24-channel tubes is $Q_{\text{p}} = 41.8\,\text{m}^3/\text{h}$, which is an increase of 180% compared to the COM-144-865-(2*2)-0.04. Since the COM-144-865-(2*2)-0.04 is almost three times longer than the 24-channel tubes three modules correspond to one COM-144-865-(2*2)-0.04. A total permeate flow rate delivered from three modules in a parallel coupling is $Q_{\text{p}} = 125\,\text{m}^3/\text{h}$, which is an

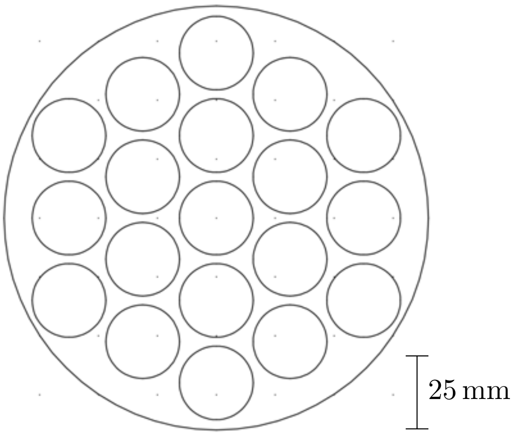

Figure 8.8: Sketch of a module containing 19 original 24-channel tubes. The diameter of the module is $d_{\text{o}} = 144\,\text{mm}$, just as the diameter of the COM-144-865-(2*2)-0.04. The diameter of the 24-channel tubes is $d_{\text{o}} = 25\,\text{mm}$. The gab between two 24-channel tubes is at least 3 mm.

increase of 750%. This is only a loose comparison, but it shows that significant increases in the permeate flow rate can be achieved by parallel coupling small tubes compared to large standard tubes.

In Section 8.3 a new geometry, the 18-channel tube, was introduced and the EC simulations showed that an increase of approximately 37% could be achieved in the permeate flow rate with coated tubes compared to the EC simulations of the original 24-channel tube. Using the 18-channel tubes with a length of $L = 305\,\text{mm}$ in a module would result in a permeate flow rate of $Q_p = 38.6\,\text{m}^3/\text{h}$, which is an increase of 160% compared to the COM-144-865-(2*2)-0.04. This a bit smaller than the flow rate from the module of original 24-channel tubes which is because the measured flow rates found in the experiments are used in that module. In the simulations we assume that the membrane thickness on the tubes is equal to that on the monotubes, and therefore the predicted flow rate from the 18-channel tubes is lower than the measured flow rate from the original 24-channel tubes. In practice a module of 18-channel tubes might have an even higher flow rate than predicted in these simulations.

If the hexagonal tubes with a length of $L = 305\,\text{mm}$ are used 37 tubes can fit inside a module, still with a gab of minimum 3 mm, see Appendix D. The permeate flow rate from such a module would be $Q_p = 40.3\,\text{m}^3/\text{h}$ and thus approximately the same as from a module of 18-channel tubes. The channels in the hexagonal tubes are very large with a hydraulic diameter of more than $d_\text{h} = 4.5\,\text{mm}$, whereas the 18-channel tube has a maximum hydraulic diameter in the channels of $d_\text{h} = 3.7\,\text{mm}$. If long tubes are needed the hexagonal tubes would then be the preferable choice due to the low hydraulic resistance in the channels.

8.4.2 New design of a COM-144-865-(2*2)-0.04

The geometries presented in this section have only been implemented in the COMSOL model as it would demand too much time to implement them in our EC model.

A COMSOL simulation of one eighth of a COM-144-865-(2*2)-0.04 is made and the pressure distributions as well as the permeate flow rate results are shown in Fig. 8.9. The screening of the inner channels is obvious in this large tube making the majority of the channels inefficient, even when the 0.04 µm membrane is added. The flow rate found in the 2D COMSOL model of the COM-144-865-(2*2)-0.04 with the membrane added is $Q_\text{p} = 30.0\,\text{m}^3/\text{h}$ when it has a length of $L = 865\,\text{mm}$. The calculated flow rate is then twice the flow rate stated by CoMeTas. Fig. 8.5(b) show that the EC model of the 60-channel tube, which is a smaller version of the COM-144-865-(2*2)-0.04, predicts roughly half the permeate flow rate compared to the COMSOL model at a length of $L \approx 850\,\text{mm}$ and this is assumed to be the same for the COM-144-865-(2*2)-0.04. It therefore seems likely that the COMSOL model predicts twice the flow rate.

12 cuts are made into the original geometry in order to reduce the screening of the inner channels. The geometry with the pressure distribution and the results from the simulations in COMSOL are shown in Fig. 8.10. The 12 cuts have a width of 4.8 mm and two rows of channels have then been removed in each of the cuts. The increase in both the surface area and the permeate flow rate is 280% compared to COMSOL simulations of the

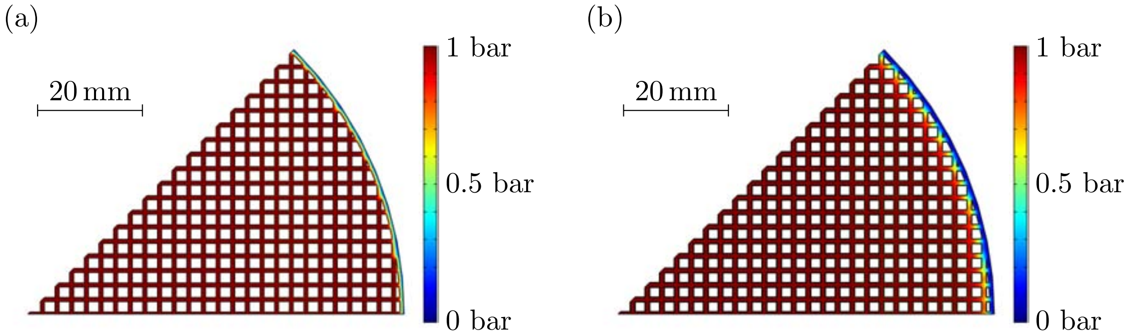

(c)

	Q_p [m^3/h]
Substrate	130
0.04 µm membrane	30.0

(d)

	$\mathcal{A}$ [m^2]
Surface area	0.39
Membrane area	14.3

Figure 8.9: Pressure distribution in a COM-144-865-(2*2)-0.04 with a diameter and length of $d_o = 144$ mm and $L = 865$ mm, respectively. The tube is a larger version of the 60-channel tube and therefore has wall thickness of $w = 0.8$ mm and the size of the channels is 2 mm × 2 mm. (a) Substrate. (b) Coated with a 0.04 µm membrane. (c) Permeate flow rate results. (d) Surface and membrane areas.

original geometry. This is a higher increase than seen with a module of parallel connected tubes, but this large tube is nearly three times longer than the small tubes. Using three modules of parallel connected small tubes would therefore be better. However, it might

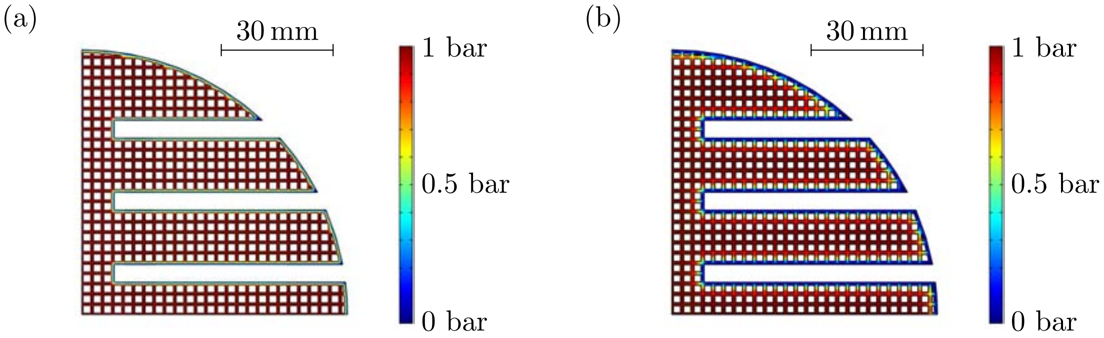

(c)

	Q_p [m^3/h]
Substrate	519
0.04 µm membrane	113

(d)

	$\mathcal{A}$ [m^2]
Surface area	1.50
Membrane area	11.1

Figure 8.10: The pressure distribution of the COM-144-865-(2*2)-0.04 with 12 cuts. The cuts are 4.8 mm wide, thus two rows of channels disappear, and the depth varies between the cuts. (a) Pure substrate. (b) Coated with a 0.04 µm membrane. (c) Permeate flow rate results. (d) Surface and membrane areas.

(a)

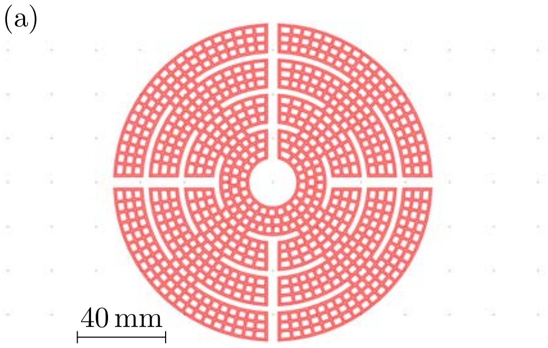

(b)

	$\mathcal{A}$ [m^2]
Surface area	1.73
Membrane area	7.65

Figure 8.11: (a) Design of a large tube with an outer diameter of $d_\mathrm{o} = 144\,\mathrm{mm}$, a length of $L = 865\,\mathrm{mm}$, and a wall thickness of $w = 1\,\mathrm{mm}$. The hydraulic diameters of the channels are more than 3 mm and the channels are of approximately the same size. (b) Surface and membrane areas.

be easier to implement the cuts in the original geometry compared to making the modules of the parallel connected tubes.

Using the investigations and designs presented in the previous sections of this chapter as inspiration, we create a new design of a large membrane with an outer diameter of $d_\mathrm{o} = 144\,\mathrm{mm}$ and a length of $L = 865\,\mathrm{mm}$, see Fig. 8.11(a). The membrane and surface areas of the new design are listed in Fig. 8.11(b). The design is made with the focus on creating a large surface area as well as having channels with hydraulic diameters at or above 3 mm and still approximately of the same size. The position of the channels has been

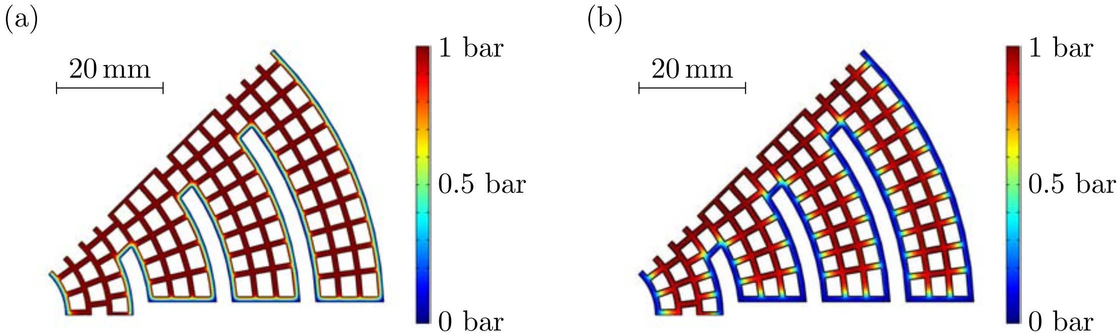

(c)

	Q_p [m^3/h]
Substrate	487
0.04 µm membrane	112

Figure 8.12: Pressure distribution in a new design suggestion of a large membrane with an outer diameter of $d_\mathrm{o} = 144\,\mathrm{mm}$, a length of $L = 865\,\mathrm{mm}$, and a wall thickness of $w = 1\,\mathrm{mm}$. Only one eighth is modeled in order to get a properly meshed structure, which results in a slightly different geometry than seen in Fig. 8.11. For convenience this small change is neglected. Surface and membrane areas are given in Fig. 8.11. (a) Substrate. (b) Coated with a 0.04 µm membrane. (c) Permeate flow rate results.

changed so that they follow the geometry and hereby we avoid the small channels near the surface as seen in the original geometries. The walls have a thickness of $w = 1\,\mathrm{mm}$ and it is assumed that the structure is self-sustaining during a fabrication process. It should be noted that the four main cuts in the structure would be cut subsequently to the sintering process while the small cuts within the structure are possible to extrude. The present geometry might not be possible to make in practice, but the general idea of the geometry can be used to make a new design of a large membrane.

Because of the complex geometry and the limited number of elements available in COMSOL, only one eighth of the structure is simulated in order to obtain a properly meshed geometry. This results in a slightly different structure than the one shown in Fig. 8.11 as the cut into the center hole is omitted. For convenience it is assumed that the two structures have the same permeate flow rate. The pressure distribution for a substrate and a tube coated with a $0.04\,\mu\mathrm{m}$ membrane are shown in Fig. 8.12 together with results for the flow rate. The permeate flow rate delivered from this new design with a length of $L = 865\,\mathrm{mm}$ is $Q_\mathrm{p} = 487\,\mathrm{m}^3/\mathrm{h}$ which is a bit lower than found for the design with 12 cuts. However, if the hydraulic resistance in the channels is taken into account the new design will undoubtedly be better. This can be seen from the investigation of the importance of the channel sizes in the tubes presented in Section 8.2. With a $0.04\,\mu\mathrm{m}$ membrane added the flow rate becomes $Q_\mathrm{p} = 112\,\mathrm{m}^3/\mathrm{h}$ in the new design which is the same as found for the design with the 12 cuts. Again, the new design is the most efficient when the hydraulic channel resistance is included.

The results presented here can be used to get an impression of the possibilities when making new designs. Significant increases are found both when using parallel connected small tubes in modules and when changing the geometry of the large COM-144-865-(2*2)-0.04.

8.5 Summary

The screening of the inner channels of the tubes observed in Chapter 7 can be reduced by increasing the surface area of the tubes. The results from the 2D COMSOL model show that the increase in surface area is comparable to the increase in permeate flow rate, both for substrates and coated tubes, and significant flow rate increases are obtained.

The hydraulic resistance in the channels depends on channel size, tube length and channel flow rate. In the original design the peripheral channels, having the highest flow rates, are the smallest and therefore significant pressure drops were observed in these channels in Chapter 7. The resistance is minimized by making a new design with larger channels that follow the geometry of the tubes and it is also seen that the tubes should not be longer than $L \approx 500\,\mathrm{mm}$ to minimize the pressure drop in the channels.

Proposals of new designs are presented with an increase of both channel size and surface area. In these proposals no considerations concerning the size of the membrane area or the degree of contamination of the fluid are made. A 53% increase in permeate flow rate is seen in the EC simulations of the substrate 18-channel tube compared to the EC simulations of the original 24-channel tube, while the increase is 37% when the tubes are coated with a 0.04 μm membrane. The new design for the COM-144-865-(2*2)-0.04 tube increases the permeate flow rate by 270% for both the uncoated and coated tube comparing to the original COM-144-865-(2*2)-0.04 in the Comsol model and the increase might be even larger when including the hydraulic channel resistance.

Idealized modules with the same diameter as the COM-144-865-(2*2)-0.04 are made containing parallel connected tubes, and a module can contain 19 18-channel tubes. When these tubes have a length of $L = 305\,\mathrm{mm}$, the permeate flow rate from such a module is approximately 160% higher compared to data for the original COM-144-865-(2*2)-0.04, even though the COM-144-865-(2*2)-0.04 is almost three times longer. This is only a loose comparison, but it shows that significant increases can be achieved by parallel coupling small tubes.

The new designs presented in this chapter show that higher flow rates are easily attainable and the efficiency of the tubes can be increased significantly.

Chapter 9

Conclusion and outlook

9.1 Conclusion

The work presented in this thesis can be categorized into experimental and numerical work. The experimental work includes fabrication and flow measurements of various SiC-samples, while the numerical work includes validation of the two numerical models with the experimental results and geometry optimization of the tubes regarding the permeating flow. Only water is used in the experiments during this thesis and the filtration process itself is not investigated.

Experiments with plugs and monotubes show a linear relation between permeate flow rate and transmembrane pressure and we conclude that Darcy's law is valid in porous SiC. The experiments with thin-walled and thick-walled monotubes show that the permeability is independent of the SiC thickness and it is found to be $k = (8.3 \pm 0.7) \times 10^{-13}\,\mathrm{m}^2$ for the substrate. For 24-channel tubes the relation between permeate flow rate and transmembrane pressure is nonlinear. We find this to be due to a large hydraulic resistance in the channels of the tubes giving rise to a significant pressure drop down the length of the 24-channel tubes.

Simulations show that the peripheral channels screen the inner channels in the 24-channel tubes even when the tubes are coated with membranes and the efficiency of the tubes is therefore low. We have made different suggestions for optimized geometries regarding the permeate flow rate focusing on three parameters, the length of the tubes, the size of the channels and the surface area. Different suggestions are compared to an existing membrane geometry used by CoMeTas and significant increases in the permeate flow rate are obtained. Making simple cuts in the surface of the tubes to increase the surface area can increase the permeate flow rate by roughly 50% in 24-channel tubes and more than 250% in large membranes. More advanced optimization suggestions with modules consisting of many small tubes in parallel connection might increase the permeate flow rate even more compared to the existing large membrane.

Thin-walled monotubes and 24-channel tubes are coated with two different membrane layers, a $0.1\,\mu\mathrm{m}$ membrane and a $0.04\,\mu\mathrm{m}$ membrane. It is expected that tubes coated with the $0.04\,\mu\mathrm{m}$ membrane has the lowest flow rate, but it is found to be only slightly lower than the flow rate in tubes coated with the 0.1 µm membrane. This is seen both for monotubes and 24-channel tubes. An investigation of the membrane thicknesses with a microscope show that the 0.04 µm membrane layer is thinner than the 0.1 µm membrane layer in average and we conclude that this is the reason for the equal flow rates. The investigation also shows that the membrane layers are significantly thinner on 24-channel tubes compared to monotubes.

Simulations of the substrate 24-channel tubes show that the 2D Comsol model overshoots the experimental results at high flow rates due to lacking channel resistance in the model. The 3D equivalent circuit model agrees well with experiments predicting a slightly lower flow rate than measured. Simulations of 24-channel tubes coated with 0.04 µm membrane predict a significantly lower flow rate than measured in the experiments. On the basis of the measured membrane thicknesses we argue that the membrane layer is approximately only half the thickness on 24-channel tubes compared to monotubes and using this in the simulations gives very good agreement between simulations and experimental results. We conclude that the two numerical models predict the flow in the porous SiC well.

9.2 Outlook

Our simulations of the geometrical optimized proposals show that it is easy to retrieve large increases in the permeate flow rate by making relatively small and simple changes in the membrane geometries. An obvious point of departure for future work would therefore be to perform experimental work on SiC-tubes with these simple changes. The experimental

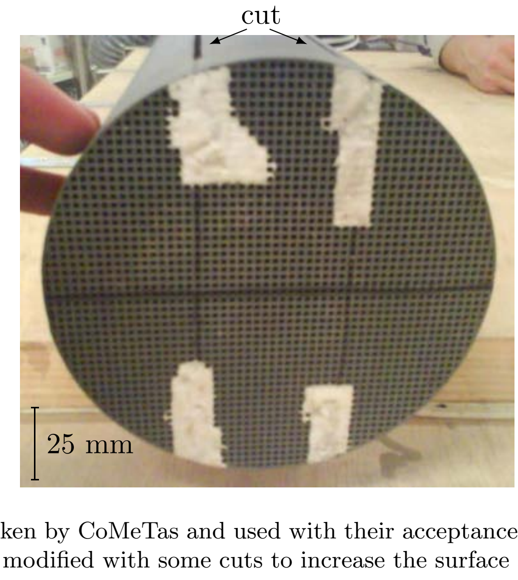

Figure 9.1: The picture is taken by CoMeTas and used with their acceptance. The geometry of the COM-144-865-(2*2)-0.04 has been modified with some cuts to increase the surface area and it has been used for preliminary experiments by CoMeTas. Four cuts with a length of 20 cm are made in each end giving a total of eight cuts. The permeate flow rate is increased by approximately 30% compared to a standard COM-144-865-(2*2)-0.04.

work could also be extended to include some of the more complicated geometries we have suggested, but this will of course encompass development and fabrication of the geometries in question.

To be able to simulate the flow in the SiC-tubes better it would be beneficial to extend the numerical model to include inlet and outlet effects on the tubes, a transition zone from laminar to turbulent flow in the channels, and inertia forces in the equations. In order to look at the filtering process in the tubes, a new numerical model could also be developed that includes particulate material in the flow. This way it would be possible to investigate the dynamic filter cake on the surface of the membrane and it will be possible to check how this influences an optimization of the membrane geometry.

It would be very interesting to use topology optimization when looking at the optimization process of the membrane geometry. This method would make it easier and faster to retrieve suggestions which could result in very efficient membranes and indicate some tendencies which could be used when designing new membranes.

CoMeTas has conducted a few preliminary experiments with a membrane using one of the simple design proposal we have presented. They have increased the surface area of their COM-144-865-(2*2)-0.04 by making eight cuts with an angle grinder, see Fig. 9.1. The cuts increase the permeate flow rate by approximately 30% compared to the flow rate from a standard COM-144-865-(2*2)-0.04. These preliminary experiments demonstrate that significant increases in the permeate flow rate can be obtained. Furthermore the experiments verify that focusing on increasing the surface area is important when optimizing the membranes.

Appendix A

Characterization methods

The simple methods that can be used to characterize the porous SiC by its porosity and pore size are shortly presented in the following.

A.1 Porosity

The porosity of the SiC used in our plugs and tubes, can be found from a simple experiment with the thin-walled and thick-walled monotubes. The mass m_d of the dry monotubes is measured, and then the monotubes are immersed in demineralized water until they are completely saturated with water. Afterwards, the mass m_s of the now saturated monotubes is measured. The volume $\mathcal{V}_\mathrm{SiC}$ of the SiC in the monotubes is found as

$$\mathcal{V}_\mathrm{SiC} = \pi L\Big(\frac{d_\mathrm{o}^2}{4} - \frac{d_\mathrm{c}^2}{4}\Big), \tag{A.1}$$

where L is the length, d_o is the outer diameter, and d_c is the channel diameter of the monotubes. The volume $\mathcal{V}_\mathrm{w}$ of the absorbed water can be estimated by subtracting the mass of the dry monotubes from the mass of the saturated monotubes and dividing by the density $\rho = 1000\,\mathrm{kg/m^3}$ of the water,

$$\mathcal{V}_\mathrm{w} = \frac{m_\mathrm{s} - m_\mathrm{d}}{\rho}. \tag{A.2}$$

Hereafter the porosity ϕ_SiC of the SiC is calculated from the relation between Eqs. (A.1) and (A.2),

$$\phi_\mathrm{SiC} = \frac{\mathcal{V}_\mathrm{w}}{\mathcal{V}_\mathrm{SiC}}. \tag{A.3}$$

We used ten thin-walled and eight thick-walled monotubes for this porosity experiment. All of them had a length of $L = 305\,\mathrm{mm}$ and an outer diameter of $d_\mathrm{o} = 21.3\,\mathrm{mm}$, while the channel diameter was $d_\mathrm{c} = 16.9\,\mathrm{mm}$ for the thin-walled monotubes and $d_\mathrm{c} = 14.1\,\mathrm{mm}$ for the thick-walled monotubes. The mean porosity, in %, of the SiC was found to be

$$\phi_\mathrm{SiC} = (38.2 \pm 0.8)\%, \tag{A.4}$$

where the error is the standard deviation of the porosities found from each of the monotubes. A porosity of approximately 40% was expected for the SiC, and our results agree well with these expectations. The porosity varied up to 3% from one monotube to another. This was both because of slight uncertainties in the experiment itself, but mostly because the monotubes are relatively small samples of SiC, and therefore small deviations in the porosity are expected.

A.2 Capillary rise

One way to determine the average pore size in a porous medium, is by use of the capillary rise height. If one end of a piece of SiC is immersed in a bowl of water, the water will be absorbed and rise through the pores in the SiC due to capillary forces, see Fig. A.1. These capillary forces occur due to the Young-Laplace pressure drop Δp_{surf} over the water/air interface, as described in section 7.3 in [1].

In order to simplify the problem, it is assumed that the pores are straight, cylindrical channels in the SiC. The air has the standard atmospheric pressure p_0 while the pressure just below the water/air interface is $p_0 - \Delta p_{\text{surf}}$. When the water column reaches its equilibrium height H, the Young-Laplace pressure drop will be equal to the hydrostatic pressure generated by the water column. The mean pore diameter d_{m} can then be found by rearranging Eq. (7.21), pp. 129, in [1],

$$d_{\text{m}} = \frac{4\gamma}{\rho g H} \cos\theta, \tag{A.5}$$

where $\gamma = 72.9\,\text{mJ/m}^2$ is the surface tension at the water/air interface, $\rho = 1000\,\text{kg/m}^3$ is the mass density of the water, $g = 9.81\,\text{m/s}^2$ is the gravitational acceleration and θ is the contact angle at the water-SiC-air contact line. Unfortunately we were unable to retrieve

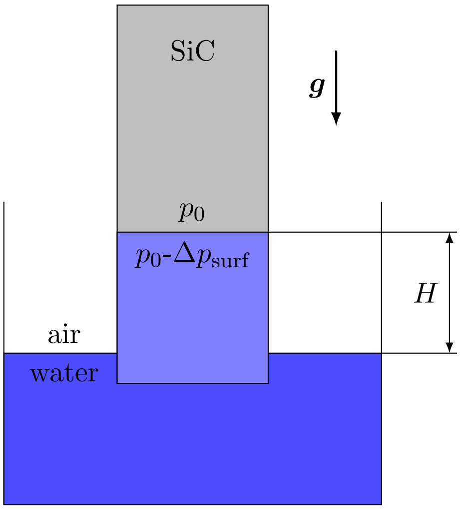

Figure A.1: Capillary rise of liquid column in a vertically positioned, porous piece of SiC.

Table A.1: The measured equilibrium height H, in m, and corresponding average pore diameter d_m, in µm, using three different contact angles θ.

	H [m]	d_m [µm]		
		$\theta = 0°$	$\theta = 30°$	$\theta = 60°$
TI-II	1.10	27.0	23.4	13.5
TI-VIII	1.06	28.0	24.3	14.0
TI-IX	1.09	27.3	23.6	13.6

this contact angle, but as a rule of thumb the contact angle can be assumed to be $\theta = 0°$ for very hydrophilic materials.

We made a small observation during the preliminary experiments concerning the capillary rise. Surprisingly, the first SiC-tubes we used showed no sign of water rise. We discovered that this was because the tubes had not been oxidized, and thus we found that an easy way to see, if our tubes and plugs had been oxidized, was to check if they could absorb water.

We used three thin-walled monotubes that had been extruded to a length of approximately 1.2 m using two pieces of SiC-clay in the extruder. One end of the monotubes was immersed in a bowl filled with demineralized water, see Fig. A.1, and a stand was used to keep them steady and in a vertical position. The three monotubes were put in the same bowl of water at the same time, and thus they experienced similar conditions. Humidity, temperature changes and water evaporation has not been taken into account. The experiments lasted for two days, hence it is assumed that the water has reached its equilibrium height.

The results from the experiment are shown in Table A.1. The three monotubes reached almost the same height of just over 1 m, which corresponds to an average pore diameter of approximately 27 µm, assuming a contact angle of 0°. The expected pore diameter is in the order of 10-12 µm, as stated in [20], and the calculated diameter is then nearly three times too high. If a contact angle of 0° is correct, the water should reach an equilibrium height of nearly 3 m, much higher than the observed 1 m. Since we conducted the experiments correctly, this means that either the expected pore size or the contact angle is wrong. The most obvious reason is the contact angle, since it is unknown. We therefore calculated the average pore diameter using two other contact angles of $\theta = 30°$ and $\theta = 60°$, as seen in Table A.1. This gives a pore diameter of about 24 µm and 14 µm, respectively, and to get an average pore diameter around the expected 10-12 µm from our experiments, the contact angle should then be more than 60°. We have not investigated the contact angle further, however, as these results are not crucial to our thesis work.

A.3 Bubble point

The maximum pore size d_max, as well as the homogeneity of our plugs and tubes, can be found using the so-called bubble point method. The bubble point method is described in [5, 6, 17, 18]. It is a very simple method, where the SiC-samples are immersed in water, and air pressure is then applied upstream, increasing it slowly until air bubbles are formed on the downstream surface, see Fig. A.2. This pressure is called the bubble point pressure p_{b}, and it is defined as the pressure needed to press a steady stream of air bubbles through the largest pores in a saturated, porous medium, [17]. This means that we had to estimate when the bubble point pressure occurred by the amount of air bubbles coming through the porous SiC-samples. The bubble point test can be used not only for estimating the maximum pore diameter, but may also indicate if our plugs and tubes are damaged. If bubbles form at a lower pressure than expected, and only in one region of the SiC-sample, it could indicate a hole or a crack in the sample.

It is assumed that the pores are straight, circular channels, as in the capillary rise experiment, and the maximum pore size can be found from Eq. (A.6), which is a modification of Eq. (A.5),

$$d_{\mathrm{max}} = \frac{4\gamma}{p_{\mathrm{b}}} \cos\theta. \tag{A.6}$$

As in Eq. (A.5) $\gamma = 72.9\,\mathrm{mJ/m^2}$ is the surface tension at the water/air interface and θ is the contact angle at the water-SiC-air contact line.

Seven thin-walled and six thick-walled monotubes were used in the experiments. The experimental setup is shown in Fig. A.2. Pressurised air was connected to one end of the monotubes and the other end was sealed. The tubes were then immersed in demineralized water for at least ten minutes, until they were fully saturated. Afterwards the air pressure was slowly increased until air bubbles formed on the outer surface of the monotubes, and the bubble point pressure was observed. The experiment was repeated several times for all the monotubes, in order to check that the correct bubble point pressure had been obtained.

The average bubble point pressure found for the 13 monotubes is listed in Table A.2, as well as the estimated maximum pore diameter at three different contact angles. The errors are the standard deviations of the pressures and pore diameters found from each of the monotubes. The average maximum pore diameter is 16.2 µm, when a contact angle of $\theta = 0°$ is assumed. As mentioned, the mean pore diameter is expected to be around 10-12 µm, and it is expected that the maximum pore diameter is only slightly larger. Thus,

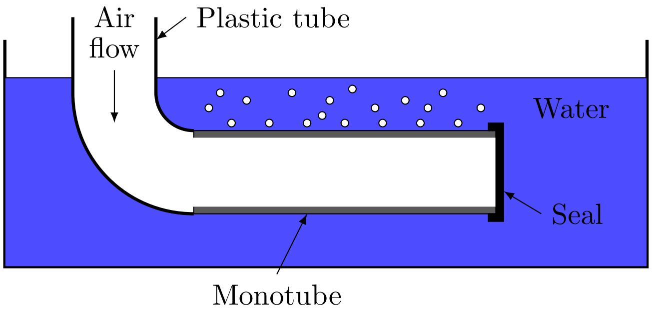

Figure A.2: Experimental setup for the bubble point experiments showing the cross-section of a monotube. For clarity the dimensions have been altered on the sketch. The monotube is immersed in a bowl of demineralized water and air flow is supplied in one end, while the other end is sealed.

Table A.2: The average bubble point pressure p_b, in bar, and the corresponding maximum pore diameters d_max, in µm, for three different contact angles. The errors are the standard deviations of the pressures and pore diameters found from each of the monotubes.

p_b [bar]	d_max [µm]		
	$\theta = 0°$	$\theta = 30°$	$\theta = 60°$
0.181 ± 0.006	16.2 ± 0.6	14.0 ± 0.5	8.1 ± 0.3

our results agree well with our expectations at a contact angle of $\theta = 0°$, opposed to the results found in the capillary rise method. The reason for this is unknown and has not been investigated further.

Since the results from the capillary rise method and the bubble point method do not agree, no conclusions are made from the methods presented here. The methods are still usable, however, as they give useful information concerning the quality of the SiC-samples.

Appendix B

Investigation of the experimental setup

The pressure drops in the experimental setup between the initial position of the pressure transmitters and the housing is investigated and calculated analytically. This check is carried out to see if the pressure drops in the setup will have an influence on the measured pressures. The pressure drops presented in this appendix will not be described in detail and only the results will be given.

The flow rate in the pipes on the setup is assumed to be between $Q = 1\,\mathrm{m}^3/\mathrm{h}$ and $Q = 4\,\mathrm{m}^3/\mathrm{h}$ during the experiments and the pipe diameters vary from $D = 18\,\mathrm{mm}$ to $D = 46\,\mathrm{mm}$. The Reynolds number, found from Eq. (2.2), then varies from $\mathrm{Re} = 7.5 \times 10^3$ to $\mathrm{Re} = 8 \times 10^4$ using water in the pipes with $\rho = 1000\,\mathrm{kg/m}^3$ and $\eta = 10^{-3}\,\mathrm{Pa\ s}$. As the Reynolds numbers are larger than $\mathrm{Re} = 4 \times 10^3$, the pipe flow is thus fully turbulent at all times.

The loss in mechanical energy in a pipe system with viscous flow is described by the energy equation, see Eq. (2.23). The kinetic energy coefficient α can be assumed to be $\alpha = 1$ for turbulent flow which therefore will be used in this investigation. The pipes in the setup are assumed to be smooth.

Major Losses

The major head losses are found from Eq. (2.25) and arise due to pipe roughness. The friction factor f is given by the Blasius correlation, Eq. (2.30), and is valid for turbulent flow in smooth pipes with $\mathrm{Re} \leq 10^5$, see section 8-7 in [3].

Minor Losses

The minor losses are caused by a variety of fittings, bends and abrupt changes in diameter in the pipes and can be found from

$$h_{\mathrm{l_m}} = K_{\mathrm{l}} \frac{\bar{V}^2}{2}, \tag{B.1a}$$

$$h_{\mathrm{l_m}} = f \frac{L_0}{D} \frac{\bar{V}^2}{2}, \tag{B.1b}$$

where K_l is the loss coefficient and L_0 is a characteristic length. The values are taken from the corresponding graphs and tables in section 8-7 in [3].

B.1 Pressure drop from PT01 to housing

The pressure drops from PT01 to the housing are found from Eq. (2.23) and the calculated pressure drops in the different sections of the system between PT01 and the housing are listed in Table B.1. For a feed flow rate of $Q_\mathrm{f} = 1\,\mathrm{m^3/h}$ the dynamic pressure difference from PT01 to the housing is around $\Delta p = p_2 - p_1 = -0.03\,\mathrm{bar}$, meaning a pressure drop of 0.03 bar. Because of the height difference this pressure drop is balanced by the hydrostatic pressure and the total pressure difference actually becomes positive. If the flow rate is increased to $Q_\mathrm{f} = 4\,\mathrm{m^3/h}$ the pressure drop is much larger being 0.35 bar without hydrostatic pressure and 0.26 bar when the hydrostatic pressure is included. The pressure at the feed side of the housing is assumed to be around 2 bar it the highest flow rates and a pressure drop of 0.26 bar is therefore significant and cannot be neglected in the experiments. It is further noticed that the metal tube and the sudden contractions deliver most of the pressure drop.

B.2 Pressure drop from housing to PT02

The pressure drop between the housing and PT02 is estimated for retentate flow rates of $Q_\mathrm{r} = 1\,\mathrm{m^3/h}$ and $Q_\mathrm{r} = 4\,\mathrm{m^3/h}$. The results are listed in Table B.2. The dynamic pressure drop is negligible for $Q_\mathrm{r} = 1\,\mathrm{m^3/h}$, but for a flow rate of $Q_\mathrm{r} = 4\,\mathrm{m^3/h}$ the pressure difference is 0.026 bar, thus it is a dynamic pressure increase and not decrease from the housing to PT02. Table B.2 further shows that nearly all of the pressure increase originates from

Table B.1: Pressure difference $\Delta p = p_2 - p_1$ from PT01 to the housing with a feed flow rate of $Q_\mathrm{f} = 1\,\mathrm{m^3/h}$ and $Q_\mathrm{f} = 4\,\mathrm{m^3/h}$.

Description	D_1 [mm]	D_2 [mm]	L [mm]	K_l	Δp [Pa]	
					$Q_\mathrm{f} = 1\,\mathrm{m^3/h}$	$Q_\mathrm{f} = 4\,\mathrm{m^3/h}$
Straight part	46	46	80	0	-1	-10
Gradual contraction	46	36	100	0.05	-30	-400
Sudden contraction	36	18	0	0.41	-800	-12800
Metal tube	18	18	2000	0	-1800	-20000
Sudden expansion	18	38	0	0.6	200	3300
Straight part	38	38	24	0	-1	-7
Gradual contraction	38	21	20	0.04	-300	-4900
Sum of pressure drop					-2700	-35000
Hydrostatic pressure					8800	8800
Total pressure drop					6100	-26000

Table B.2: Pressure difference $\Delta p = p_2 - p_1$ from the housing to PT02 with a retentate flow rate of $Q_\mathrm{r} = 1\,\mathrm{m}^3/\mathrm{h}$ and $Q_\mathrm{r} = 4\,\mathrm{m}^3/\mathrm{h}$.

Description	D_1 [mm]	D_2 [mm]	L [mm]	K_l	Δp [Pa]	
					$Q_\mathrm{r} = 1\,\mathrm{m}^3/\mathrm{h}$	$Q_\mathrm{r} = 4\,\mathrm{m}^3/\mathrm{h}$
Gradual expansion	21	38	20	0.4	160	2600
Straight part	38	38	24	0	-1	-7
Sudden contraction	38	36	0	0.01	-8	-100
Gradual expansion	36	46	10	0.2	14	200
Standard elbow 90°	46	46	0	15	-7	-80
Straight part	46	46	250	0	-3	-30
Sum of pressure drop					150	2600
Hydrostatic pressure					2000	2000
Total pressure drop					2100	4600

the first gradual expansion after the housing. For both flow rates the pressure drops are negligible when compensating for the hydrostatic pressure, as the pressure at the retentate side of the housing will be much higher than the estimated pressure drops. It is therefore not necessary to change the position of PT02 if we compensate for the hydrostatic pressure.

B.3 Pressure drop from housing to PT03

The pressure drop from the housing to PT03 is also estimated and the results are listed in Table B.3. The flow rate on the permeate side is lower compared to the flow rate on the feed and retentate side of the housing, thus the pressure drop is estimated for permeate flow rates of $Q_\mathrm{p} = 0.5\,\mathrm{m}^3/\mathrm{h}$ and $Q_\mathrm{p} = 2\,\mathrm{m}^3/\mathrm{h}$. The table shows that the dynamic pressure drop for the low flow rate is negligible but because of the relatively high hydrostatic pressure the total pressure drop is significant since the gauge pressure at the permeate

Table B.3: Pressure difference $\Delta p = p_2 - p_1$ from the housing to PT03 with a permeate flow rate of $Q_\mathrm{p} = 0.5\,\mathrm{m}^3/\mathrm{h}$ and $Q_\mathrm{p} = 2\,\mathrm{m}^3/\mathrm{h}$.

Description	D_1 [mm]	D_2 [mm]	L [mm]	K_l	Δp [Pa]	
					$Q_\mathrm{p} = 0.5\,\mathrm{m}^3/\mathrm{h}$	$Q_\mathrm{p} = 2\,\mathrm{m}^3/\mathrm{h}$
Sudden expansion	18	20	0	0.05	40	700
Plastic tube	20	20	3150	0	-500	-5700
Sudden expansion	20	36	0	0.4	50	800
Gradual expansion	36	46	10	0.2	3	60
Straight part	46	46	0	0	-1	-3
Sum of pressure drop					-400	-4100
Hydrostatic pressure					-6800	-6800
Total pressure drop					-7200	-11000

Table B.4: Hydrodynamic pressure drop $\Delta p = p_2 - p_1$ from PT01 to the housing with different tubes instead of the metal tube. The pressure drops are estimated at feed flow rates of $Q_\mathrm{f} = 1\,\mathrm{m^3/h}$ and $Q_\mathrm{f} = 4\,\mathrm{m^3/h}$.

	Δp [Pa]		
	$D = 18\,\mathrm{mm}$	$D = 33\,\mathrm{mm}$	$D = 51\,\mathrm{mm}$
$Q_\mathrm{f} = 1\,\mathrm{m^3/h}$	-2700	-450	-350
$Q_\mathrm{f} = 4\,\mathrm{m^3/h}$	-35000	-6800	-5500

side of the housing is assumed to be close to zero. At a flow rate of $Q_\mathrm{p} = 2\,\mathrm{m^3/h}$ the pressure drop is even higher. Nearly all the resistance is generated in the plastic tube, but another significant contribution comes from the hydrostatic pressure.

B.4 Larger tubes from PT01 and PT03 to the housing

The error from the hydrostatic pressure can be corrected in the measured data since it is constant at all flow rates, but the hydrodynamic pressure drop is more difficult to correct. The pressure drops between the housing and PT01 and PT03 will decrease significantly if the small tubes are replaced with tubes having a larger diameter. If this is done some of the sudden expansions and contractions will also become smaller.

In Table B.4 the hydrodynamic pressure drop is listed for the original metal tube and two tubes with larger diameters. The pressure drops listed are from PT01 to the housing. Since different fittings are needed when changing the diameter of the tube the changed pressure drops in these fittings are also included. The table clearly shows that by increasing the diameter of the metal tube the hydrodynamic pressure drop will decrease significantly.

The same investigation is made with the tube from the housing to PT03. In Table B.5 the pressure drops for tubes with larger diameters are estimated and listed together with the pressure drop in the original plastic tube. The table shows that Δp becomes smaller and even positive. It becomes positive because of the pressure increase created by the sudden expansion just after the housing.

From the calculations in this appendix it is shown that the hydrodynamic pressure drop can be reduced significantly by exchanging the metal and plastic tubes with tubes with larger diameters. However, it is still preferable to simply change the position of PT01 and PT03 closer to the housing in order to measure the correct pressures.

Table B.5: Hydrodynamic pressure drop $\Delta p = p_2 - p_1$ from the housing to PT03 with different tubes instead of the plastic tube. The pressure drops are estimated at permeate flow rates of $Q_\mathrm{p} = 0.5\,\mathrm{m^3/h}$ and $Q_\mathrm{p} = 2\,\mathrm{m^3/h}$.

	Δp [Pa]		
	$D = 20\,\mathrm{mm}$	$D = 33\,\mathrm{mm}$	$D = 51\,\mathrm{mm}$
$Q_\mathrm{p} = 0.5\,\mathrm{m^3/h}$	-400	30	60
$Q_\mathrm{p} = 2\,\mathrm{m^3/h}$	-4100	630	1000

Appendix C

Additional experiments

Some additional experiments have been carried out and these will shortly be presented in the following. A few cross-flow experiments have been conducted with both thin-walled monotubes and 24-channel tubes to see how an increasing retentate flow rate influences the relation between permeate flow rate and transmembrane pressure. Furthermore experiments have been conducted with two 1 m long thin-walled monotubes and with thin-walled monotubes and 24-channel tubes coated with the 1 µm membrane to see how this membrane influences the permeate flow rate.

C.1 Cross-flow experiments

Cross-flow measurements are carried out with different retentate flow rates in order to observe the possible changes in the relation between the permeate flow rate Q_p and the transmembrane pressure p_tm compared to dead-end experiments. The results from the cross-flow experiments carried out with monotube TI-XVIII-I and 24-channel tube XXIV-XIV coated with a 0.04 µm membrane are included here and these results are representative for the tendencies seen in the cross-flow experiments.

C.1.1 Monotubes

Fig. C.1 shows the results from both dead-end and cross-flow experiments with monotube TI-XVIII-I. The cross-flow experiments are carried out at three different relative retentate flow rates compared to the feed flow rates. $Q_\mathrm{r}/Q_\mathrm{f}$ changes slightly as the pressure is increased and the values used here are calculated at the highest flow rates used. At low retentate flow $Q_\mathrm{r}/Q_\mathrm{f} = 35\%$, medium retentate flow $Q_\mathrm{r}/Q_\mathrm{f} = 46\%$ and high retentate flow $Q_\mathrm{r}/Q_\mathrm{f} = 60\%$. From Fig. C.1(a) it is seen that the relation between permeate flow rate and transmembrane pressure is unchanged even at the highest retentate flow rate used. This is also seen from Fig. C.1(b) where the constants for the best-fitted lines are listed for the four different experiments. The slope a_2 of the best-fitted lines are equal for all four experiments. The reason that the Q_p-p_tm relation is unchanged is that the hydraulic resistance is negligible in the monotubes and the pressure distribution in the channel of the monotubes is therefore well estimated by the used equation for p_tm, see Eq. (2.22).

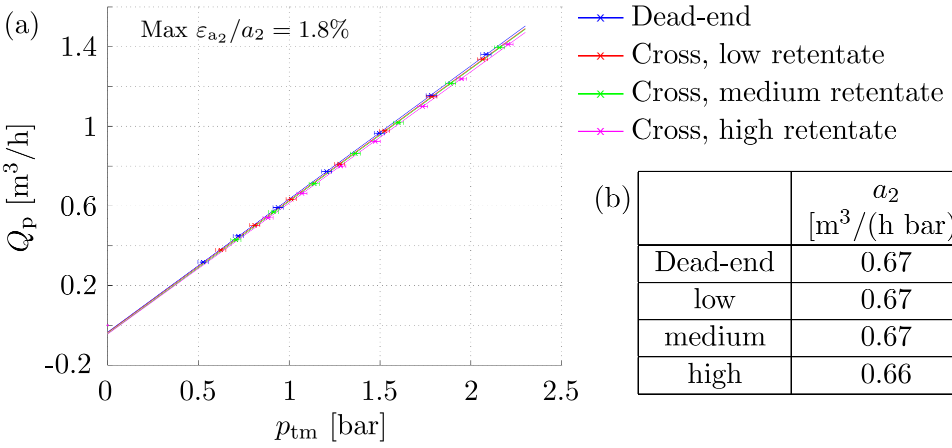

(b)

	a_2 [m^3/(h bar)]	Q_{p_2} [m^3/h]
Dead-end	0.67	-3.4×10^{-2}
low	0.67	-3.5×10^{-2}
medium	0.67	-3.6×10^{-2}
high	0.66	-3.8×10^{-2}

Figure C.1: (a) Cross-flow measurements with monotube TI-XVIII-I coated with a 0.04 µm membrane. At low retentate flow $Q_\mathrm{r}/Q_\mathrm{f} = 35\%$ at the highest flow rate used, at medium retentate flow it was $Q_\mathrm{r}/Q_\mathrm{f} = 46\%$ and high retentate flow $Q_\mathrm{r}/Q_\mathrm{f} = 60\%$. Increasing Q_r relative to Q_f did not change the Q_p-p_tm relation. Max ε_{a_2}/a_2 is the maximum relative error of the slopes for the best-fitted lines. (b) Table containing the constants for the best-fitted lines on the form $Q_\mathrm{p} = a_2 p_\mathrm{tm} + Q_{\mathrm{p}_2}$.

C.1.2 24-channel tubes

Results from cross-flow and dead-end measurements conducted with 24-channel tube XXIV-XIV coated with a 0.04 µm membrane are shown in Fig. C.2. As for the cross-flow experiments with monotubes the experiments are carried out at three different levels of relative retentate flow rate. At low retentate flow $Q_\mathrm{r}/Q_\mathrm{f} = 30\%$, medium retentate is $Q_\mathrm{r}/Q_\mathrm{f} = 48\%$, and high retentate is at $Q_\mathrm{r}/Q_\mathrm{f} = 66\%$. From Fig. C.2(a) it is seen that the

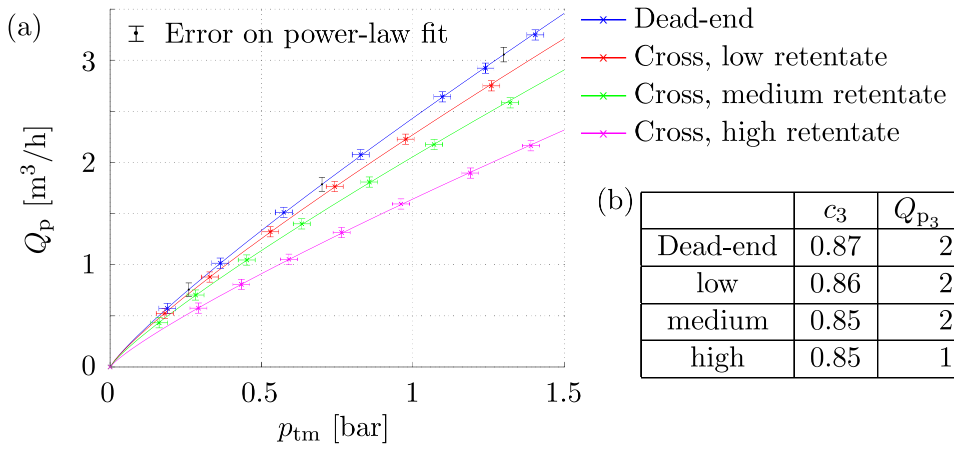

(b)

	c_3	Q_{p_3} [m^3/h]
Dead-end	0.87	2.43
low	0.86	2.27
medium	0.85	2.06
high	0.85	1.64

Figure C.2: (a) Cross-flow measurements with 24-channel tube XXIV-XIV coated with a 0.04 µm membrane. At low retentate flow $Q_\mathrm{r}/Q_\mathrm{f} = 30\%$ at the highest flow rate used, at medium retentate flow it was $Q_\mathrm{r}/Q_\mathrm{f} = 48\%$ and high retentate flow $Q_\mathrm{r}/Q_\mathrm{f} = 66\%$. Increasing Q_r relative to Q_f changed the Q_p-p_tm relation significantly. (b) Table containing the constants for the power-law lines on the form $Q_\mathrm{p} = Q_{\mathrm{p}_3} p_\mathrm{tm}^{c_3}$.

Q_p-p_tm relation decreases significantly as $Q_\mathrm{r}/Q_\mathrm{f}$ is increased. The constants for the power-law fitted lines are listed in Fig. C.2(b). These show that the power c_3 does not change as the retentate flow is increased but Q_{p_3} decreases significantly. The permeate flow rate decreases due to an increasing hydraulic resistance in the channels of the 24-channel tube, leading to a large pressure drop throughout the channels. As the flow is turbulent in the channels the assumptions used for calculating p_tm, see Section 2.2.4, are poor and p_tm is thus not correct. This is the reason for the decreasing Q_p-p_tm relation.

C.2 Long thin-walled monotube

When the experiments with the 1 m long thin-walled monotubes were conducted, a long housing had to be used. It was not possible to mount PT03 at this housing, which introduced some problems when measuring the permeate pressure. The housing had two permeate exits, one in each end, and therefore the permeate pressure could be measured at either of them while the permeate water could be let out through one or both of them. In order to check how this influenced the measured permeate pressure both PT02 and PT03, mounted at the extra pipe part and the small housing, respectively, was used to measure the pressure at the two exits, while the permeate water was let out through either or both of them. Four measurements conducted with TI-XXI, where the permeate pressure was measured in different ways, are shown in Fig. C.3. As the figure shows, the repeatability is poor which is due to the permeate pressure not being measured properly. If the water was let out through the same exit where the pressure was measured, a significant hydrodynamic pressure difference was introduced. If only one exit was used for the permeate water

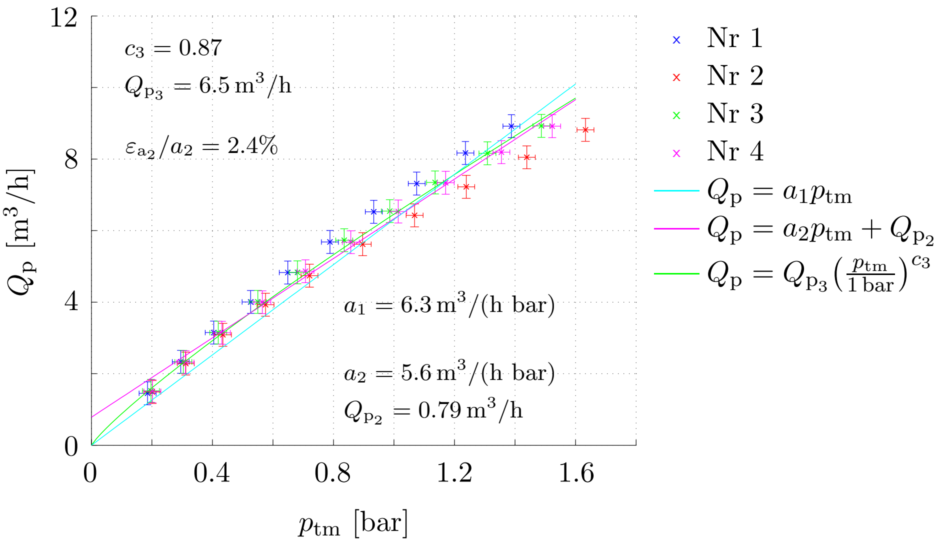

Figure C.3: A plot of the measurements for the 1 m long, thin-walled monotube TI-XXI. Q_p and p_tm are not linearly related due to a large hydraulic channel resistance in the long monotube. The error on the measurements is significantly larger than in the experiments with the short monotubes because it was not possible to measure the permeate pressure p_p properly.

and the other was used to measure p_p, the housing itself became restricting making the monotube less efficient. These problems were all dependent of the flow rate and therefore they became more and more significant as the flow rate increased, as seen in Fig. C.3. In the end it was concluded that it was not possible to measure the true permeate pressure at high flow rates.

Fig. C.3 also shows another interesting aspect, namely that the permeate flow rate and the transmembrane pressure are not linearly related for the long thin-walled monotubes. The best linear fit intersects with the Q_p-axis in $Q_{\mathrm{p}_2} = 0.79\,\mathrm{m}^3/\mathrm{h}$ and the slopes of the best fit and the linear line through $(0, 0)$ are not equal. Also the power in the power-law fit is $c_3 = 0.87$ which clearly indicates that the relation is nonlinear.

This nonlinearity is not only because of the problems with measuring p_p, but also because at the high flow rates, the hydraulic channel resistance in the monotube becomes significant. A pressure drop of nearly 0.2 bar was measured down the length of the monotube at a flow rate of $9\,\mathrm{m}^3/\mathrm{h}$. Hence, by increasing the length of the tube, the hydraulic channel resistance has increased considerably compared to the short monotubes which results in a nonlinear Q_p-p_tm profile.

C.3 Experiments with 1 μm membrane

Results from the experiments carried out with four short monotubes and four 24-channel tubes coated with a 1 μm membrane are presented here. These experiments were conducted in order to investigate how the 1 μm membrane effected the permeate flow rate.

C.3.1 Monotubes

The results from four short monotubes coated with a 1 μm membrane are shown in Fig. C.4. A linear relation between the flow rate and the transmembrane pressure is seen for all the tubes. By comparing these results with the results from the uncoated, short monotubes a 15% decrease is seen in permeate flow rate. A decrease of 15% is not much and we can conclude that adding the 1 μm membrane to the tubes does not change the flow rate significantly. The spread between the slopes of the best-fitted lines is 10% indicating that the monotubes are uniformly coated with the 1 μm membrane layer.

C.3.2 24-channel tubes

Experiments were conducted with four 24-channel tubes coated with the 1 μm membrane, and the results from these measurements are seen in Fig. C.5. From this figure it is seen that the relation between the permeate flow rate and the transmembrane pressure is still nonlinear as seen in the substrate experiments. A decrease of approximately 20% in average is observed in the permeate flow rate when compared to the results from the substrate experiments. The spread on the flow rates is approximately 25% which is more then seen for the monotubes having a spread of only 10%. This could indicate that the 24-channel tubes have not been uniformly coated with the 1 μm membrane.

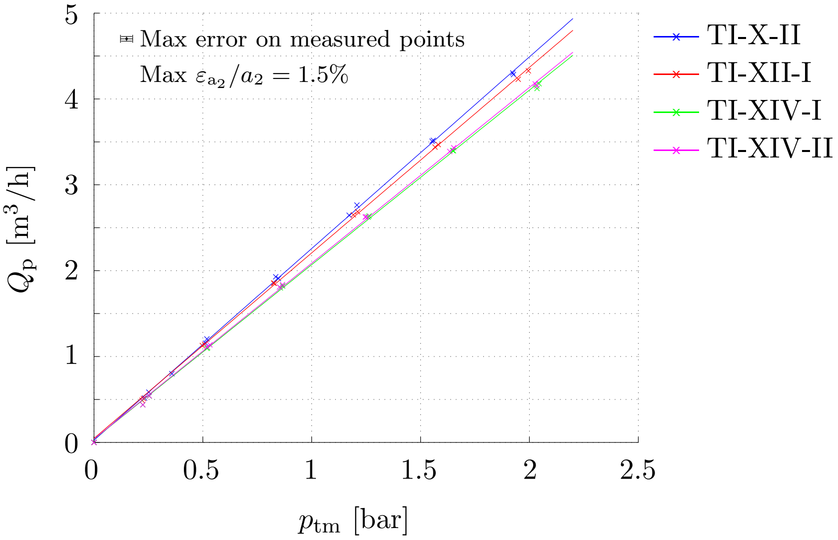

Figure C.4: Plot of the measurements for four thin-walled monotubes coated with the 1 µm membrane. The flow rate has decreased approximately by 15% compared to the substrate measurements. The spread on the slope of the best-fitted lines is 10%. Max ε_{a_2}/a_2 is the maximum relative error of the slopes for the best-fitted lines.

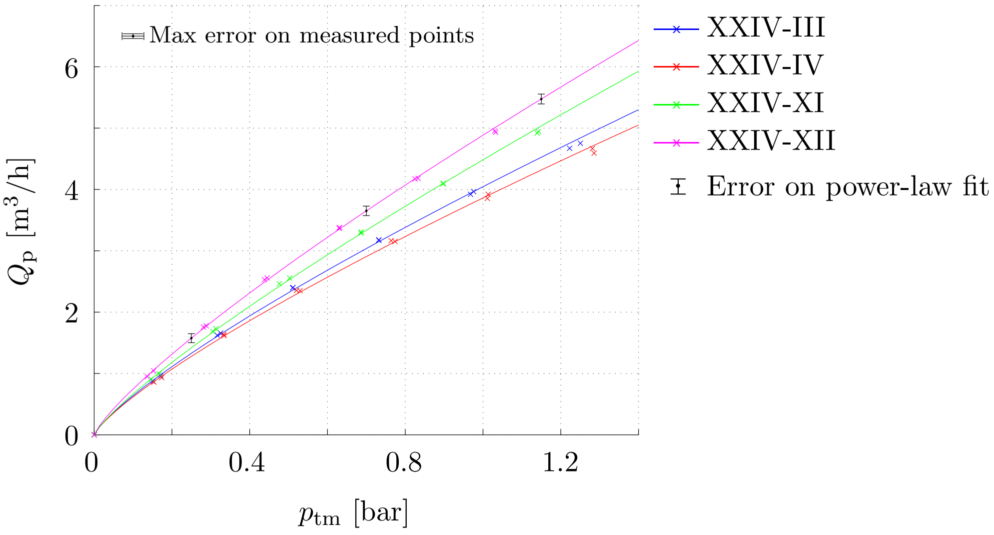

Figure C.5: Plot of the measurements for four 24-channel tubes coated with the 1 µm membrane. The flow rate has decreased approximately by 20% in average compared to the substrate measurements. The error on the power-law lines is given in three places on the slope of XXIV-XII. The spread on the flow rate is approximately 25%.

Appendix D

Module of hexagonal tubes

The restriction between hydraulic channel diameter and wall thickness of $w/d_\mathrm{h} = 0.25$ can be lowered by changing the tube geometry from circular to hexagonal, [22]. Such a geometry can sustain itself easier than a circular when extruded and therefore channels can be larger.

A design of a hexagonal tube is shown in Fig. D.1 with the pressure distribution found in the 2D COMSOL model for both a substrate tube and a tube with a 0.04 µm membrane added. The length of each side is $L_\mathrm{s} = 10\,\mathrm{mm}$, the wall thickness is $w = 1\,\mathrm{mm}$, and the length of the tube is $L = 305\,\mathrm{mm}$. The hydraulic diameter is $d_\mathrm{h} = 4.5 \times 10^{-3}\,\mathrm{m}$ in the inner channel and $d_\mathrm{h} = 5.2 \times 10^{-3}\,\mathrm{m}$ in the peripheral channels, hence the channels are

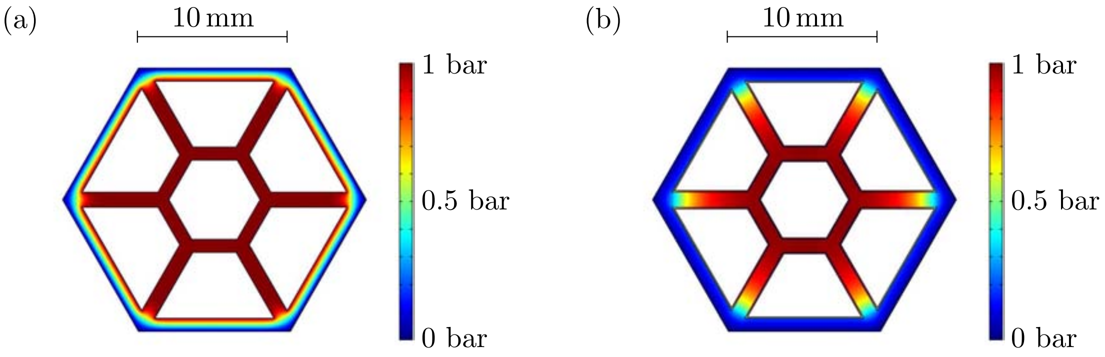

(c)

	Q_p [m^3/h]
Substrate	5.62
0.04 µm membrane	1.09

(d)

	$\mathcal{A}$ [m^2]
Surface area	1.83×10^{-2}
Membrane area	4.33×10^{-2}

Figure D.1: Pressure distribution in a hexagonal tube modeled in COMSOL. The side length is $L_\mathrm{s} = 10\,\mathrm{mm}$ and the wall thickness is $w = 1\,\mathrm{mm}$. The hydraulic diameter is $d_\mathrm{h} = 4.5 \times 10^{-3}\,\mathrm{m}$ in the inner channel and $d_\mathrm{h} = 5.2 \times 10^{-3}\,\mathrm{m}$ in the peripheral channels. (a) Pressure distribution in pure substrate. (b) Pressure distribution in tube coated with a 0.04 µm membrane. (c) Permeate flow rate results for a tube with a length of $L = 305\,\mathrm{mm}$. (d) Surface and membrane areas.

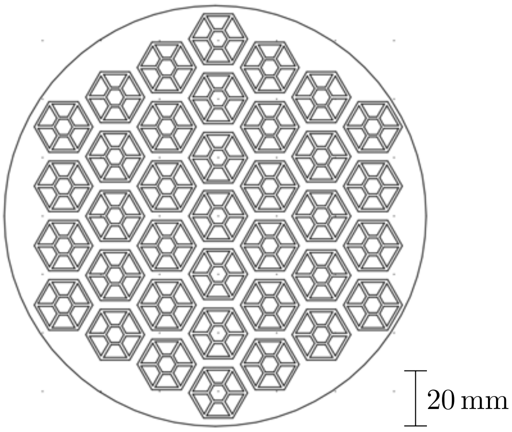

Figure D.2: Sketch of module containing 37 hexagonal tubes. The gab between two tubes is 3 mm. The outer diameter of the module is $d_\mathrm{o} = 144\,\mathrm{mm}$ which equal to the diameter of the COM-144-865-(2*2)-0.04.

relatively large. The hexagonal tube has a permeate flow rate of $Q_\mathrm{p} = 5.62\,\mathrm{m}^3/\mathrm{h}$ when the tube is uncoated and $Q_\mathrm{p} = 1.09\,\mathrm{m}^3/\mathrm{h}$ when the tube is coated with a 0.04 µm membrane. This less than found in the 2D Comsol model of the original 24-channel tube, which is because the hexagonal tube has a much smaller cross-section. If the hydraulic resistance is included the hexagonal tube will be better than the original 24-channel tube but still less efficient compared to the other optimization suggestions. The hexagonal design proposal presented here has not been optimized, however, as the surface area has not been increased which was proven to be a crucial factor in Section 8.1. The hexagonal design is included to show that other geometries than circular can be used for the tubes in order to increase the channel size relative to the wall thickness.

A module containing parallel connected hexagonal tubes with a length of $L = 305\,\mathrm{mm}$ is made and a sketch of this module is shown in Fig. D.2. It contains 37 hexagonal tubes and the gab between two tubes is 3 mm while the outer diameter of the module is $d_\mathrm{o} = 144\,\mathrm{mm}$ which is equal to the diameter of the COM-144-865-(2*2)-0.04. The module delivers a permeate flow rate of $Q_\mathrm{p} = 40.33\,\mathrm{m}^3/\mathrm{h}$ when the tubes are coated with the 0.04 µm membrane, which is a 170% increase compared to the permeate flow rate delivered by a standard COM-144-865-(2*2)-0.04. The increase is comparable with the increase seen from a module containing parallel connected 24-channel tubes.

The hexagonal tube presented in this appendix shows that good results are obtainable with other geometries than cylinders and the hexagonal geometry can be optimized further by increasing the surface area.

Appendix E

Data sheet

An official data sheet containing information about some of CoMeTas' large standard membranes is presented here. The information for the COM-144-865-(2*2)-0.04 having a length of $L = 865\,\mathrm{mm}$, an outer diameter of $d_\mathrm{o} = 144\,\mathrm{mm}$, a wall thickness of $w = 0.8\,\mathrm{mm}$, containing approximately 1900 channels with a size of $2\,\mathrm{mm} \times 2\,\mathrm{mm}$ and coated with the $0.04\,\mu\mathrm{m}$ membrane is used for comparison to the optimization suggestions presented in Chapter 8.

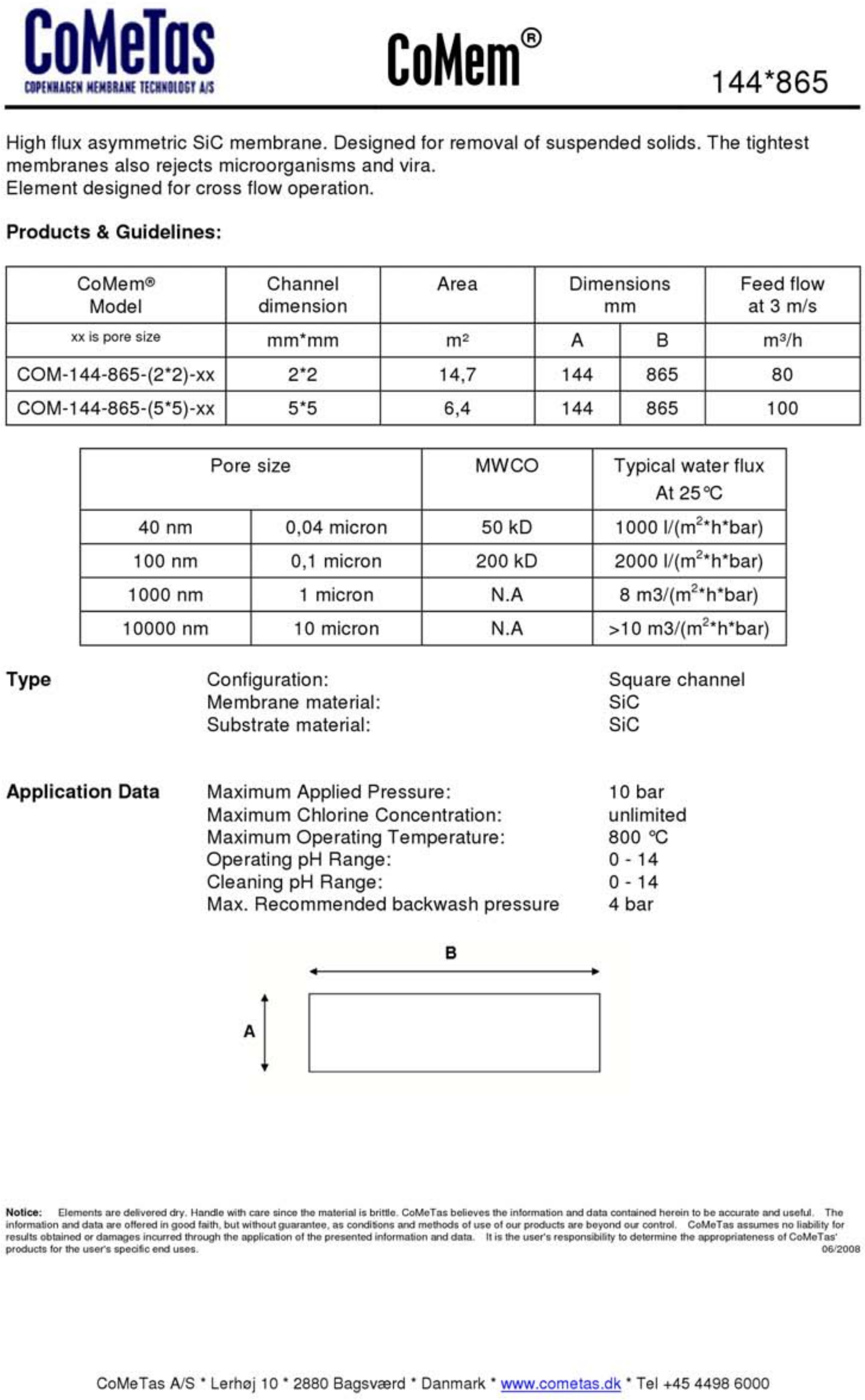

CoMeTas
COPENHAGEN MEMBRANE TECHNOLOGY A/S

CoMem®

144*865

High flux asymmetric SiC membrane. Designed for removal of suspended solids. The tightest membranes also rejects microorganisms and vira.
Element designed for cross flow operation.

Products & Guidelines:

CoMem® Model	Channel dimension	Area	Dimensions mm		Feed flow at 3 m/s
xx is pore size	mm*mm	m^2	A	B	m^3/h
COM-144-865-(2*2)-xx	2*2	14,7	144	865	80
COM-144-865-(5*5)-xx	5*5	6,4	144	865	100

Pore size		MWCO	Typical water flux At 25°C
40 nm	0,04 micron	50 kD	1000 l/(m^2*h*bar)
100 nm	0,1 micron	200 kD	2000 l/(m^2*h*bar)
1000 nm	1 micron	N.A	8 m3/(m^2*h*bar)
10000 nm	10 micron	N.A	>10 m3/(m^2*h*bar)

Type	Configuration:	Square channel
	Membrane material:	SiC
	Substrate material:	SiC
Application Data	Maximum Applied Pressure:	10 bar
	Maximum Chlorine Concentration:	unlimited
	Maximum Operating Temperature:	800 °C
	Operating pH Range:	0 - 14
	Cleaning pH Range:	0 - 14
	Max. Recommended backwash pressure	4 bar

Notice: Elements are delivered dry. Handle with care since the material is brittle. CoMeTas believes the information and data contained herein to be accurate and useful. The information and data are offered in good faith, but without guarantee, as conditions and methods of use of our products are beyond our control. CoMeTas assumes no liability for results obtained or damages incurred through the application of the presented information and data. It is the user's responsibility to determine the appropriateness of CoMeTas' products for the user's specific end uses.
06/2008

CoMeTas A/S * Lerhøj 10 * 2880 Bagsværd * Danmark * www.cometas.dk * Tel +45 4498 6000

Appendix F

Working drawings

The working drawings included here have been created to improve the extruder head used to produce the monotubes. The part with the new adjustment screws for the extruder head is shown in Appendix F.1, while the new inner cylinders for fabricating the thick-walled and thin-walled monotubes are shown in Appendixes F.2 and F.3, respectively.

F.1 Part for extruder head

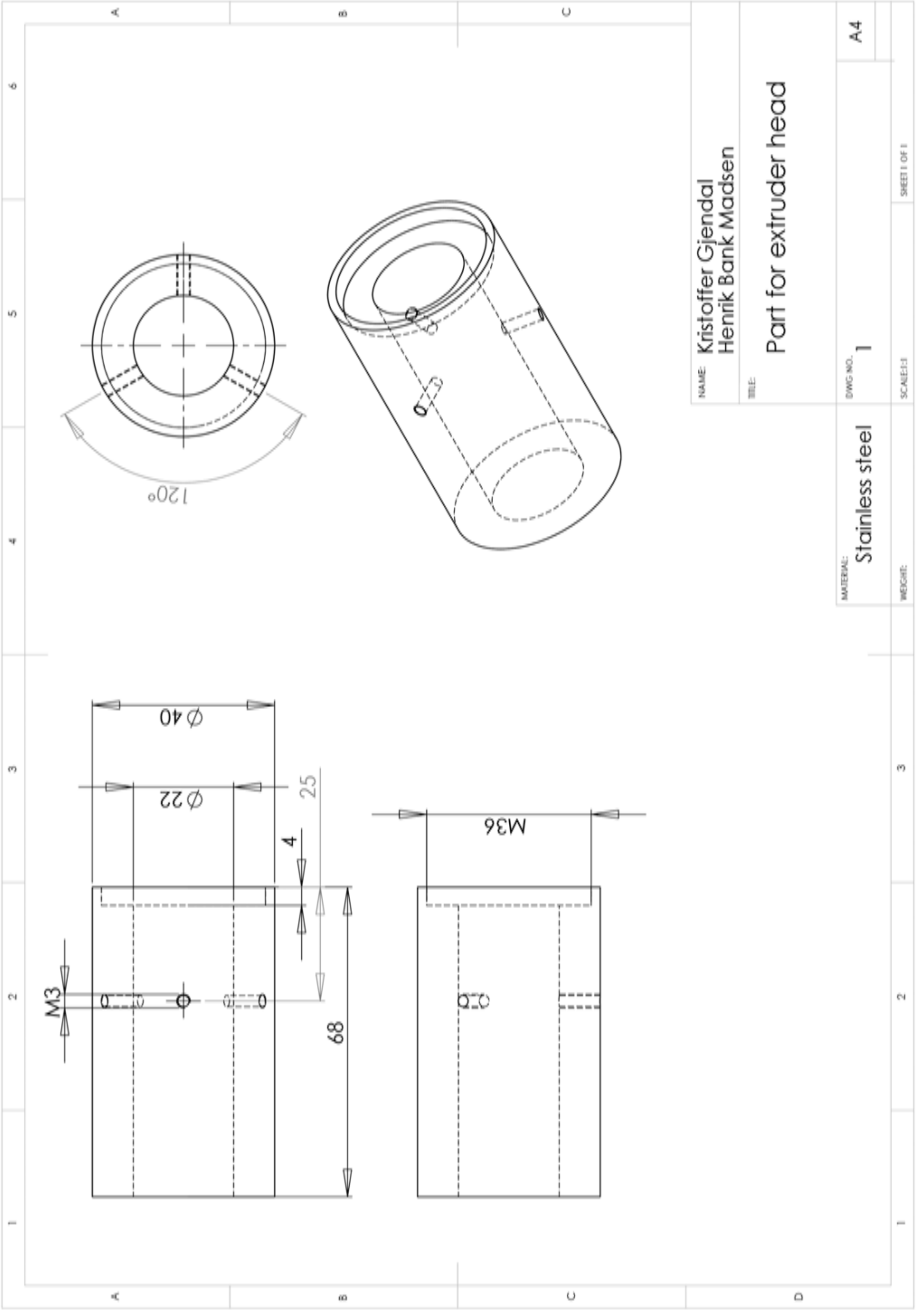

Figure F.1: New part for the extruder head with holes for adjustment screws.

F.2 Thin inner cylinder

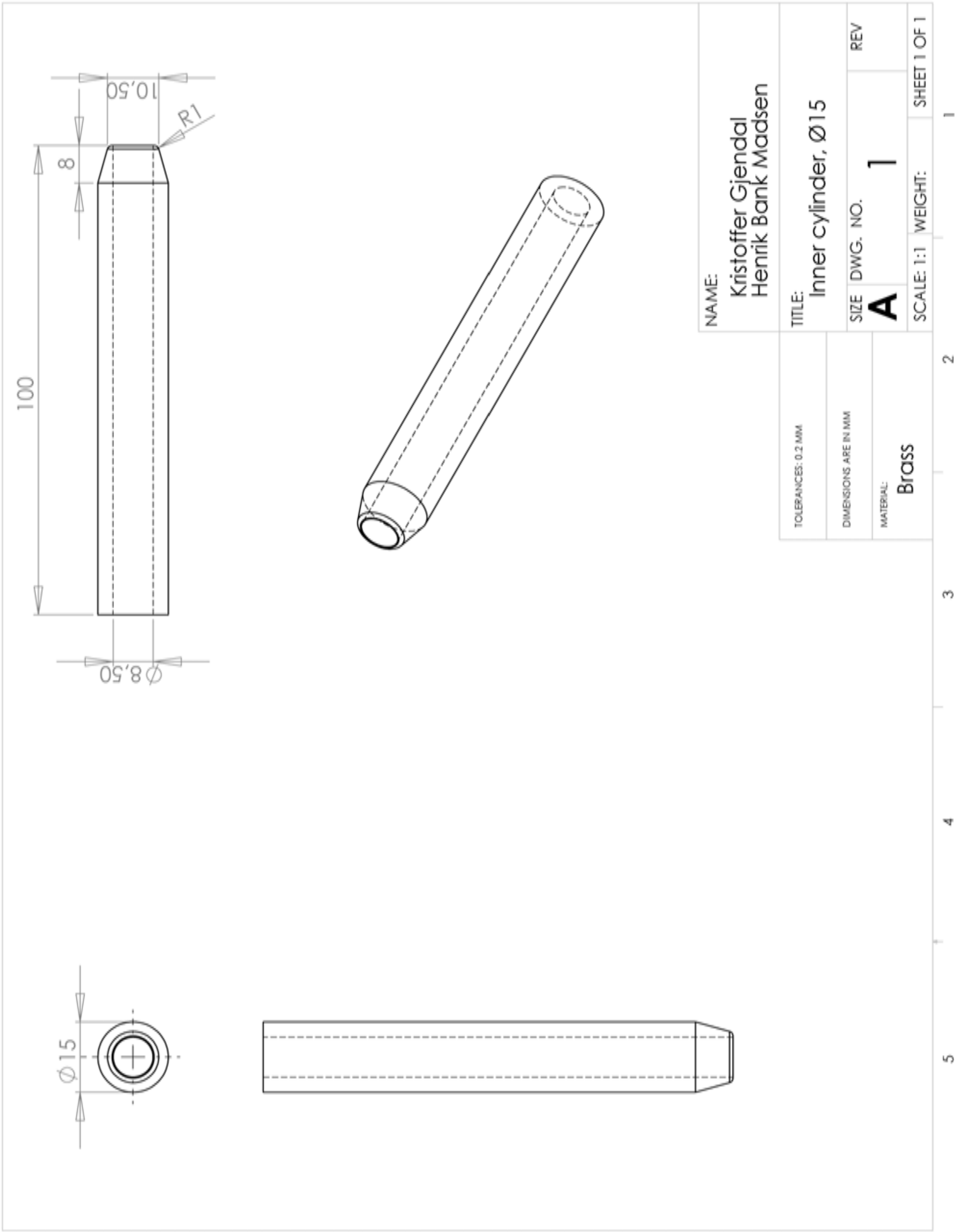

Figure F.2: Thin inner cylinder made out of brass used to make the thick-walled monotubes.

F.3 Thick inner cylinder

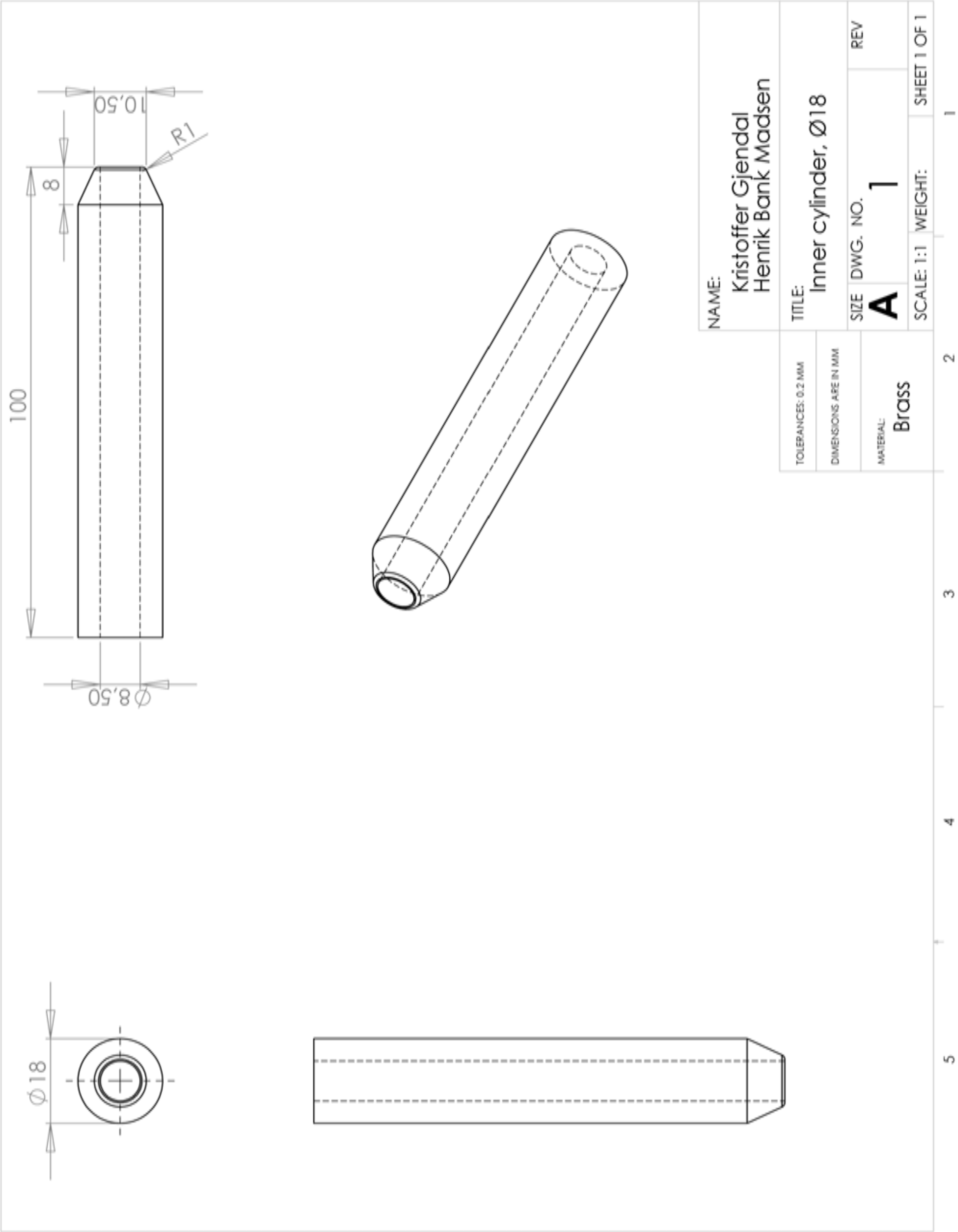

Figure F.3: Thick inner cylinder made out of brass used to make the thin-walled monotubes.

Bibliography

[1] *Theoretical Microfluidics*
Henrik Bruus,
Oxford University Press Inc, Oxford, GB, (2008).

[2] *Dynamics of fluids in porous media*
Jacob Bear,
American Elsevier Publishing Company, New York, (1972).

[3] *Introduction to fluid mechanics*
Robert W. Fox, Alan T. McDonald and Philip J. Pritchard,
John Wiley & sons Inc, International Edition, (2004).

[4] *Viscous fluid flow*
Frank M. White,
McGraw-Hill, Singapore, International Edition, (2006).

[5] *Membrane Filtration - and related molecular separation technologies*
Edited by: Werner Kofod Nielsen,
APV Systems, (2000).

[6] *Membrane Filtration - The Technology of Pressure-driven Crossflow Processes*
R. G. Gutman,
Adam Hilger, Bristol, (1987).

[7] *Flow Through Porous Media*
Roger J. M. De Wiest,
Academic press Inc, London, (1969).

[8] *Flow in Porous Media with Special Reference to Breakwater Structures*
Ole Holst Andersen,
Centertrykkeriet, Aalborg University, (1994).

[9] *Introduction to Modeling of Transport Phenomena in Porous Media*
Jacob Bear and Yehuda Bachmat,
Kluwer Academic Publichers, Dordrecht, (1990)

[10] Thomas Eilkær Hansen,
Flow in micro porous silicon carbide
M.Sc. thesis, Department of Micro- and Nanotechnology, Technical University of Denmark, (2007),
http://www.nanotech.dtu.dk/Research/Theory/TMF/publications/MSc_theses.aspx

[11] Brooks, C. S., Decrascente, M. A. and Scola, D. A.,
The Wetting of Silicon Carbide Surfaces
United Aircraft Research Laboratories. East Hartford, (1968).

[12] Fand, R. M., Kim, B. Y. K., Lam, A. C. C., and Phan, R. T.,
Resistance to the Flow of Fluids Through Simple and Complex Porous Media Whose Matrices Are Composed of Randomly Packed Spheres
ASME J. Fluids Eng., vol. 109, pp. 268-274, (1987).

[13] Ifiyenia Kececioglu and Yuxiang Jiang,
Flow Through Porous Media of Packed Spheres Saturated With Water
ASME J. Fluids Eng., vol. 116, pp. 164-170, (1994).

[14] Kagramanov, G. G., Dytnerskii, Yu. I. and Il'ib, P. G.,
A model simulation of the filteringprocess in multichannel ceramic membranes
Vol. 42, Nos. 3-4, (2001)

[15] Alexopoulos, S., Breitbach, G., Hoffschmidt, B., Stobbe, P.,
Computational fluid flow of porous ReSIC ceramic filtering modules and optimization of the channel edge form geometry
10th World Filtration Congress

[16] Schwartzendruber, Dale,
Non-Darcy Flow Behaviour in Liquid-Saturated Porous Media Journal of Geophysical Research, vol. 67, no. 13, (1962)

[17] ASTM F316-03,
Standard Test Methods for Pore Size Characteristics of Membrane Filters by Bubble Point and Mean Flow Pore Test Annual book of ASTM standards. Section 11, volume 11.02, Water and Environmental Technology, (2007).

[18] ASTM E128-99,
Standard Test Method for Maximum Pore Diameter and Permeability of Rigid Porous Filters for Laboratory Use Annual book of ASTM standards. Section 14, General Methods and Instrumentation, (2005).

[19] Webpage of CoMeTas A/S:
http://www.cometas.dk

[20] Webpage of LiqTech A/S:
http://www.liqtech.dk

[21] Webpage of DTI Oil and gas:
http://ior.senergyltd.com/issue8/tp/

[22] Private communication
Johnny Marker
Technical Director
Research & Development
LiqTech A/S
e-mail: jm@liqtech.dk